

INFORMATION TO USERS

While the most advanced technology has been used to photograph and reproduce this manuscript, the quality of the reproduction is heavily dependent upon the quality of the material submitted. For example:

- Manuscript pages may have indistinct print. In such cases, the best available copy has been filmed.
- Manuscripts may not always be complete. In such cases, a note will indicate that it is not possible to obtain missing pages.
- Copyrighted material may have been removed from the manuscript. In such cases, a note will indicate the deletion.

Oversize materials (e.g., maps, drawings, and charts) are photographed by sectioning the original, beginning at the upper left-hand corner and continuing from left to right in equal sections with small overlaps. Each oversize page is also filmed as one exposure and is available, for an additional charge, as a standard 35mm slide or as a 17"x 23" black and white photographic print.

Most photographs reproduce acceptably on positive microfilm or microfiche but lack the clarity on xerographic copies made from the microfilm. For an additional charge, 35mm slides of 6"x 9" black and white photographic prints are available for any photographs or illustrations that cannot be reproduced satisfactorily by xerography.

8716735

Albers, Mark L.

A STUDY OF DEPOSITION CONDITIONS AND HYDROGEN MOTION IN R. F.
SPUTTERED HYDROGENATED AMORPHOUS SILICON

Iowa State University

PH.D. 1987

University
Microfilms
International 300 N. Zeeb Road, Ann Arbor, MI 48106

PLEASE NOTE:

In all cases this material has been filmed in the best possible way from the available copy. Problems encountered with this document have been identified here with a check mark .

1. Glossy photographs or pages _____
2. Colored illustrations, paper or print _____
3. Photographs with dark background _____
4. Illustrations are poor copy _____
5. Pages with black marks, not original copy
6. Print shows through as there is text on both sides of page _____
7. Indistinct, broken or small print on several pages
8. Print exceeds margin requirements _____
9. Tightly bound copy with print lost in spine _____
10. Computer printout pages with indistinct print _____
11. Page(s) _____ lacking when material received, and not available from school or author.
12. Page(s) _____ seem to be missing in numbering only as text follows.
13. Two pages numbered _____. Text follows.
14. Curling and wrinkled pages _____
15. Dissertation contains pages with print at a slant, filmed as received _____
16. Other _____

University
Microfilms
International

A study of deposition conditions and hydrogen motion
in r.f. sputtered hydrogenated amorphous silicon

by

Mark L. Albers

A Dissertation Submitted to the
Graduate Faculty in Partial Fulfillment of the
Requirements for the Degree of
DOCTOR OF PHILOSOPHY

Department: Physics
Major: Solid State Physics

Approved:

Signature was redacted for privacy.

~~In Charge of Major Work~~

Signature was redacted for privacy.

~~For the Major Department~~

Signature was redacted for privacy.

~~For the Graduate College~~

Iowa State University
Ames, Iowa

1987

TABLE OF CONTENTS

	Page
I. INTRODUCTION	1
A. Historical Background	1
B. Definition of the Amorphous State	3
C. Energy Bands and Dangling Bonds	3
D. Hydrogenation	8
E. Scope of This Research	12
II. SAMPLE PREPARATION	13
III. SAMPLE CHARACTERIZATION	20
A. Mechanical Thickness Measurements	20
B. Optical Measurements	20
C. Infrared Measurements	35
D. ESR Measurements	46
IV. RESULTS of He, Ar and Xe SPUTTERING	53
A. Introductory Comments	53
B. Deposition Rates	53
C. Hydrogen Concentrations	64
D. Unpaired Dangling Bond Spin Densities	83
E. Optical Measurements	95
F. Summary of Results and Conclusions	101
V. MULTILAYERED FILMS of $a\text{-Si}_{1-x}\text{:H}_x/a\text{-Si}_{1-y}\text{:H}_y$	105
A. Introductory Comments	105
B. Sample Preparation	108
C. Multilayer Structure Measurements	111
1. X-ray diffraction	111
2. Optical transmission	113
3. REELS measurements	123
D. Hydrogen Motion in $a\text{-Si:H}$	131
E. Conclusions	138
VI. REFERENCES	142

LIST OF FIGURES

	page
Fig. 1. On the right is the electronic structure of silicon as determined by nearest neighbor bonds. On the left is the electronic structure of silicon as determined by a band model	6
Fig. 2. Davis-Mott model of the electronic density of states in amorphous silicon, showing the valence band, conduction band, valence band mobility edge (E_v), conduction band mobility edge (E_c), valence band localized tail states (E_v to E_b), conduction band localized tail states (E_c to E_a), and the T_3° and T_3^{-} dangling bond states near the middle of the gap	9
Fig. 3. Schematic diagram of the r.f. sputtering system	14
Fig. 4. Voltage vs time characteristics for the source, V_a , and the target, V_b , in a r.f. sputtering system. The period of the voltage source is τ	16
Fig. 5. Schematic representation of mechanical thickness measurements	21
Fig. 6. Optical system in the Cary Model 14A spectrophotometer used in this work	22
Fig. 7. Transverse electromagnetic waves normally incident on a surface at $y=0$	24
Fig. 8. Multiple reflections from two reflecting surfaces	26
Fig. 9. A schematic representation of the absorption spectrum of amorphous semiconductors. The regions A, B, and C are discussed in the text	32

	page
Fig. 10. A a-Si:H infrared spectrum. The dashed line is the assumed approximate baseline	38
Fig. 11. Abs (defined in the text) vs. wave number for sample number 115. Note that this sample does not have either the 2100 cm^{-1} stretching band or the $850\text{--}890\text{ cm}^{-1}$ bending mode	39
Fig. 12. Schematic illustration of the bond-stretching (top row), bond-bending (middle row), and bond wagging and rocking (bottom row) modes of SiH, SiH ₂ , and SiH ₃ groupings in either hydrogenated a-Si or gaseous silanes. The frequencies in cm^{-1} are those seen in hydrogenated a-Si. The solid circles represent Si atoms, the open circles represent H atoms. Only the relevant bonds to one central Si are shown, the other Si bonds can be connected to either Si or H atoms. Ref. 29	40
Fig. 13. An infrared absorption spectrum of sample #132. The peaks (from left to right) are the Si-H stretching band at $\sim 2100\text{ cm}^{-1}$, the Si-O bending mode at $\sim 110\text{ cm}^{-1}$, the Si-H bending band at $890\text{--}850\text{ cm}^{-1}$, and the Si-H wagging mode at $\sim 640\text{ cm}^{-1}$. Note the large interference fringes from 40000 cm^{-1} to 1200 cm^{-1}	56
Fig. 14. Typical optical density vs. wavelength spectrum	57
Fig. 15. A typical ESR first derivative absorption spectrum	58
Fig. 16. Deposition rate vs. sputtering power for the r.f. sputtered a-Si:H samples	59

	page
Fig. 17. Schematic description of the voltage distribution in a r.f. sputtering process. V_p is the sheath voltage between the plasma and substrate; and, V_{SB} is the naturally occurring self-bias which is responsible for the sputtering of the target	62
Fig. 18. Predicted vs. observed deposition rates for a-Si:H prepared by r.f. sputtering	63
Fig. 19. Total hydrogen concentration vs. deposition rate for the three sets of r.f. sputtered a-Si:H films	66
Fig. 20a. $-\ln(1-[H_T]/[H_T]_{max})$ vs. $1/R$ for the helium sputtered a-Si:H films, where $[H_T]$ is the total hydrogen concentration and R is the deposition rate	68
Fig. 20b. $-\ln(1-[H_T]/[H_T]_{max})$ vs. $1/R$ for the argon sputtered a-Si:H films, where $[H_T]$ is the total hydrogen concentration and R is the deposition rate	69
Fig. 20c. $-\ln(1-[H_T]/[H_T]_{max})$ vs. $1/R$ for the xenon sputtered a-Si:H films, where $[H_T]$ is the total hydrogen concentration and R is the deposition rate	70
Fig. 21. $[Si-H_2]$ vs. deposition rate for the three sets of r.f. sputtered a-Si:H films	73
Fig. 22a. $[SiH_2]^{1/2}$ vs. $[H_T]$ for the helium sputtered a-Si:H films	76
Fig. 22b. $[SiH_2]^{1/2}$ vs. $[H_T]$ for the argon sputtered a-Si:H films	77
Fig. 22c. $[SiH_2]^{1/2}$ vs. $[H_T]$ for the xenon sputtered a-Si:H films	78

	page
Fig. 23. $[\text{SiH}_2]^{1/2}/[\text{H}_T]$ vs. sputtering power for the helium sputtered a-Si:H films	81
Fig. 24. Unpaired dangling bond spin density vs. sputtering power for the three sets of r.f. sputtered a-Si:H films	85
Fig. 25. Unpaired dangling bond spin density vs. deposition rate for the three sets of r.f. sputtered a-Si:H films	86
Fig. 26. Unpaired dangling bond spin density vs. $[\text{H}_T]$ for the three sets of r.f. sputtered a-Si:H films	88
Fig. 27a. Unpaired dangling bond spin density vs. $[\text{Si-H}_2]$ for the Ar and Xe sputtered a-Si:H films	89
Fig. 27b. Unpaired dangling bond spin density vs. $[\text{Si-H}_2]$ for the He sputtered a-Si:H films	90
Fig. 28. Unpaired dangling bond spin density vs. $[\text{Si-H}_2]$ which show increasing ρ_{DB} with increasing $[\text{H}_T]$	92
Fig. 29. Relative density of weak Si-Si bonds ([WB]) vs. sputtering power for the three sets of r.f. sputtered a-Si:H films	94
Fig. 30. $\sqrt{E_{\text{cut}}}$ vs. E plots for the He, Ar, and Xe r.f. sputtered a-Si:H films	96
Fig. 31. $E_{\text{gag}}^{\text{optical}}$ vs. $[\text{H}_T]$ for the three sets of r.f. sputtered a-Si:H films	97
Fig. 32. $\ln \alpha$ vs. E for determination of the Urbach edge coefficient	100

	page
Fig. 33. Schematic representation of quantum well confinement in semiconductor superlattices as proposed by Esaki and Tsu. CB and VB are the conduction and valence band edges, respectively, the hatched regions are the new allowed bands formed by the periodic quantum well structure, and l is the period of the superlattice	106
Fig. 34. X-ray diffraction data for $a\text{-Si}_{1-x}\text{H}_x/a\text{-Si}_{1-y}\text{H}_y$ multilayer number 147	114
Fig. 35. X-ray diffraction data for $a\text{-Si}_{1-x}\text{H}_x/a\text{-Si}_{1-y}\text{H}_y$ multilayer number 157	115
Fig. 36. Optical density vs. wavelength spectrum for multilayer sample number 119. Note the interference fringe at high optical densities	118
Fig. 37. Optical density vs. wavelength spectrum for multilayer sample number 139. Note the "strange" interference fringe from 780 to 700 nm	119
Fig. 38. Optical density vs. wavelength spectrum for multilayer sample number 146. Note the "strange" interference fringe from 810 to 700 nm	120
Fig. 39. First derivative REELS spectra taken at $E_p = 100$ eV from an $a\text{-Si:H}$ film containing 27 at.% hydrogen (a) and from another $a\text{-Si:H}$ film containing 0 at.% hydrogen (b). Small but reproducible changes between the spectra are observed over a loss energy range from 1.5 to 18 eV. The parameter R , used to determine the <u>bulk</u> hydrogen concentration is also shown	126

- | | page |
|--|------|
| Fig. 40. The linear dependence of R on <u>bulk</u> hydrogen concentration is demonstrated | 128 |
| Fig. 41a. A REELS depth profile of a multilayer specimen consisting of alternating hydrogen concentration layers of a-Si:H. One period consists of a high hydrogen concentration layer containing 24 at.% hydrogen and a low hydrogen layer contains 8 at.% H | 129 |
| Fig. 41b. An expanded view of a portion of the depth profile shown in (a) illustrating the scatter in the data and the interfacial broadening | |
| Fig. 42. Second derivative REELS spectra taken at $E_p = 196$ eV from an a-Si:H film containing 27 at.% H (a) and from another a-Si:H film containing no hydrogen (b). The parameter R' is also shown | 133 |
| Fig. 43. REELS depth profile of a three layer a-Si:H sample on a silicon substrate. The two high hydrogen layers are readily distinguishable from the middle low hydrogen layer and from the silicon substrate. The three interfaces between the four regions of different hydrogen concentration are apparent in this unannealed sample | 135 |
| Fig. 44. A schematic representation of the depth profiles obtained from various three layer a-Si:H samples that had been annealed for one hr at 175°C (b), 225°C (c), 350°C (d), 400°C (e), and 500°C (f) as well as an unannealed sample (a). | 137 |

I. INTRODUCTION

A. Historical Background

Solid state physics has long been primarily concerned with crystalline materials. The periodic nature of crystalline materials, and the mathematical formalism allowed by this periodicity, made theoretical investigations and explanations of observed phenomena in crystalline materials possible. Amorphous materials, which by definition have no long range order or periodicity, were not studied to the same extent as crystalline materials.

Interest in studying amorphous materials was spurred by the discovery of technological uses for these materials. For instance, the oxide glass $(\text{SiO}_2)_{0.9}(\text{GeO}_2)_{0.1}$ is used for fiber optic waveguides, the chalcogenide glasses of Se and As_2Se_3 are used in xerography, and the amorphous alloy semiconductor $\text{Te}_{0.8}\text{Ge}_{0.2}$ is used in computer memory elements. Hydrogenated amorphous silicon (a-Si:H), the material studied in this work, was found to have a very high absorption coefficient in the visible spectrum, allowing ~ 1 μm thick, solar cells to be produced.¹ The amorphous solar cells of today have a typical efficiency of ~ 10% compared to single crystal cells which have an efficiency of ~ 18%. Because of their lower cost and lighter weight, a-Si:H solar cells are becoming the dominant element in solar cell technology. More recently, a-Si:H field effect transistors have been made to use as drivers in liquid crystal flat panel displays. Also, r.f. sputtered a-Si:H is the active Xerographic element in Canon copiers.

The first modern day work on amorphous silicon was carried out by Chittick, Alexander, and Sterling in 1969.² Their films were deposited

by glow discharge decomposition of silane (SiH_4). They reported low conductivities and small dangling bond ESR signals. However, no mention was made of the presence of hydrogen in the samples. It was not until 1974 that the role of hydrogen in a-Si:H was discovered. Lewis and his collaborators³ intentionally introduced hydrogen into a-Ge and found a reduction in ESR dangling bond density and an increase in resistivity with increasing hydrogen concentration. From these results, they concluded that hydrogen passivates dangling bonds and thereby removes allowed electron energy levels which were near the Fermi levels. Thus electron "hopping" through these states was eliminated. This caused the increase in the resistivity. Spear and LeComber also assumed that if this was true for a-Ge, it should also be true for a-Si. This conclusion was proven by their work in 1976 on a-Si:H⁴. The presence of hydrogen in glow discharge produced a-Si was confirmed by the hydrogen evolution experiments of Triska et al.⁵

Early attempts to produce n- or p-type doped a-Si failed. This was due to the large number of dangling bond states near the center of the gap which effectively pinned the Fermi level at this energy. This effect should be compensated for by the incorporation of hydrogen. Indeed, in 1975 Spear and LeComber reported that a-Si could be doped n-type or p-type by the addition of PH_3 or B_2H_6 into the SiH_4 plasma.⁶ However, they did not realize the important role hydrogen played in this doping. In 1976, Paul et al. demonstrated that r.f. sputtered a-Si:H could be doped both p and n type if hydrogen was also added to the plasma.⁴ With the discovery that a-Si:H could be made p or n type by doping, interest in a-Si:H as a semiconductor material developed.

B. Definition of the Amorphous State

Amorphous semiconductors are noncrystalline in that they lack long-range periodic ordering of their constituent atoms. However, amorphous semiconductors are not completely disordered on the atomic scale. Local chemistry provides almost rigorous bond lengths and constraints on bond angles. For example, in ideal a-Si all of the Si atoms would be bonded to four other Si atoms with nearest neighbor distances fixed at 2.45 Å and only the bond angles allowed to vary from those of the crystalline case. This would then allow for no unfilled bonding orbitals (dangling bonds). However, it has been shown⁷ that this ideal amorphous silicon exists in concept only. Dangling bonds are intrinsic to a-Si implying some of the Si atoms are bound to less than four other Si atoms. Also, weak bonds exist with bonding lengths deviating from 2.45 Å. Both of these defects involve only a few percent of the silicon atoms in pure (non-hydrogenated) amorphous silicon. In practice, a material is empirically defined to be amorphous if its x-ray diffraction pattern consists of diffuse rings (halos) rather than sharply defined Bragg rings or spots characteristic of polycrystalline or single crystal solids.

C. Energy Bands and Dangling Bonds

Much of the work done in solid state physics involves crystalline materials. The natural process to follow in considering a crystalline material involves assuming a periodic potential due to the periodic positioning of the atoms in the crystal. The allowed energies for an electron in such a potential are then solved for with the help of

Bloch's theorem and appropriate boundary conditions. This gives a relationship between the allowed energies of the electron and its wave vector. Typically, there will exist bands of such allowed energies separated by gaps of forbidden energies. Thus, the picture of energy bands and energy gaps seems to be directly related to the periodic nature of crystalline materials.

However, in amorphous semiconductors, no long range order exists and the concept of a wave vector becomes meaningless. Still, energy bands and band gaps are observed in amorphous semiconductors. In an amorphous semiconductor, as in a crystalline semiconductor, a density of states, $N(E)$ can be defined as the number of allowed single particle electron energy states per unit volume between the energies E and $E+dE$. Optical absorption and photoconductivity measurements have shown the existence of allowed energy bands separated by forbidden energy gaps in amorphous semiconductors.

To see how this might be possible, consider a single atom of silicon which has fourteen electrons. Ten of these are tightly bound core electrons which do not become involved in chemical bonding and will not be considered here. Of the outer four electrons, two are in 3s states, and two are in 3p states. These four orbitals hybridize to form four sp^3 orbitals. This involves an increase in energy corresponding to the difference in energy between a 3s and a 3p level. When four more Si atoms are brought in to enclose this Si atom in the tetrahedral structure, new orbitals are formed. These are called the bonding (lower energy) orbitals and the antibonding (higher energy) orbitals. The total energy of the four electrons in the bonding orbital is now lower

than the combined energy of two electrons in 3s orbitals plus two electrons in 3p orbitals. This lowering in energy is achieved by allowing the electrons to move over larger spatial distances and is responsible for the silicon atoms being chemically bound to each other. If many Si atoms are bound to each other in this fashion, the degeneracy of these levels is removed by broadening the levels into bands. See Fig. 1. Thus, the chemical viewpoint can explain energy bands and band gaps in both amorphous and crystalline silicon.

Using this picture, one can begin to understand the dangling bonds. A dangling bond arises when a Si atom is bound to only three other silicon atoms. This may happen at surfaces where there simply is not another Si with which to bond. Or, it may occur because of the randomness of bond angles in a-Si. Simply put, the lattice may become distorted enough to squeeze out the fourth Si atom. In either case, this leaves a silicon sp^3 orbital unpaired to another sp^3 orbital. Thus, no bonding or antibonding orbitals are formed and an available energy state is left corresponding to this sp^3 orbital. As shown in Fig. 1, this energy level lies midway between the conduction and valence bands. It is interesting to note that the first a-Si produced had 10^{19} - 10^{20} cm^{-3} of these dangling bonds; and, this high density of allowed energy levels at the middle of the gap effectively pinned the Fermi energy there. This is why initial attempts to dope a-Si failed, the dopants simply could not introduce enough allowed states to move the Fermi energy.

The exact nature of the energy bands in a-Si:H is not agreed upon, but the following basic features are well accepted.

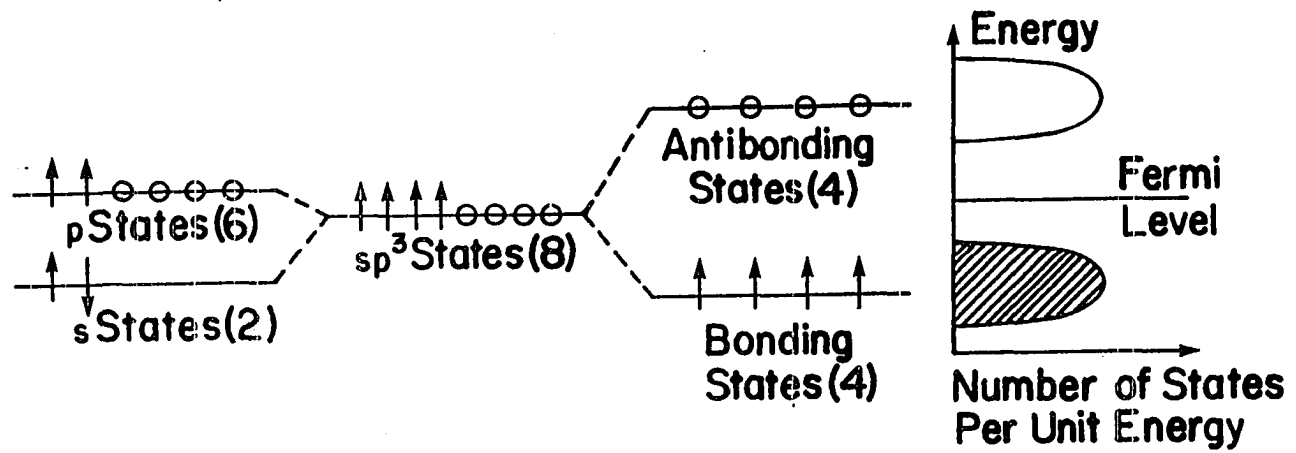


Fig. 1. On the right is the electronic structure of silicon as determined by nearest neighbor bonds. On the left is the electronic structure of silicon as determined by a band model

- 1) There exist conduction and valence bands separated by a region of very low density of states (DOS). This region of very low DOS can be thought of as a pseudogap, and will be referred to as the "energy gap" for the a-Si:H films considered in this work.
- 2) The absence of long range order smears out sharp features characteristic of the electronic DOS for crystalline silicon.
- 3) Fluctuations in short range order lead to tailing of electronic states into the gap. For greater local disorder, the tail states induced will be farther into the gap.
- 4) Because of this disorder, electrons may become "localized" or spatially confined to the vicinity of a single atom. The greater the degree of disorder in the potentials experienced by the electrons, the greater is the probability of occurrence of localized states. This localization occurs in the tail states. The first theoretical discussion of localization due to disorder was given by Anderson and is called "Anderson localization."⁸ The separation in energy between the delocalized states of the valence and conduction bands is called the mobility gap.
- 5) Dangling bonds introduce two types of states near the center of the gap. One is called the T_3° dangling bond. Here, the T indicates tetrahedral bonding, the subscript denotes the coordination, and the superscript denotes the charge state of this defect site. This is a dangling bond orbital containing one electron. The other state is the T_3^{-} . This dangling bond is doubly occupied. The insertion of the second electron costs some energy U, also called the correlation energy; therefore,

this dangling bond state is higher in energy by an amount U above the T_3° level. See Fig. 2 for a schematic description of the density of states for amorphous silicon.

D. Hydrogenation

The incorporation of hydrogen into amorphous silicon is generally accepted to have beneficial effects on the material. These effects include 1) a pronounced lowering of the density of dangling bonds, 2) a reduction in the density of electronic states in the gap, 3) an increase in the energy gap, and 4) sharper band tail edges.

The reduction in the number of dangling bonds is a result of hydrogen reacting with these bonds to passivate them. The density of dangling bonds is usually measured using electron spin resonance. This technique can only observe those electrons which are not paired with another electron of opposite spin. When hydrogen is added to a-Si, the electron of the hydrogen can form a bond with the electron in a dangling bond orbital. The spin of the hydrogen's electron then cancels that of the dangling bond's electron and no ESR signal will be observed. This ESR signal cancelling can also occur if two dangling bond orbitals stretch or bend to form a weak silicon-silicon bond.

When the hydrogen atom and the dangling bond orbital bond, two new orbitals are formed. These are bonding and antibonding orbitals. The energy level of the bonding orbital is lower than that of the dangling bond (sp^3) orbital while the energy level of the antibonding orbital is higher. The energy of the bonding orbital places this state in the valence band of the amorphous silicon. The energy of the antibonding

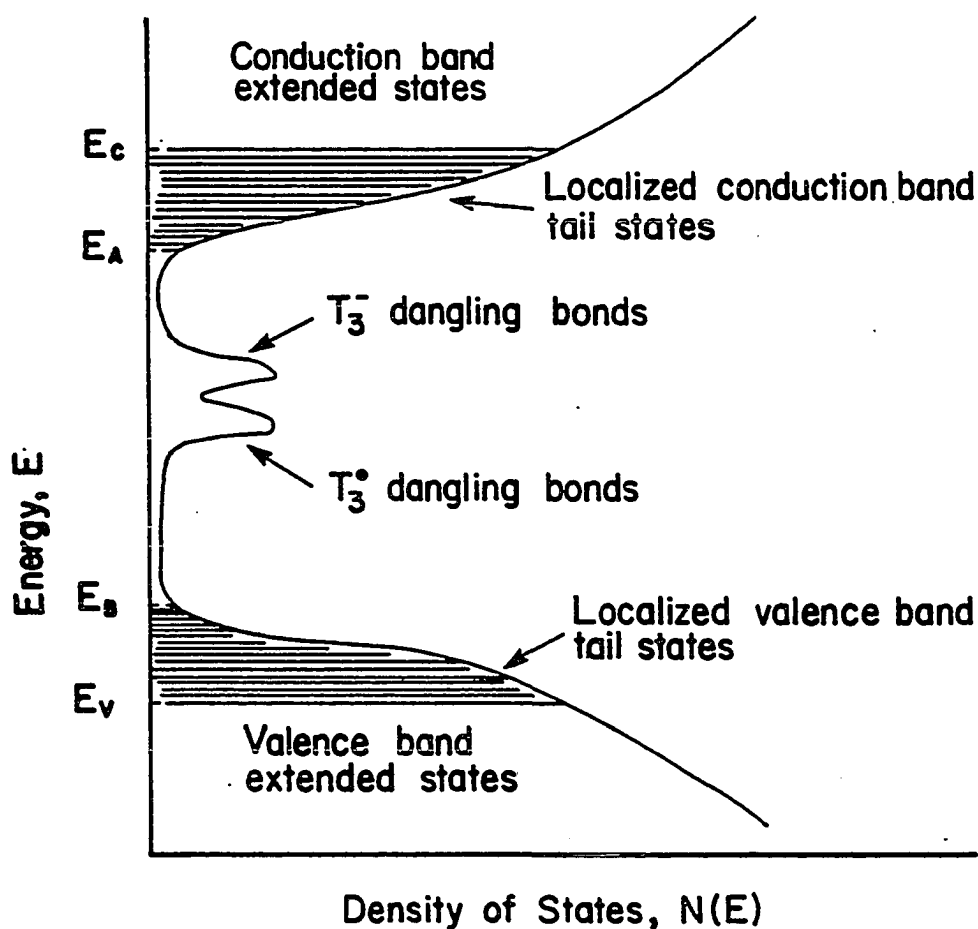


Fig. 2. Davis-Mott model of the electronic density of states in amorphous silicon, showing the valence band, conduction band, valence band mobility edge (E_v), conduction band mobility edge (E_c), valence band localized tail states (E_v to E_b), conduction band localized tail states (E_c to E_a), and the T_3^0 and T_3^- dangling bond states near the middle of the gap

orbital places this state in the conduction band of the amorphous silicon. In this way, allowed states are removed from the gap by the addition of hydrogen.

The size of the band gap has been seen to increase with increasing hydrogen incorporation.^{9,10} This could be the result of either decreasing the number of band tail states or it could be the result of silicon-hydrogen alloying. Cody et al.¹¹ believe that the addition of hydrogen allows the amorphous structure to relax to a structure more like that of crystalline silicon. Thus, there would be less deviation in local order and less tail states caused by local disorder. However, this seems unlikely, since this process could give at most an energy gap equal to that of crystalline silicon (corresponding to the case of no local disorder). The indirect energy gap of crystal silicon is 1.12 eV while energy gaps observed in hydrogenated amorphous silicon range from 1.4 eV to 2.0 eV. It should be noted that crystalline silicon does have a direct gap of 3.4 eV which is larger than the gaps observed in a-Si:H. However, this gap would only be observed in a-Si:H if momentum conservation rules made the indirect transition impossible. Since momentum conservation rules are relaxed in a-Si:H, it seems improbable that the direct gap would be the one observed in a-Si:H. Therefore, a silicon-hydrogen alloying effect seems like a more plausible explanation for the observed increase in the energy gap.

Although it is generally agreed upon that the band tail states of a-Si:H are due to some type of disorder the exact nature of the disorder that gives band tail states is uncertain. The types of disorder that could cause these tail states include 1) weak Si-Si bonds, 2) structural

defects such as microvoids and columnar morphology, 3) exotic SiH_x complexes, and 4) dangling bonds. The possibility of tail states due to dangling bonds can probably be disregarded because dangling bonds introduce states near the middle of the gap and not in the band tails.

Cody et al.¹¹ believe that the band tail states are due to local variations in Si-Si bond lengths and angles and that the incorporation of hydrogen reduces these variations. Standard treatments of band tails, known as Urbach edges, in crystalline semiconductors^{12,13} conclude that the width of the absorption edge is proportional to a thermal average of the square of the displacement of the atoms from their equilibrium positions.

The presence of microvoids and columnar morphology has been correlated to the presence of SiH_2 and SiH_3 .¹⁴⁻²⁶ It is believed that SiH_2 and SiH_3 complexes form on the surface of such structural defects. These surfaces are more likely to have silicon atoms bonded to more than one hydrogen atom because on surfaces silicon bonding orbitals are necessarily unfulfilled. Since these types of structural defects and $\text{SiH}_2/\text{SiH}_3$ complexes are always correlated, it is difficult to separate the effects of one from those of the other. However, the results of this work tend to indicate that band tail states are the result of weak Si-Si bonds on the surfaces of microvoids and columns. The surface area of these defects is assumed to be proportional to the amount of SiH_2 and SiH_3 in the films.¹⁴⁻²⁶ Thus, tail states are correlated to, but not caused by, the $\text{SiH}_2/\text{SiH}_3$ complexes.

E. Scope of This Research

Two questions are addressed in this work. The first concerns the effects of deposition conditions on the structure of r.f. sputtered hydrogenated amorphous silicon films. Three gas mixtures were used for sputtering: He/H₂, Ar/H₂, and Xe/H₂. Samples were prepared at r.f. sputtering powers ranging from 0.27 W/cm² to 3.3 W/cm² for each of these gas mixtures. All of these samples were then characterized using optical transmission, infrared, and ESR measurements. The results of these measurements were then used to show a systematic decrease in the structural disorder of the films with increasing r.f. sputtering power. It was also found that the Ar/H₂ gas mixture produced the highest quality films, while the He/H₂ gas mixture produced the lowest quality films. This was interpreted as being due to greater plasma-substrate interactions when sputtering with the Ar/H₂ mixture.

The second part of this work is concerned with hydrogen motion in r.f. sputtered a-Si:H multilayers. These multilayer films consisted of alternating layers of high and low hydrogen concentration a-Si:H. The hydrogen content as a function of depth into the films was determined using reflected electron energy low spectroscopy with ion sputter milling. The multilayer films were thermally annealed for 1 hr at temperatures ranging from 175°C to 500°C. These samples showed signs of hydrogen evolution but not of hydrogen diffusion.

II. SAMPLE PREPARATION

All samples for this work were prepared by reactive r.f. sputtering. Deposition of a thin amorphous film by r.f. sputtering is accomplished by bombarding a target of the material to be deposited with high energy ions of an inert gas. The inert gas is ionized and accelerated towards the target by an applied r.f. field. The momentum transfer between the ions and the target ejects particles of atomic dimensions from the surface of the target. These ejected particles then travel across the vacuum and deposit on a substrate. For this work, the substrates used were Corning 7059 glass slides and single crystal silicon chips. Several substrates of both types were used for each deposition to allow the various sample characterization techniques to be carried out on films prepared under identical conditions.

Prior to film deposition, the sputtering chamber (Fig. 3) was pumped down to $\sim 2 \times 10^{-7}$ torr. Then the throttle valve was closed to only three turns open in order to slow the pumping rate and thereby extend the lifetime of the turbomolecular pump. Then hydrogen was introduced to the system. The rate at which hydrogen flowed into the chamber was controlled by a micrometer valve to obtain the desired partial pressure of hydrogen. For this work, the partial pressure of hydrogen was usually set at 0.5 mtorr. Next, the inert gas (He, Ar, or Xe) was introduced into the chamber; and, its flow rate was also controlled by a micrometer valve. The partial pressure of the inert gas was set at 10 mtorr, giving a total pressure in the sputtering chamber of 10.5 mtorr.

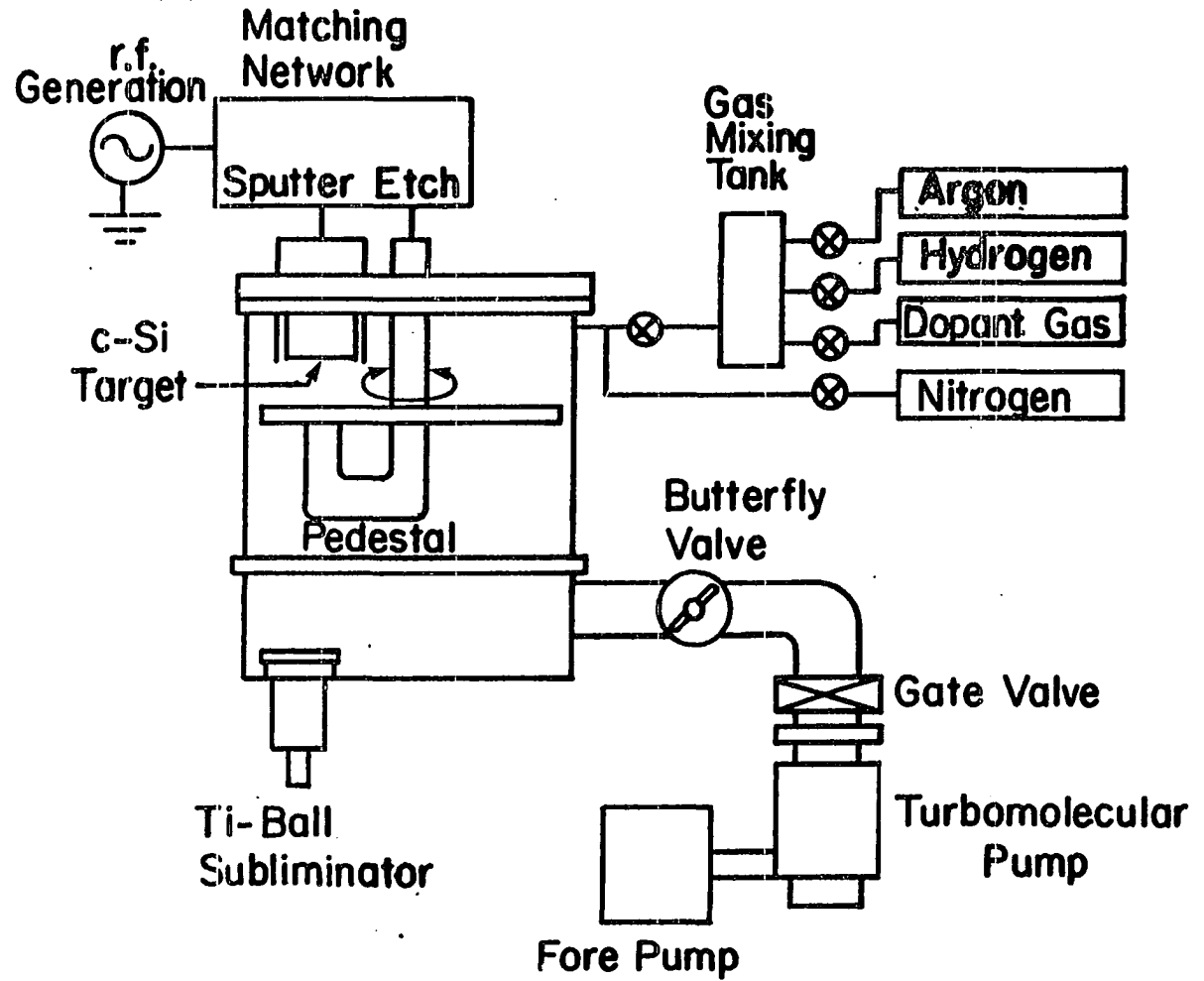


Fig. 3. Schematic diagram of the r.f. sputtering system .

After the desired gas flow rates and pressures were achieved, r.f. power was applied to the target while the pedestal, on which the substrates were held, was grounded. The r.f. field induced between the target and pedestal then accelerated free electrons and ions in the gas. These charged particles then collided with other gas atoms causing the gas atoms to become ionized. In this way, the number of charged species was increased until a plasma was formed. When the target was held at a negative potential, the positive ions in the plasma were attracted to the target. As the ions arrived at the target they reduced the target's negative bias. Because the potential of the target was alternated at a very high frequency (13.56 MHz), the positive ions were not able to reduce the negative potential of the target to zero before the r.f. power supply switched this potential to a positive value. When the target's potential was positive, it attracted the negatively charged electrons in the plasma. As the electrons impinged on the target, they reduced the target's positive potential. Because electrons are much lighter and hence faster than ions, they were much more effective in reducing the positive bias of the target. In this way, the average potential of the target was reduced from zero to some negative value. Figure 4 depicts the r.f. voltage supplied by the power source, V_a , and the potential at the target, V_b . This naturally occurring self-bias of the target causes the positive ions in the plasma to bombard the target surface.

The target for this work was a polycrystalline silicon plate 15 cm in diameter and of 99.999 percent purity manufactured by the Materials Research Corporation. As this target was struck by the inert gas ions,

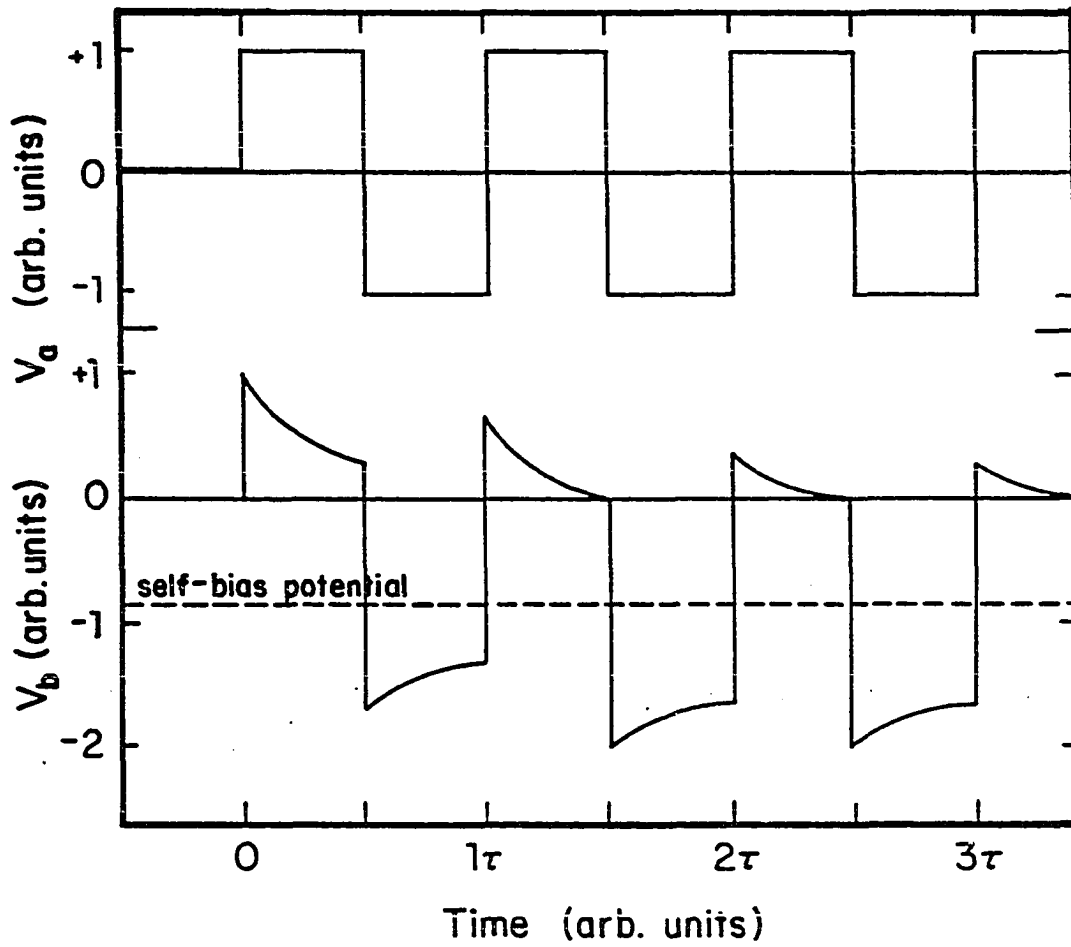


Fig. 4. Voltage vs time characteristics for the source, V_a , and the target, V_b , in a r.f. sputtering system. The period of the voltage source is τ

the momentum transfer ejected atoms of silicon which then traversed the chamber to the substrates on the pedestal. The substrates were held approximately one inch from the target. As the amorphous silicon film deposited on the substrates, hydrogen in the plasma reacted with the silicon. This hydrogen incorporation gave hydrogenated amorphous silicon, a-Si:H.

Both the target and the pedestal were water cooled to avoid excessive heating. To maximize the power transmitted through the target, an r.f. power matching system was used. This matching system consisted of two variable capacitors connected, one in series and the other in parallel, to the capacitor formed by the target and pedestal. By adjusting the values of these capacitors, it was possible to maximize the power transmitted through the target while holding the power reflected from the target at less than 2.5 watts. The transmitted power used varied from 50 watts (0.27 W/cm^2) to 600 watts (3.3 W/cm^2). The inert gases used were helium, argon, and xenon.

Samples prepared in a helium/hydrogen atmosphere demonstrated post-depositional oxidation. After a film was prepared by helium sputtering, but before it was removed from the vacuum chamber, it was coated with a film sputtered in an argon/hydrogen atmosphere to protect it from post-depositional oxidation. These coatings were $\sim 500 \text{ \AA}$ thick and sputtered with 50 W (0.27 W/cm^2) transmitted power.

Multilayer films were also prepared. These films consisted of alternating layers of high and low hydrogen concentration a-Si:H. The multilayer samples were prepared in the same manner as the single layer films described above except that the transmitted r.f. power was

alternated between 50 and 600 watts during deposition. By changing the r.f. power, the hydrogen concentration of the film being deposited was changed. At high r.f. transmitted power the rate at which silicon was ejected from the target, and subsequently deposited on the substrate, was also high. Typically, at 600 W transmitted power, the deposition rate was $\sim 5 \text{ \AA}/\text{sec}$. When low power was used (50 W) a deposition rate of $\sim 1 \text{ \AA}/\text{sec}$ was observed. However, the flux of hydrogen at the surface of the substrate depended primarily on the partial pressure of hydrogen in the vacuum chamber. Thus, depositions at higher r.f. sputtering powers gave lower concentrations of hydrogen. Using the deposition rates observed for homogeneous films prepared with 50 W and 600 W transmitted power, it was possible to alternate the sputtering power from 50 W and 600 W and from 600 W to 50 W at the appropriate times to give layers of the desired thickness. Layer thicknesses used ranged from 60 to 2000 \AA .

It has been found that the following measures are helpful when preparing r.f. sputtered a-Si:H in the sputtering system of Ames Laboratory.

- 1) One should measure the hydrogen partial pressure first and then introduce the inert sputtering gas. The partial pressure of the inert gas can be found by subtracting the partial pressure of hydrogen from the total pressure.
- 2) The output pressures of the gas bottles should be held constant. In this way, the setting of the micrometer valves needed to produce a desired pressure in the system will remain almost constant.

- 3) It has been found to be easiest to first adjust the "load" capacitor and then the "tuning" capacitor of the r.f. matching system.
- 4) All water lines and filters should be cleaned regularly (about once a month) to insure proper cooling of the target and pedestal.
- 5) Removing built-up deposits of a-Si:H from the pedestal should be done with caution. It has been found that significantly higher deposition rates occur when the majority of the pedestal is coated with a thick insulating layer of a-Si:H.
- 6) The substrates should always be placed in the same position on the pedestal. This will allow one to avoid problems related to the deposition being non-homogeneous over the entire pedestal.

III. SAMPLE CHARACTERIZATION

A. Mechanical Thickness Measurements

Film thickness was measured using a Dektak stylus profilometer. A step of the same thickness as the film was formed by masking part of a Corning glass substrate with a strip of metal before sputtering. The height of this step was measured after sputtering with the Dektak stylus profilometer. Figure 5 gives a schematic depiction of this technique.

B. Optical Measurements

A Cary Model 14A spectrophotometer was used to measure optical density vs. wavelength for the films used in this work. A Schematic representation of the Cary can be found in Fig. 6. Optical density (OD) is defined as

$$OD = \log_{10} \left(\frac{I_0}{I} \right), \quad (1)$$

where I_0 is the intensity of the incident light and I is the intensity of the transmitted light. The Cary spectrophotometer is a dual beam instrument. One beam is passed through a reference compartment while the other beam passes through the sample compartment. The sample was placed in its compartment such that the incident light impinged on the sample parallel to the sample's surface normal. The reference compartment was left empty for reasons described below. The Cary automatically adjusted the size of the entrance slits of these compartments to balance the intensity of the two exiting beams. The ratio of the two slit sizes gave the ratio of I_0 to I , mentioned above.

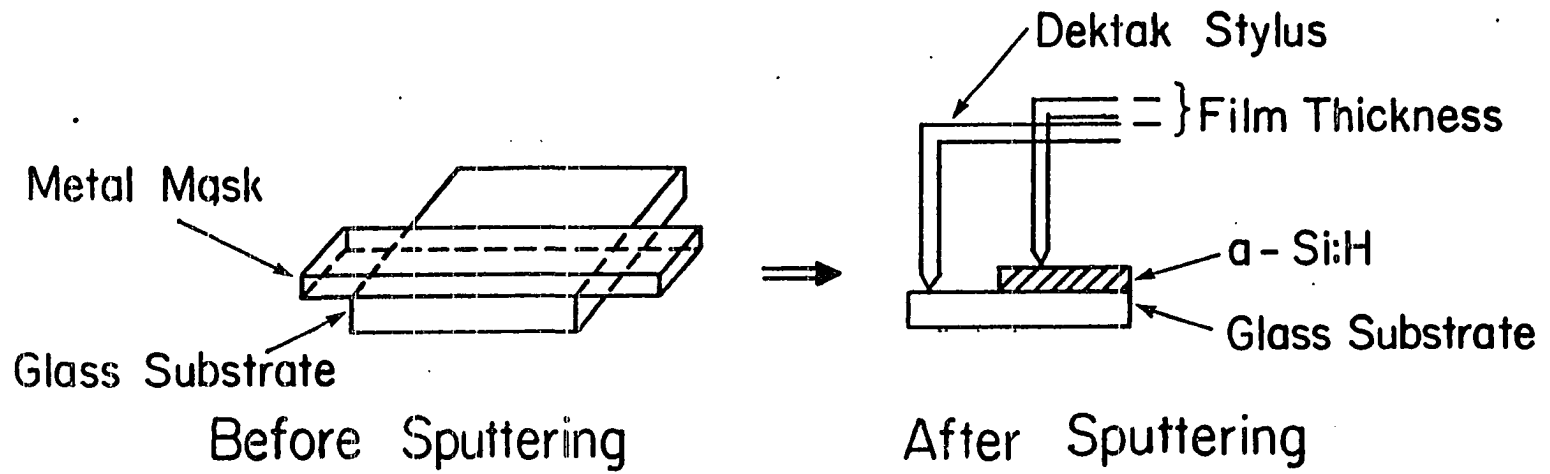


Fig. 5. Schematic representation of mechanical thickness measurements

The light source for the Cary was a General Electric quartzline lamp. By using the monochromator of the Cary, it was possible to scan the wavelength of the light sent through the reference and sample compartments from 2000 to 350 nm. As the wavelength was scanned, the optical density was measured and this information was plotted out on a strip chart recorder. In practice, the optical density was measured for wavelengths from 1000 nm down to the wavelength which gave an optical density of two, as this was the largest optical density the Cary spectrophotometer was capable of measuring. It should be noted that an optical density of two corresponds to a transmission of one percent and an absorption coefficient on the order of 10^4 cm^{-1} .

The absorption coefficient vs. wavelength was found from the optical density vs. wavelength data. To understand the relationship between the absorption coefficient and optical density, it is easiest to start by considering transverse waves normally incident on a surface at $y = 0$ as in Fig. 7. For $y < 0$ let the complex index of refraction be $\bar{n}_0 = n_0 + ik_0$; and for $y > 0$ let the complex index of refraction be $\bar{n}_1 = n_1 + ik_1$. This gives the form of the three waves in question to be

$$\vec{E}_{\text{incident}} = \vec{E}_0 \exp(-i \frac{2\pi\bar{n}_0 Y}{\lambda} + i\omega t), \quad (2a)$$

$$\vec{E}_{\text{reflected}} = r_{01} \vec{E}_0 \exp(i \frac{2\pi\bar{n}_0 Y}{\lambda} + i\omega t), \quad (2b)$$

$$\vec{E}_{\text{transmitted}} = \tau_{01} \vec{E}_0 \exp(-i \frac{2\pi\bar{n}_1 Y}{\lambda} + i\omega t) \quad (2c)$$

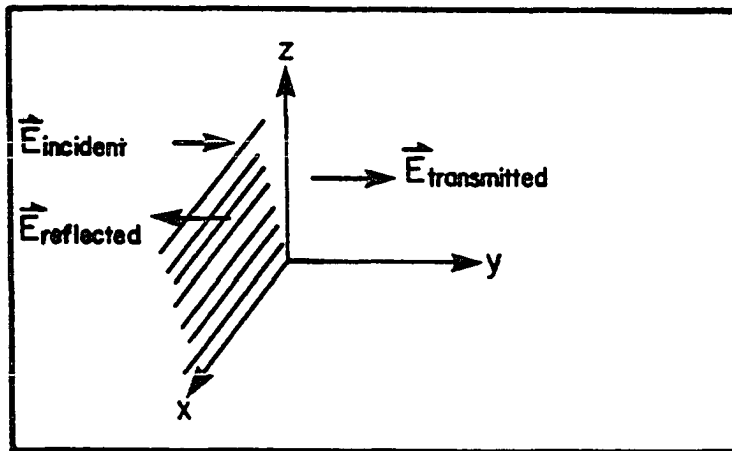


Fig. 7. Transverse electromagnetic waves normally incident on a surface at $y=0$

where

$$r_{01} = \frac{\bar{n}_0 - \bar{n}_1}{\bar{n}_0 + \bar{n}_1}, \quad (3)$$

and

$$\tau_{01} = \frac{2\bar{n}_0}{\bar{n}_0 + \bar{n}_1}. \quad (4)$$

In the preceding equations, λ , ω , and t take on the usual meanings of wavelength, angular frequency, and time, respectively.

Now consider the case of two reflecting surfaces as in Fig. 8. Not considering multiple reflections, \vec{E}_2 is given by

$$\vec{E}_2 = \vec{E}_0 \tau_{01} \tau_{02} e^{-\alpha d/2} \quad (5)$$

where

$$\alpha \equiv \frac{4\pi k_1}{\lambda}. \quad (6)$$

The absorption coefficient, α , is defined by Eq. (6). With multiple reflections, \vec{E}_2 becomes

$$\begin{aligned} \vec{E}_2 &= \vec{E}_0 \tau_{01} \tau_{12} e^{-\alpha d/2} \sum_{m=0}^{\infty} r_{12}^m r_{10}^m e^{-m\alpha d} e^{-i(4m\pi_1 md)/\lambda} \\ &= \vec{E}_0 \tau_{01} \tau_{13} e^{-\alpha d/2} \frac{1}{1 - r_{12} r_{10} e^{-\alpha d} e^{-i(4m\pi_1 md)/\lambda}} \quad (7) \end{aligned}$$

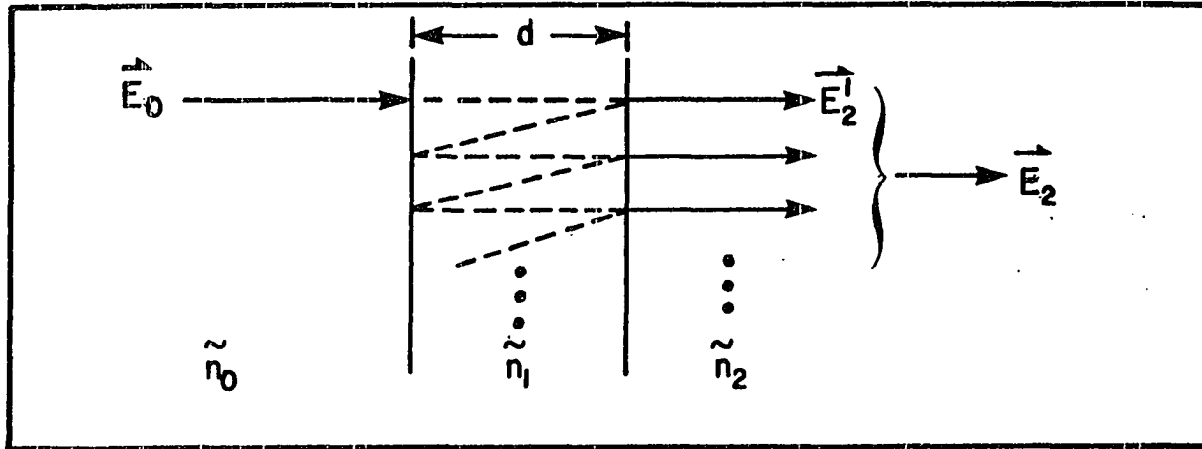


Fig. 8. Multiple reflections from two reflecting surfaces

Where $\sum_{m=0}^{\infty} x^m = \frac{1}{1-x}$ for $|x| < 1$ has been used. Assuming $\bar{n}_0 = 1$ (as is

the case for air) and $\bar{n}_2 = 1.53$ (as is the case for the transparent Corning 7059 glass) and using the definition of transmission

$$T = \frac{I}{I_0} = \frac{n_2}{n_0} \frac{|E_2|^2}{|E_0|^2}, \quad (8)$$

it is easy to show that

$$T = \frac{(1 - R_1)(1 - R_2)e^{-\alpha d}}{1 + R_1 R_2 e^{-2\alpha d} - 2(R_1 R_2)^{1/2} e^{-\alpha d} \cos(4\pi n_1 d/\lambda)} \quad (9)$$

where

$$R_1 \equiv \left| \frac{(\bar{n}_1 - \bar{n}_0)^2}{(\bar{n}_1 + \bar{n}_0)} \right|, \quad (10a)$$

and

$$R_2 \equiv \left| \frac{(\bar{n}_2 - \bar{n}_1)^2}{(\bar{n}_2 + \bar{n}_1)} \right|. \quad (10b)$$

R_1 and R_2 are the film-air interface and film-substrate interface reflection coefficients, respectively.

For this work, it was assumed that $k_1^2 \ll (n_1 - n_0)^2, (n_2 - n_1)^2$ which allows R_1 and R_2 to be written as

$$R_1 \equiv \frac{(\bar{n}_1 - 1)^2}{(\bar{n}_1 + 1)^2}, \quad (11a)$$

and

$$R_1 \equiv \frac{(\bar{n}_1 - 1.53)^2}{(\bar{n}_1 + 1.53)^2}, \quad (11b)$$

This assumption is valid since $n_1 \approx 3.5$ and the maximum value for k_1 is $\approx 10^{-2}$ (this value of k_1 can be found by using $k_1 = \alpha\lambda/4\pi$ and the maximum value of α of $\sim 10^{+4} \text{ cm}^{-1}$ at a wavelength of $\lambda \sim 500 \text{ nm}$). Also, the $\cos(4\pi nd/\lambda)$ term in the denominator of Eq. (9) gives rise to interference fringing. As α grows larger, this term becomes smaller. Thus, when data are taken in the wavelength region in which there are no interference fringes, it is deduced that $2(R_1 R_2)^{1/2} e^{-\alpha d} \ll 1$ and so this term can be ignored. Then, obviously, the $R_1 R_2 e^{-2\alpha d}$ term can also be ignored, since it is the square of a number small compared to unity. Using these simplifying assumptions, Eq. (9) reduces to

$$T = (1 - R_1)(1 - R_2)e^{-\alpha d}. \quad (12)$$

To find R_1 and R_2 , it was necessary to find the index of refraction for the film, n_1 . The index of refraction of the film was found by using the position of the interference fringes in the optical density

vs. wavelength data. For a maximum in transmission (minimum in the optical density)

$$2n_1d = m\lambda \quad (13)$$

where m is an integer giving the order of the interference fringe. For a minimum in transmission (maximum in the optical density)

$$2n_1d = \left(m + \frac{1}{2}\right) \lambda \quad (14)$$

Algebraic manipulations of Eqs. (13) and (14) give

$$n = \frac{\lambda_1 \lambda_2}{4d(\lambda_1 - \lambda_2)} \quad (15)$$

if the index of refraction is assumed to be independent of wavelength. In general, the index of refraction depends on wavelength. Therefore, the index of refraction was found at several wavelengths in the region where interference fringes were observed and linearly extrapolated into the wavelength region where there were no interference fringes.

At this point, it becomes apparent why the reference compartment was left empty while taking the optical density measurements. It may seem that in order to compensate for the small absorption by the glass substrate, one should have placed a blank glass substrate in the reference compartment. However, if this is done, it creates the need to compensate for the difference in reflection coefficients between a glass-air interface and a glass-film interface. This is because in the reference compartment there would be reflections from the glass-air interface whereas in the sample compartment there would be reflections from a glass-film interface. In practice, R for a glass-air interface is ~ 0.06 while R for a glass-film interface is ~ 0.16 . Therefore, it

is easier, and more accurate, to compensate for absorption in the glass substrate by measuring the transmission of the glass, T_g , and multiplying the expression above by T_g . The glass was found to have a transmission of 0.97 independent of wavelength for the wavelength region of interest. This gives, using the definition of optical density,

$$10^{-OD} = T_g(1 - R_1)(1 - R_2)e^{-\alpha d} \quad (16)$$

or

$$\alpha = -\frac{1}{d} \ln \left[\frac{10^{-OD}}{[T_g(1 - R_1)(1 - R_2)]} \right] \quad (17)$$

The determination of the absorption coefficient for the He sputtered films was complicated by these films being coated with an Ar sputtered layer to prevent post-depositional oxidation. The coating layer was a 500 Å thick layer of a-Si:H sputtered in 10 mt Ar and 0.5 mt H₂ with a transmitted sputtering power of 50 W (0.27 W/cm²). To account for absorption in this coating, Eq. (17) was replaced with

$$\alpha_{He} = \frac{1}{d} - \ln \left[\frac{10^{-OD}}{[T_g T_c (1 - R_1)(1 - R_2)]} \right] \quad (18)$$

where

$$T_c = e^{-\alpha_c d_c} \quad (19)$$

= transmission of the coating.

Here d_c was 500 Å and α_c was taken from the data collected on the single thick film sputtered in Ar at 50 W (0.27 W/cm²).

The optical energy gap was determined using a method suggested by Tauc et al.²⁷ In a perfect crystalline semiconductor there are no allowed states in the energy gap. Therefore, photons with energies $h\omega < E_{\text{gap}}$ cannot cause electronic transitions across the gap; and, $\alpha(E) = 0$ for $E < E_{\text{gap}}$. Photons with energies greater than E_{gap} can cause electronic transitions across the gap and so $\alpha(E) > 0$ for $E > E_{\text{gap}}$. Thus, the change from zero to nonzero α gives the energy gap for perfect crystalline semiconductors. In amorphous semiconductors the density of allowed states in the "gap" is large enough to allow photons of all energies to cause transitions. Thus, for amorphous semiconductors α is never equal to zero, but an optical energy gap can be defined by extrapolating α to zero from the high absorption region.

Amorphous silicon, and other amorphous semiconductors, shows three qualitatively different absorption regions. This is depicted in Fig. 9. The low energy, low absorption region A arises from transitions involving defect states, and will not be discussed here. Region B absorption is dominated by transitions from tail states to either other tail states or extended states and is observed to grow exponentially with energy. Region C absorption is dominated by transitions from valence band states to conduction band states. In this high energy, high absorption region the dependence of the absorption coefficient on the exciting photon's energy is controlled by the valence and conduction band shapes for band energies removed from the band tails. Away from the band tails, the conduction and valence bands are assumed to be parabolic. Extrapolation of the absorption coefficient at these high energies to zero gives a value for the optical band gap. To see how

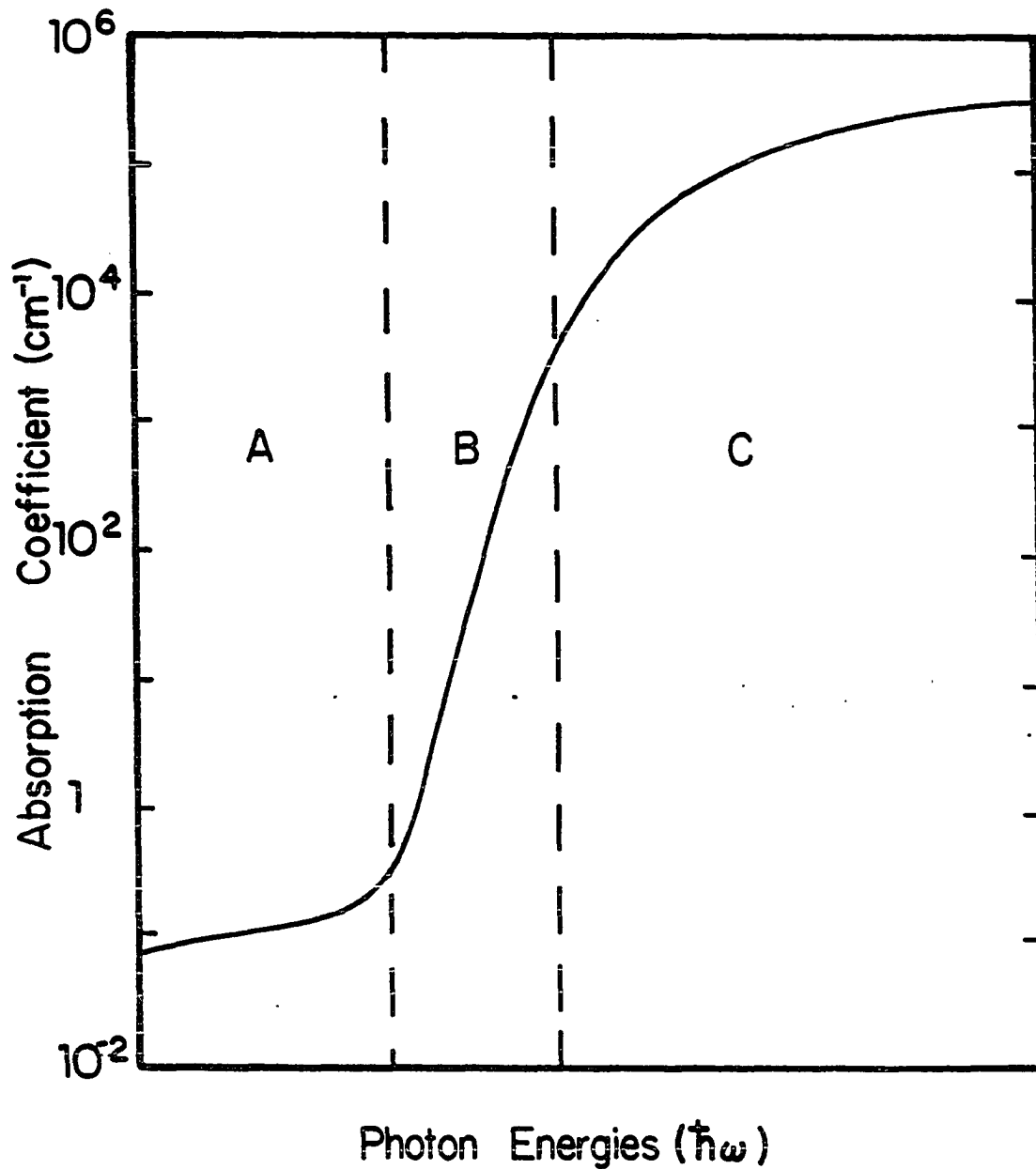


Fig. 9. A schematic representation of the absorption spectrum of amorphous semiconductors. The regions A, B, and C are discussed in the text

this is done, the dependence of the absorption coefficient on energy must be deduced.

The dependence of the absorption coefficient on the frequency, and hence energy, of the exciting photon can be deduced from the general one electron expression for the imaginary part of the dielectric constant. From Lax,²⁸ we have

$$\epsilon_2(\omega) = \frac{2}{V} \left(\frac{2\pi e}{m\omega} \right)^2 \sum_{if} |\langle f|P|i\rangle|^2 \delta(E_f - E_i - \hbar\omega) \quad (20)$$

where

- $\epsilon_2(\omega)$ = imaginary part of the dielectric constant,
- V = sample volume,
- P = momentum operator,
- ω = angular frequency of the exciting photon,
- $|i\rangle$ = initial electron state,
- E_i = energy of the initial state,
- $|f\rangle$ = electron's final state, and
- E_f = energy of the final state.

Before ϵ_2 can be evaluated, some assumptions must be made. In crystalline materials there exist momentum conservation rules which select those transitions that will be allowed. In amorphous materials only short range order exists and, therefore, short coherence lengths for the electronic wavefunctions. The coherence length being on the order of an atomic spacing results in the uncertainty in the wavevector being on the order of the wavevector. This leads to a relaxation of momentum conservation rules. Averaging Eq. (20) over initial and final states gives

$$\epsilon_2(\omega) = 2 \left(\frac{2\pi e}{m\omega} \right)^2 a^3 P_{av}^2 \int_0^{\hbar\omega} dE g_i(-E) g_f(\hbar\omega - E) \quad (21)$$

where it has been assumed that the matrix element, P_{av} , is independent of ω . Here, g_i and g_f are the density of initial and final states, respectively, and a is the average atomic spacing.

If parabolic bands are assumed, i.e., $g \propto \sqrt{E}$, then Eq. (21) gives

$$\epsilon_2(\omega) = K \frac{P_{av}^2}{\omega^2} (\hbar\omega - E_g)^2 \quad (22)$$

where K is a constant and all other terms have been defined earlier.

This can be rewritten as

$$\alpha = \frac{\omega}{nc} \epsilon_2 = K \frac{P_{av}^2}{nc\omega} (\hbar\omega - E_g)^2, \text{ or} \quad (23)$$

$$\sqrt{\alpha E n} = C(E - E_g) \quad (24)$$

where

$$C = (K P_{av}^2 h/c)^{1/2}. \quad (25)$$

The optical energy gap is then determined by plotting $\sqrt{\alpha E n}$ vs. E , for those values of α that correspond to transitions between parabolic bands, and then extrapolating $\sqrt{\alpha E n}$ to zero. The energy gap is then assigned the value of E at which $\sqrt{\alpha E n}$ is equal to zero.

The value of the constant C in Eq. (24) depends on K and P_{av} . In turn, the constant K depends on the density of states in the valence and conduction bands. If g is taken to be proportional to $N\sqrt{E}$, then K is proportional to $N_v N_c$. Also, P_{av} is a measure of the overlap of

electronic wavefunctions and as such should be related to the density and order of the amorphous system. So, a larger value of C should correspond to a more densely packed and highly ordered material.

At photon energies near and below the Tauc gap, absorption is dominated by band tail to band tail transitions. This absorption has been found by experiment to vary as

$$\alpha(E) = \alpha_0 \exp\left[-\frac{1}{E_0} (E - E_e)\right] \quad (26)$$

where α_0 , E_0 , and E_e are material dependent constants and E_e is approximately equal to E_{gap} . This absorption is reminiscent of the exponential edge first observed by Urbach in alkali halides and is known as the "Urbach Edge." The energy E_0 is called the Urbach coefficient.

The tail state density, at least qualitatively, can be determined from the value of E_0 . Large E_0 implies a high density of tail states. Yet tail states arise from local disorder, so a large E_0 should imply large local disorder. To find E_0 , the absorption coefficient must be measured to small values ($< 5000 \text{ cm}^{-1}$). To measure these small values of α using the Cary Model 14A spectrophotometer required sample thicknesses such that $\alpha d \sim 1$ so that the optical density would be appreciable. This required sample thicknesses $> 4 \text{ }\mu\text{m}$.

C. Infrared Measurements

Infrared measurements were made on samples deposited on single crystal silicon substrates using a single beam Fourier Transform

Infrared (FTIR) spectrometer IBM model IR98. This spectrometer uses a silicon carbide glowbar as the source of the mid-infrared (4000 cm^{-1} to 400 cm^{-1}) radiation. The absorbance spectrum of a blank substrate was subtracted from the absorbance spectrum of the substrate-film sample to give the absorbance spectrum of the film alone. Both the blank substrate and the film carrying substrate were portions of the same silicon wafer. The spectrometer then yielded a plot of absorbance vs. wave number for the film. Absorbance is defined as

$$\text{Abs} = \log_{10} \left(\frac{I_0}{I} \right) \quad (27)$$

where I_0 is the intensity of the infrared radiation incident on the film and I is the intensity of the infrared radiation transmitted through the film.

Infrared absorbance and optical density have the same functional form; in principle, the absorption coefficient for the infrared region could be determined in the same way as the absorption coefficient was determined in the optical wavelength region. However, absorption in the film at infrared frequencies was so small that it allowed for large interference fringes which could not be easily handled by the formalism derived in the preceding section.

The absorption coefficient in the infrared region was determined by noting that Eq. (9) for the transmission through the film can be written as

$$T = C(\nu)\exp(-\alpha d) \quad (28)$$

where $C(\nu)$ is a frequency dependent function which is very nearly sinusoidal. Using Eq. (27), this can be written as

$$\text{Abs} = -\log_{10} T = \frac{1}{2.303} [\alpha d - \ln C(\nu)] \quad , \quad (29)$$

and $\ln C(\nu)/2.303$ can be treated as a frequency dependent baseline to be subtracted from the absorbance data. Figure 10 shows typical raw absorbance data with the baseline drawn in, while Fig. 11 shows the same data after the baseline has been subtracted. The absorption coefficient can then be found using

$$\text{Abs}^* \equiv \text{Abs} + \frac{C(\nu)}{2.303} = \frac{\alpha d}{2.303} \quad (30)$$

or

$$\alpha = \frac{2.303 \text{ Abs}^*}{d} \quad . \quad (31)$$

The hydrogen concentration of an a-Si:H film can be determined from its infrared spectrum. Brodsky, Cardona, and Cuomo²⁹ have identified three vibrational modes for hydrogen in a-Si:H. They identified these modes by comparing the infrared spectra of a-Si:H with that of silane, disilane, higher silanes, and halogen silanes. The three modes identified were the 1) stretching ($\sim 2000 \text{ cm}^{-1}$), 2) bending ($\sim 900 \text{ cm}^{-1}$), and 3) wagging ($\sim 640 \text{ cm}^{-1}$) modes. These vibrational modes are depicted in Fig. 12. According to Brodsky et al., there are three bond stretching modes near 2000 cm^{-1} . The stretching mode at 2000 cm^{-1} is believed to result from a silicon atom bonded to one hydrogen atom and

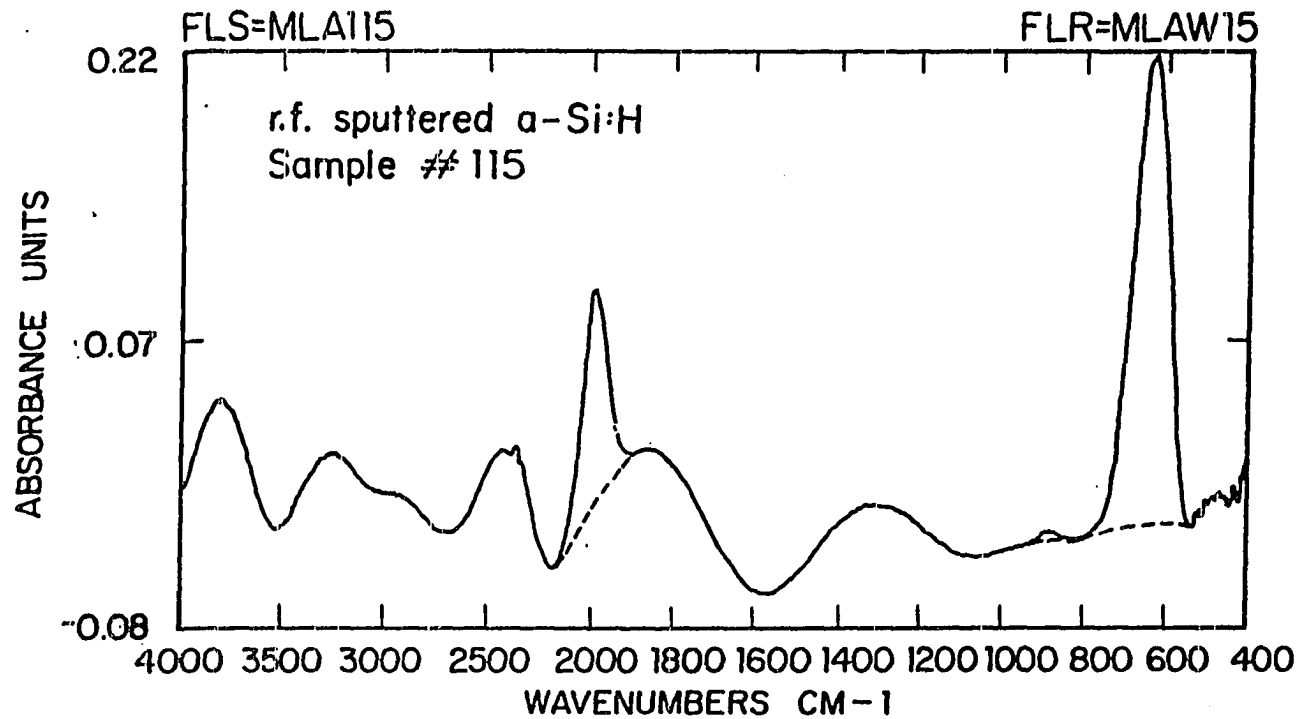


Fig. 10. A a-Si:H infrared spectrum. The dashed line is the assumed approximate baseline

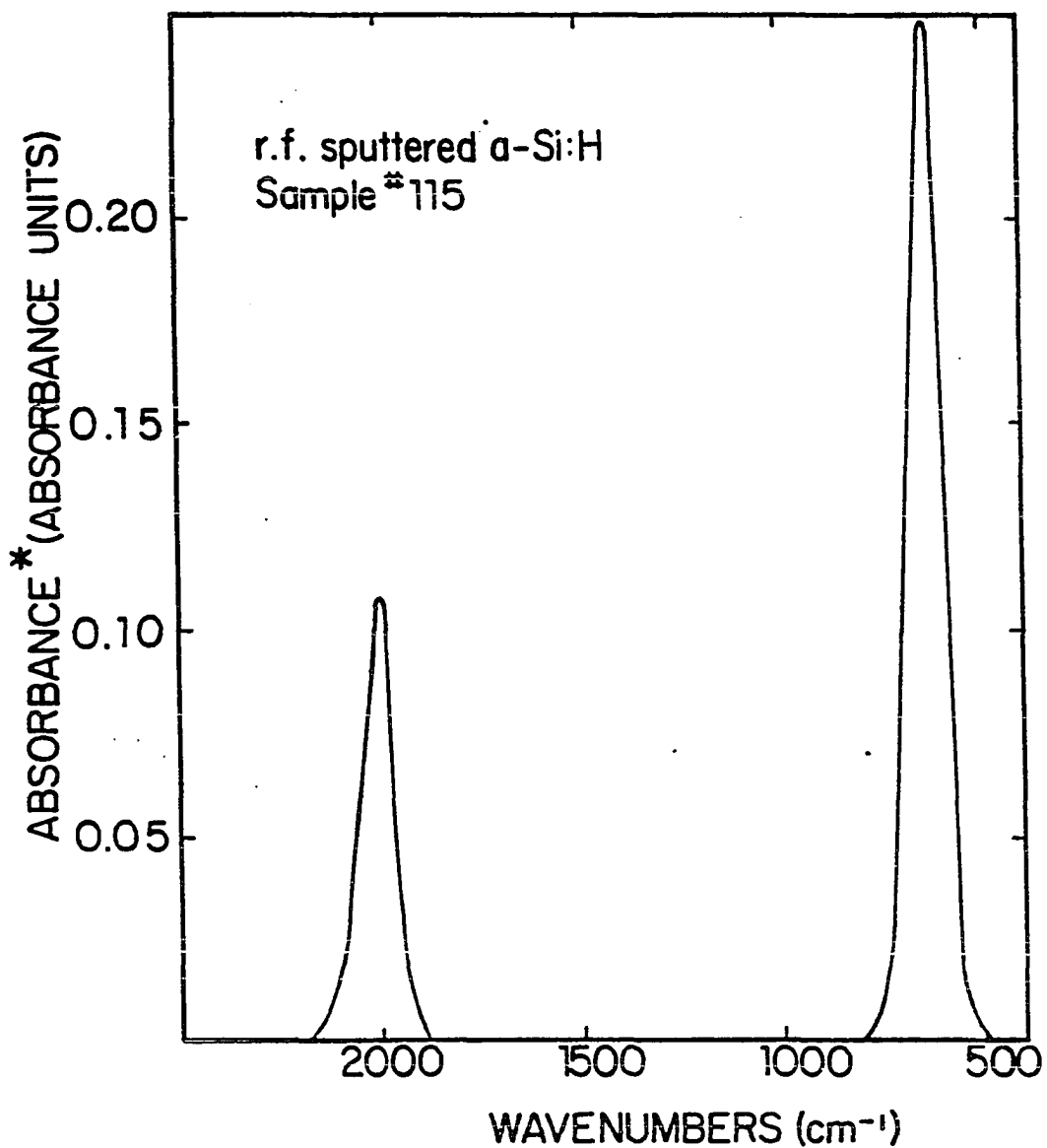


Fig. 11. Abs (defined in the text) vs. wave number for sample number 115. Note that this sample does not have either the 2100 cm^{-1} stretching band or the $850\text{--}890\text{ cm}^{-1}$ bending mode

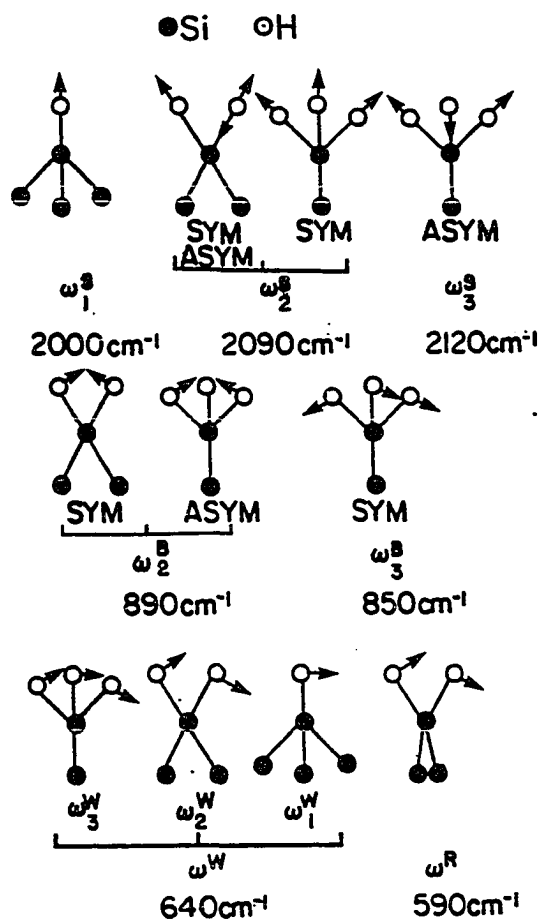


Fig. 12. Schematic illustration of the bond-stretching (top row), bond-bending (middle row), and bond wagging and rocking (bottom row) modes of SiH, SiH₂, and SiH₃ groupings in either hydrogenated a-Si or gaseous silanes. The frequencies in cm⁻¹ are those seen in hydrogenated a-Si. The solid circles represent Si atoms, the open circles represent H atoms. Only the relevant bonds to one central Si are shown, the other Si bonds can be connected to either Si or H atoms. Ref. 29

three silicon atoms. The stretching modes near 2100 cm^{-1} are believed to result from the vibrations of a silicon bonded to more than one hydrogen atom. This interpretation of the 2100 cm^{-1} stretching modes has been disputed by Shanks, Jeffrey, and Lowry.³⁰ They interpreted the 2100 cm^{-1} stretching mode as being due, in part, to clusters of silicon atoms each bonded to only one hydrogen atom. The bond bending modes at 890 cm^{-1} and 850 cm^{-1} have generally been accepted as resulting from the vibrations of bonds consisting of a silicon atom bonded to more than one hydrogen atom. However, it has been impossible to distinguish the cases of a silicon atom bonded to two or three hydrogen atoms. Still, the concentration of silicon atoms bonded to more than one hydrogen atom can be determined from the $850\text{--}890\text{ cm}^{-1}$ bond bending mode, albeit not very precisely. The 640 cm^{-1} bond wagging mode, which shows no discernible structure, is believed to result from silicon bonded to hydrogen in any configuration. Thus, the total concentration of hydrogen in a-Si:H can be determined from the 640 cm^{-1} bond wagging mode. It should also be noted that oxygen contamination of a-Si:H can give two more infrared absorption modes. An absorption mode at $\sim 900\text{ cm}^{-1}$ has been seen by Lucovsky, Nemanick, and Knights³¹ which is associated with oxygen incorporated into the bulk of the a-Si:H film. In this laboratory and others an absorption mode at $\sim 1100\text{ cm}^{-1}$ has been seen and associated with oxygen bonded to internal surfaces. This identification was made because this absorption mode was seen only in samples which exhibited a columnar morphology. In addition, the absorption peak grew with exposure to air.

The density of bonded hydrogen atoms in the a-Si:H films was determined from the integrated intensity of the 640 cm^{-1} bond wagging mode discussed above. The density of silicon atoms bonded to more than one hydrogen was found from the integrated intensity of the 850–890 cm^{-1} bond bending mode. These densities are given by

$$N = A^* \int \frac{\alpha}{\omega} d\omega \quad (32)$$

where the proportionality constant A^* for each mode is an experimentally determined parameter, α is the absorption coefficient, ω is the angular frequency, and the integral is carried out over the absorption peak of interest. The prefactors, A^* , for the various vibrational modes were determined by Shanks et al.³² who compared the integrated intensities of the various peaks to the total hydrogen concentration determined by nuclear reaction analysis. Their values of A^* are listed in Table 1.

It should be noted that Shanks et al.³² found the value of A^* for the 640 cm^{-1} wagging mode to be almost independent of preparation conditions and total hydrogen concentration. However, the value of A^* for the bending and stretching modes were found to vary with preparation conditions and hydrogen concentration. Therefore, the concentration of silicon atoms bonded to more than one hydrogen atom as found from the integrated intensity of the 850–890 cm^{-1} bond bending band must be viewed with caution.

The variation of A^* with preparation conditions and hydrogen concentration, as well as the source of Eq. (32), can be understood by considering two atoms bound by a Hooke's Law type of force. If these atoms, assumed to have a reduced mass of μ and effective charge e^* , are

Table 1. The proportionality constant, A^* , between the integrated infrared absorption and the hydrogen concentration

Wave number	640	840-890	2000	~ 2100	2100 (cm^{-1})
Mode	Wag	Bend	Stretch	Stretch	Stretch
Bonding	Si-H Si-H ₂	Si-H ₂	Si-H (Isolated)	Si-H (Cluster)	Si-H ₂
A^*	1.6×10^{19}	2×10^{20}	2.2×10^{19}	1.7×10^{20}	9.1×10^{19} (cm^{-2})

placed in an alternating electric field $E = E_0 e^{-i\omega t}$, then the equation of motion for this system will be

$$\mu \frac{d^2 x}{dt^2} + \frac{\mu}{\tau} \frac{dx}{dt} + \mu \omega_0^2 x = e^* E_0 e^{-i\omega t} \quad (33)$$

In Eq. (33) the term containing τ is the damping term and ω_0 is the natural vibrational frequency. The steady state solution of Eq. (33) is

$$x(t) = \frac{e^* E_0 e^{-i\omega t}}{\mu (\omega_0^2 - \omega^2 - i\omega/\tau)} \quad (34)$$

If $N(\omega)$ is taken as the number of oscillators vibrating at ω per unit volume, then the dipole moment can be written as

$$P = N(\omega) e^* x = \left(\frac{\epsilon}{\epsilon_0} - 1 \right) \epsilon_0 E \quad (35)$$

where ϵ is the dielectric constant. By substituting Eq. (34) into Eq. (35) and solving for the imaginary part of the dielectric constant; it is found that

$$\text{Im}(\epsilon) \equiv \epsilon_2 = \frac{N(\omega) e^{*2}}{\mu} \frac{\omega/\tau}{(\omega_0^2 - \omega^2)^2 + \omega^2/\tau^2} \quad (36)$$

In the region of the absorption peak, $\omega \approx \omega_0$ and Eq. (36) can be approximated by

$$\epsilon_2 = \frac{N(\omega) e^{*2} \tau}{\mu \omega_0} \quad (37)$$

With $\epsilon_2 = \text{anc}/\omega$ this becomes

$$N(\omega) = \frac{cn\omega_0}{\tau} \frac{\mu}{e^{*2}} \frac{\alpha(\omega)}{\omega} . \quad (38)$$

Both $N(\omega)$ and $\alpha(\omega)$ have been written explicitly as functions of ω . The density of oscillators, N , with a natural vibrational frequency ω_0 is given by integrating $N(\omega)$ over the peak of interest. This yields

$$N = A^* \int \frac{\alpha}{\omega} d\omega \quad (39)$$

with

$$A^* = \frac{cn\omega_0}{\tau} \frac{\mu}{e^{*2}} . \quad (40)$$

Thus, the value of A^* can be changed by changing the reduced mass, μ , or the effective charge, e^* . The reduced mass and charge have been seen to vary with the environment of the oscillator.³³ And, in a-Si:H, the environment of the oscillator or local structure of the material is known to be strongly effected by preparation conditions and total hydrogen concentration.^{29,32} Thus, it is expected that A^* may vary with sputtering conditions. In particular, the value of A^* may depend on the inert gas used for sputtering. Shanks et al.³² have treated this problem in terms of a variation in local field due to changes in the shapes of cavities in which the oscillators may be found. They write the local field, E_L , in terms of the applied field, E_{ext} , as

$$E_L = fE_{ext} . \quad (41)$$

The local field factor f was calculated for each of the vibrational modes assuming the oscillator was in a spherical cavity and assuming it was in a pillbox-shaped cavity. For the 640 cm^{-1} wagging mode, the field factor f was found to vary from 1 to 1.5 depending on the shape of

the cavity. This small variation in f , and a related small variation in A^* , makes the 640 cm^{-1} wagging mode an accurate measure of the total hydrogen concentration. For the $850\text{--}890\text{ cm}^{-1}$ bending mode, f was found to vary from 1.5 to $\epsilon \sin(\beta/2)$, where ϵ is the dielectric constant of silicon and β is the angle between two hydrogen atoms bonded to the same silicon atom. This would allow for a factor of four change in A^* for the $850\text{--}890\text{ cm}^{-1}$ bending mode. However, since in practice the variation of A^* for the wagging mode is much less than the 50 percent predicted by this treatment, it seems reasonable to assume that A^* for the bending mode varies by much less than a factor of four.

D. ESR Measurements

Electron spin resonance (ESR) measurements were used to measure the density of unpaired dangling bonds in the a-Si:H films. A Brüker 220 D SR spectrometer was used with a Nicolet signal averager to make these measurements. The samples used were deposited on Corning 7059 glass substrates which had a surface area of one-half inch by four millimeters. Two references were used. One reference was a sample of Picein 80³⁴ known to contain 3.43×10^{15} spins. This reference was used in determining the number of spins in the a-Si:H films. The determination of the number of spins will be discussed later. The second reference was a small quantity of DPPH used to determine the g-factor of the a-Si:H films. The g-factor and its determination will also be discussed later.

The electron spin resonance measurement is performed by placing the sample in a microwave cavity which is in a large external magnetic

field. The frequency of the microwave field is held constant while the external magnetic field is swept from H_{Low} to H_{High} . In the experiments reported upon here, H_{Low} was usually 3350 Gauss and H_{High} was 3410 Gauss. The microwave field was ~ 0.015 Gauss and had a frequency of ~ 9.5 GHz. As the external field was swept from its low to high values, it passed through the field for resonance given by

$$H_0 = \frac{\hbar \omega_0}{\beta g}; \quad (42)$$

where \hbar is Planck's constant, ω_0 is the angular frequency of the microwave field, β is the Bohr magneton, and g is the spectroscopic splitting factor. When this resonance condition is met, unpaired electrons in the sample absorb energy from the microwave field. To understand why this is so, consider the energy of interaction between the electronic spin and the magnetic field

$$E = -\vec{\mu} \cdot \vec{H}_0 \quad (43)$$

where $\vec{\mu}$ is the magnetic moment of the electron given by

$$\vec{\mu} = -g \frac{|e|\hbar}{2mc} \vec{S} \quad (44)$$

where g is the spectroscopic splitting factor and \vec{S} is the spin of the electron, $\pm 1/2$. Equation (44) can be simplified somewhat by introducing the Bohr magneton

$$\beta = \frac{|e|\hbar}{2mc} \quad (45)$$

which gives

$$\vec{\mu} = -g\beta\vec{S} \quad (46)$$

Through this interaction, the large constant magnetic field produces a splitting in energy levels between the spin down and spin up states of

$$\Delta E = E_{\text{up}} - E_{\text{down}} = g\beta H_0 \quad (47)$$

When the oscillating (microwave) field has an angular frequency ω_0 such that

$$\Delta E = \hbar\omega_0, \quad (48)$$

the microwave field can induce transitions between the two energy levels. By comparing Eqs. (47) and (48), it is seen that these transitions occur when

$$g\beta H_0 = \hbar\omega_0 \quad (49)$$

This is the resonance condition of Eq. (42). The ratio of populations of the spin up, N_+ , and spin down, N_- , states is given by

$$\frac{N_+}{N_-} = e^{-\Delta E/kT} \quad (50)$$

where ΔE is given by Eq. (48), k is the Boltzmann constant and T is the temperature of the spin system. Assuming room temperature and $\omega_0 = 9.5$ GHz, this gives

$$\frac{N_+}{N_-} \approx 0.998 \quad (51)$$

Thus, there are slightly more electrons in the spin down levels than the spin up levels. Therefore, assuming the probability of transitions from spin up to spin down are equal, more spin down to spin up transitions occur than spin up to spin down transitions. This gives a net

absorption of energy by the electron spin system from the microwave field. Given enough time, the populations of the spin up and spin down levels would become equal. This would imply an infinite temperature for the spin system according to Eq. (50). This does not happen for the small microwave fields used in these experiments. The electrons exchange energy with other electrons and the "lattice" in an attempt to keep the ratio of spin populations at its room temperature value.

The discussion of electron spin resonance given above would seem to indicate that the absorption of microwave energy by the electrons should occur at only one value of the applied external field. It also implies that once the transitions induced by the microwave field have been made, the electronic populations of the spin up and spin down states will remain at their new values. In practice, neither of these two implications is found to be true. Absorption is found to occur over a range of applied external fields. And the ratio of spin up to spin down populations is seen to return to its room temperature value. These observations can be understood in terms of the phenomenological relaxation formalism of Bloch.³⁵ This formalism introduced relaxation times to explain the transfer of energy amongst the electrons and to the surrounding "lattice," i.e., other degrees of freedom. This treatment yields the following expression for the absorbed microwave power A³⁶

$$A = X_0 \omega_0^2 T_2 \frac{H_1^2}{1 + T_2^2 (\omega_0 - \omega)^2 + \frac{\beta^2}{h^2} H_1^2 T_1 T_2} \quad (52)$$

where ω_0 is the microwave angular frequency, T_1 is the spin-lattice relaxation time, T_2 is the spin-spin relaxation time, H_1 is the amplitude of the microwave field, and χ_0 is the Curie static susceptibility. The Curie static susceptibility is given by

$$\chi_0 = Ng^2\beta^2S(S+1)/3kT \quad (53)$$

where N is the number of paramagnetic species per unit volume and all other terms have been defined earlier. For small values of H_1 , Eq. (52) reduces to

$$A = \frac{\chi_0 \omega_0^2 T_2 H_1^2}{1 + T_2^2 (\omega_0 - \omega)^2} \quad (54)$$

Absorption plotted as a function of slowly varying $\omega_0 = (\beta/h)H_0$ defines a resonance curve with a maximum at $\omega_0 = \omega$ having a half-width at half-maximum of

$$\Delta\omega_{1/2} = \frac{1}{T_2} = \frac{\beta}{h} \Delta H_{1/2} \quad (55)$$

Thus $(h/\beta)T_2 = \Delta H_{1/2}$ is the half-width expressed in units of the external field. This explains the finite width of the absorption spectrum and the spins "relaxing" back to their room temperature populations.

As the sweep of the external magnetic field is carried out, a detector measures the change in absorbed microwave energy, ΔP_a , divided by the microwave energy incident on the sample, P_w . With the energy absorbed by the sample given by Eq. (54) and the microwave energy incident on the sample by

$$P_w = H_1^2, \quad (56)$$

the ratio $\Delta P_a/P_w$ is seen to be proportional to χ_0 . Yet, χ_0 is proportional to the number of paramagnetic species in the sample. Thus, the area under the ESR absorption spectrum should be proportional to the number of paramagnetic species in the sample.

The Brüker 220D SR uses a phase sensitive lock-in detection technique. This technique involves modulating the external magnetic field with a small sinusoidal field, $H_{\text{mod}} \sin \omega_{\text{mod}} t$. The detector measures those changes in absorption that occur with a frequency of ω_{mod} . If the amplitude of this modulation is smaller than the width of the magnetic resonance absorption peak, a simple Taylor series expansion shows that this component will be proportional to the derivative of the absorption spectrum. Thus, the measurements performed yield a spectrum proportional to dN/dH vs H , where N is the number of unpaired spins per unit field in the sample and H is the external magnetic field.

The number of spins was determined from this spectrum, after Poole,³⁷ by comparing the spectrum to that of a reference sample with a known number of spins. The number of spins in the sample was given by

$$N^S = N^r \frac{(\Delta H_{pp}^S)^2}{(\Delta H_{pp}^r)} \frac{(Y_m'^S)}{(Y_m'^r)} \frac{(H_{\text{mod}}^r)}{(H_{\text{mod}}^S)} \frac{(P_w^r)^{1/2}}{(P_w^S)} \\ \times \frac{(\Lambda^{1S})}{(\Lambda^{1r})} \frac{(G^r)}{(G^S)} \frac{(NP^r)}{(NP^S)}. \quad (57)$$

In this equation, ΔH_{pp} is the field separation between the positive first derivative peak and the negative first derivative peak, Y_m' is the

amplitude of the absorption derivative peak, P_w is the amplitude of the absorption derivative peak, P_w is the microwave power, Λ' is a lineshape factor, G is the lock-in gain used, and NP is the number of scans used to signal average by the Nicolet. The lineshape factor Λ' is equal to 1.03 for Gaussian lines and 3.63 for Lorentzian lines. For lines whose shapes were mixed Lorentzian and Gaussian, an interpolated value of Λ' was used. The term $\Delta H_{pp}^2 Y_m'$ is proportional to the value of the first derivative spectrum integrated twice and so proportional to the area under the absorbance curve. the rest of the terms account for differences in measurement parameters between the measurement of the sample and reference. The value of the g -factor was found by using Eq. (42) and comparing the position of sample's absorption peak to that of a DPPH reference sample. The g -factor of DPPH is known to be 2.0036 ± 0.0003 .

Electron spin resonance was one of the earliest probes used to study a-Si.^{38,39} In sputtered samples a single asymmetric absorption was found at a g -factor of 2.0055 with a spin density in the range of 10^{19} - 10^{29} cm^{-3} .³⁹ The same g -factor is found in a-Si regardless of preparation method and is therefore assumed intrinsic to the material.⁴⁰ By comparing the line width and g -value of the a-Si ESR absorption to that of the dangling bond in radiation damaged c-Si^{41,42} and the dangling bond on the surfaces of Si/SiO₂ interfaces,⁴³ the ESR signal of a-Si at a g -factor of 2.0055 has been clearly identified as belonging to dangling bonds. Also, the reduction of the $g = 2.0055$ ESR signal with hydrogen incorporation has been seen.⁴⁴⁻⁴⁶ This is believed to be due to hydrogen bonding to dangling bonds and thereby "passivating" their ESR signal.

IV. RESULTS OF He, Ar, AND Xe SPUTTERING

A. Introductory Comments

Three series of r.f. sputtered a-si:H thin films were prepared. The inert gas used for the sputtering was different for each of these series. The inert gases used were He, Ar, and Xe. A set of samples was prepared for each gas by using r.f. sputtering powers ranging from 50W ($0.27\text{W}/\text{cm}^2$) to 600W ($3.3\text{W}/\text{cm}^2$). The films were then characterized using infrared, optical and electron spin resonance (ESR) measurements.

Sample preparation conditions and the results of thickness, infrared, optical and ESR measurements are recorded in Table 2. Sample preparation conditions include sputtering gas (He, Ar, or Xe), partial pressures of the sputtering gas and hydrogen, and transmitted r.f. sputtering power. Measurement results include thickness, deposition rate, total hydrogen concentration, the concentration of silicon atoms bonded to more than one hydrogen atom, optical energy gap, the slope of $\sqrt{E_{\text{on}}}$ vs. E, the Urbach edge coefficient, and the unpaired dangling bond spin density. Figure 13 gives a typical infrared spectrum, Fig. 14 is a typical optical density vs. wavelength measurement, and Fig. 15 is a typical ESR first derivative absorption spectrum.

B. Deposition Rates

Figure 16 shows the measured deposition rate vs. sputtering power for the three sets of samples sputtered in He/H₂, Ar/H₂ and Xe/H₂ atmospheres. The deposition rate was calculated by dividing the thickness measured by the Dektak stylus profilometer by the sputtering

Table 2. Results of thickness infrared, optical density, and ESR measurements on the three series of samples discussed in the text

Samp. No.	r.f. power (W)	Thick. (μm)	Dep. Rate (Å/S)	[H _T] (a/o %)	[Si-H ₂] (a/o %)	Dangling bond density (cm ⁻³)	E _{gap} (ev)	$\sqrt{E\alpha n}$ (E-E _g) ^{-1/2} (eVcm) ^{-1/2}	Urbach edge coeff. (eV)
Helium Sputtered Samples									
108	50	0.33	0.09	31.9	53.7	2.9×10 ¹⁸	2.14	2400	
126	100	0.45	0.26	17.5	21.3	1.5×10 ¹⁸	2.07	1190	
131	150	1.05	0.36	8.1	8.2	5.4×10 ^{17a}	1.97	950	
127	200	1.08	0.48	8.4	6.5	7.5×10 ^{17a}	1.87	870	
132	250	0.93	0.47	11.3	6.2	1.3×10 ¹⁸	1.50	760	
128	300	0.93	0.61	10.5	3.5	1.4×10 ¹⁸	1.64	860	
133	400	0.96	0.84	9.2	2.7	4.0×10 ^{18a}	1.26	780	
130	500	1.30	1.39	5.7	1.0	9.3×10 ^{17a}	1.50	670	
117	600	0.90	1.18	7.2	1.0	4.6×10 ^{17a}	1.59	960	
153	600	4.10	1.46	4.1	5.8		1.41		0.19
154	300	5.50	0.65	5.0	3.8		1.39		0.49
Argon Sputtered Samples									
111	50	1.65	1.11	20.7	11.3	1.3×10 ¹⁸	1.95	1220	
122	100	1.22	1.36	23.4	14.0	2.4×10 ¹⁸	1.95	1470	
123	150	1.11	1.49	23.8	14.1	2.5×10 ¹⁸	1.96	1860	
113	200	1.43	1.59	20.3	11.8	7.9×10 ¹⁷	1.86	1810	
124	250	1.23	2.36	18.5	7.1	1.6×10 ¹⁷	1.86	1880	
114	300	1.27	2.23	17.7	5.2	8.9×10 ¹⁶	1.74	1920	
125	350	1.17	3.25	15.4	3.6	1.1×10 ¹⁷	1.76	1770	
115	400	2.73	3.58	11.3	1.7	1.8×10 ¹⁷	1.58		
116	500	2.45	3.71	8.9	0.0		1.57	1370	
121	600	0.84	4.00	12.5	0.0	2.3×10 ¹⁷	1.67	2070	
144	600	9.35	5.39	7.6	2.5		1.55		0.09
163	100	5.6	1.57	23.3	14.7		1.96		0.08

^aSamples which suffered post depositional oxidation.

Table 2. (continued)

Samp. No.	r.f. power (W)	Thick. (μm)	Dep. Rate (Å/S)	[H _T] (a/o %)	[Si-H ₂] (a/o %)	Dangling bond density (cm ⁻³)	E _{gap} (ev)	$\sqrt{E\alpha n}$ (E-E _g) ^{-1/2} (eVcm) ^{-1/2}	Urbach edge coeff. (eV)
Xenon Sputtered Samples									
105	50	1.05	0.93	17.5	4.3	1.2×10 ¹⁸	1.70	970	
104	100	1.35	1.23	17.7	4.7	3.3×10 ¹⁸	1.66	1090	
103	200	1.10	2.00	13.4	2.1	3.3×10 ¹⁸	1.71	1980	
109	225	1.18	2.07	13.4	1.9		1.61	1570	
107	250	1.50	2.38	9.2	1.8	2.5×10 ¹⁸	1.63	1190	
102	300	1.10	3.06	9.9	1.3	2.4×10 ¹⁸	1.62	1210	
101	400	1.60	3.56	10.3	1.8	2.5×10 ¹⁸	1.55	1390	
100	500	1.38	3.83	6.3	0.51	1.3×10 ¹⁸	1.45	1370	
99	600	3.91	9.7	0.51		1.3×10 ¹⁸	1.48	1590	
149	60013.								
9	6.448.								
5	2.2		1.47		0.08				
150	300	9.00	3.57	10.3	2.8		1.54		0.10

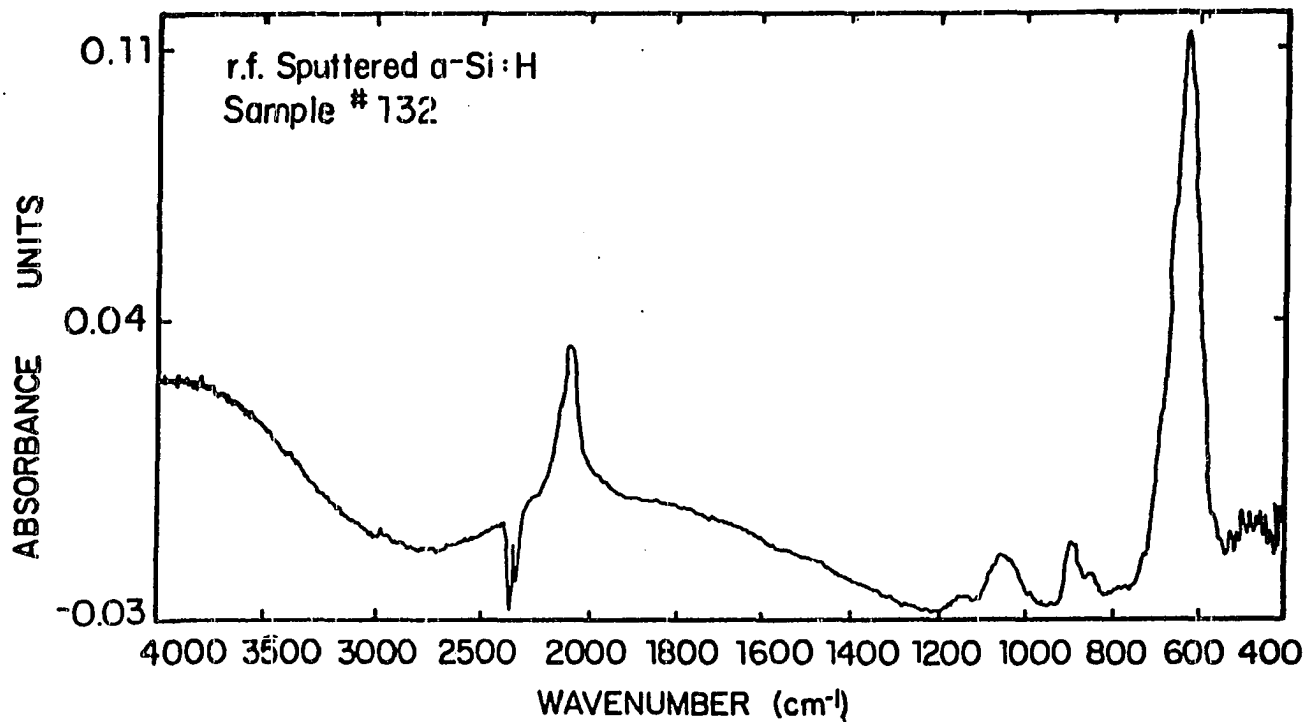


Fig. 13. An infrared absorption spectrum of sample #132. The peaks (from left to right) are the Si-H stretching band at $\sim 2100 \text{ cm}^{-1}$, the Si-O bending mode at $\sim 110 \text{ cm}^{-1}$, the Si-H bending band at $890\text{-}850 \text{ cm}^{-1}$, and the Si-H wagging mode at $\sim 640 \text{ cm}^{-1}$. Note the large interference fringes from 40000 cm^{-1} to 1200 cm^{-1} .

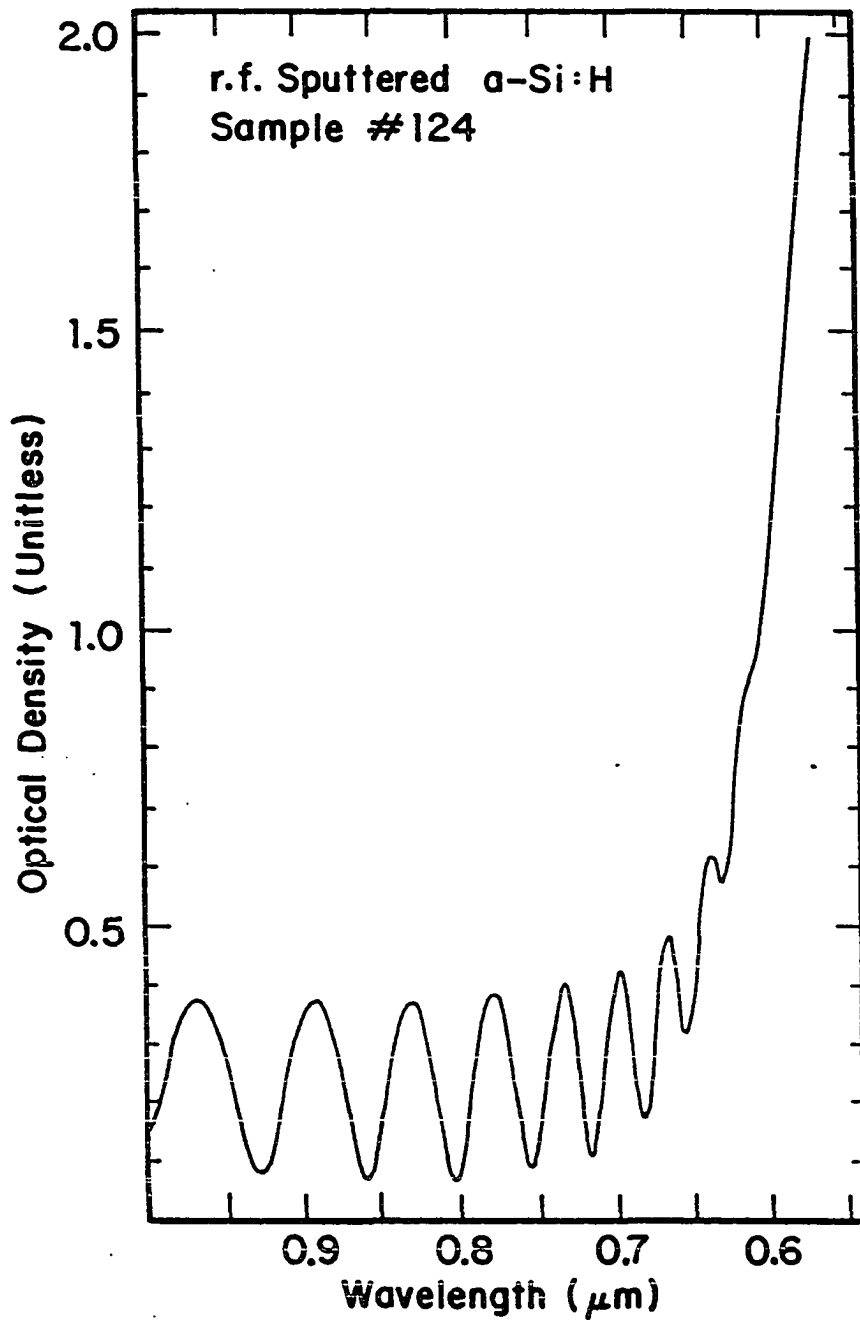


Fig. 14. Typical optical density vs. wavelength spectrum

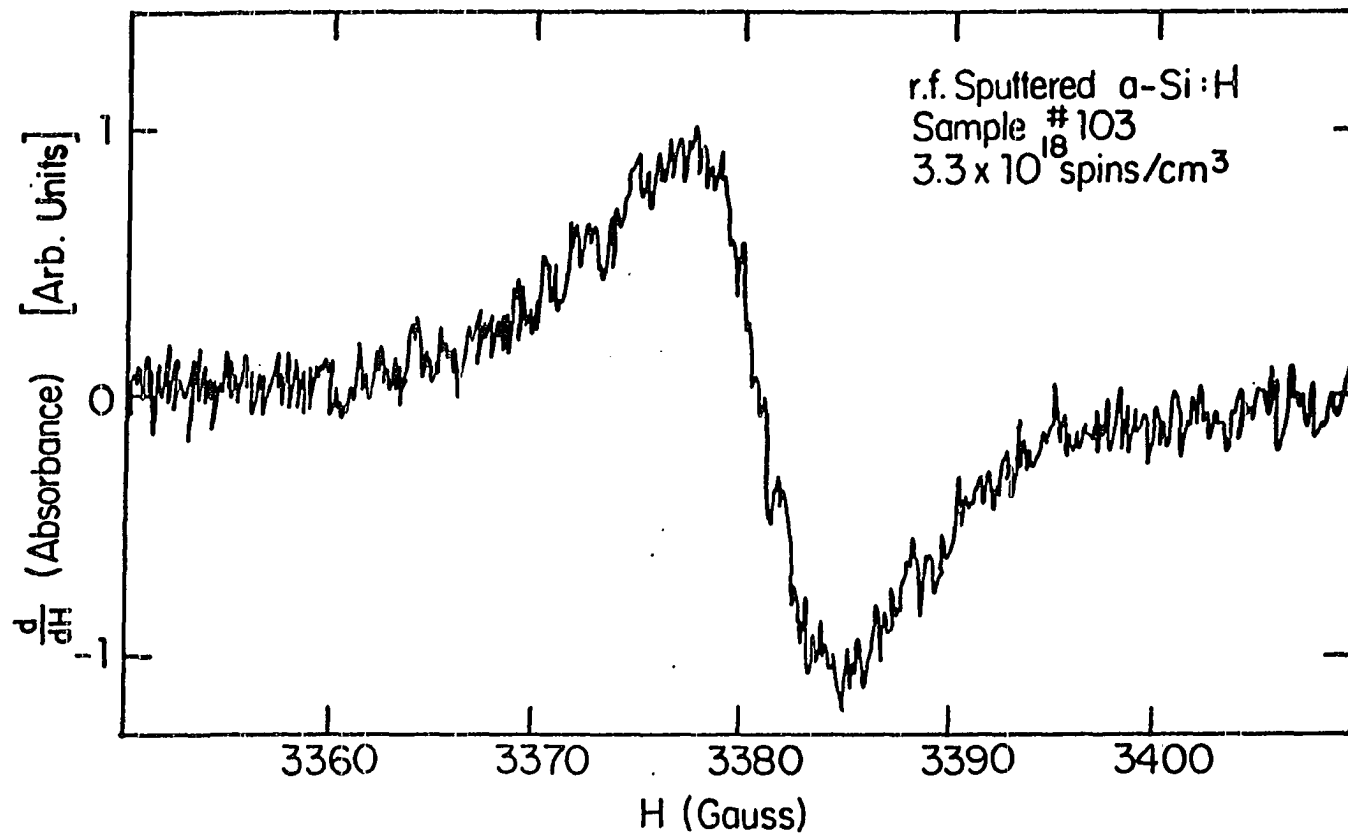


Fig. 15. A typical ESR first derivative absorption spectrum

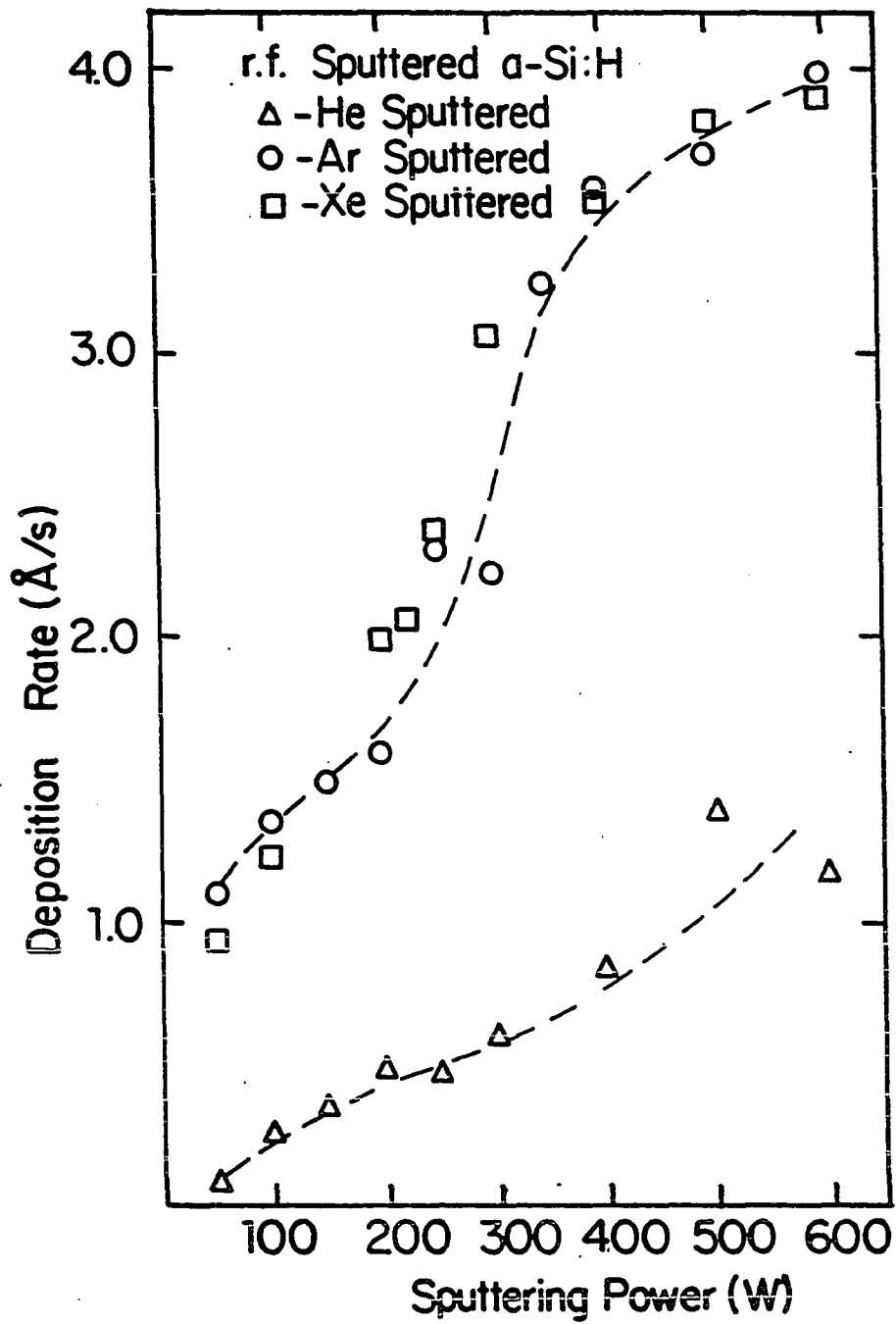


Fig. 16. Deposition rate vs. sputtering power for the r.f. sputtered a-Si:H samples

time. Repeated measurements on different portions of the same film showed the thickness measurements to be reproducible to within five percent. Sputtering time was typically measured to within a few seconds out of a few hours. Therefore, the deposition rates have an uncertainty of approximately five percent.

The deposition rates tend to increase with increasing sputtering power. At higher r.f. sputtering powers, the inert gas ions are accelerated through a larger potential and strike the target with higher energies and momenta. This leads to a larger momentum transfer between the ions and the target. This results in larger sputtering yields and larger deposition rates. The deposition rates for samples prepared in a He/H₂ atmosphere are much lower than those prepared in an Ar/H₂ or Xe/H₂ atmosphere.

The sputtering yield, defined as the number of silicon target atoms ejected per incident inert gas sputtering ion, is expected to depend on the inert gas used for sputtering. However, the sputtering yield is not a simple function of the inert gas ion's mass. The sputtering yield also depends on the ion's penetration depth and scattering cross section (i.e., in what direction it scatters Si atoms). Therefore, it is easiest and most instructive to compare the observed deposition rates to deposition rates predicted by experimentally determined sputtering yields. Sputtering yields were taken from the work of Anderson and Bay.⁴⁷ This work gave sputtering yields as a function of incident ion energy for He⁺, Ar⁺ and Xe⁺. In order to compare to the present work, it is necessary to estimate the energy with which the inert gas ions strike the target at a given sputtering power. In the r.f. sputtering

process, positively charged ions are formed in a "glow region" close to the substrates and then accelerated towards the target through the "dark space", see Fig. 17. If one neglects the small sheath voltage at the substrate, it is reasonable to assume that the ions experience an accelerating voltage nearly equal to the voltage between the target and pedestal of the sputtering system. This voltage was found to vary with sputtering power but was independent of sputtering gas. It was also assumed that each ion was singly ionized. These assumptions allowed the determination of ion incident energy as a function of r.f. sputtering power. Multiplying the sputtering yield by the measured sputtering ion density gives the number of silicon atoms ejected from the target per unit area. Dividing this quantity by the density of a-Si:H gives the expected deposition rate based on the sputtering yield. The generally accepted density of a-Si:H is 5.12×10^{22} atoms/cm³. Thus, an expected deposition rate as determined from the sputtering yield can be found using

$$\text{Deposition Rate} = (\text{Sputtering Yield}) \frac{(\text{Sputtering ion density})}{(5.12 \times 10^{22} \text{ cm}^{-3})} \quad (58)$$

Here it has been assumed that all of the silicon atoms that leave the target deposit on an area of the pedestal equal to that of the target.

As can be seen in Fig. 18, the predicted deposition rates are generally higher than the observed deposition rates. However, the relationship between predicted and observed deposition rates does seem to be nearly linear, indicating that the sputtering yield is the dominant factor in determining the deposition rate. Another factor

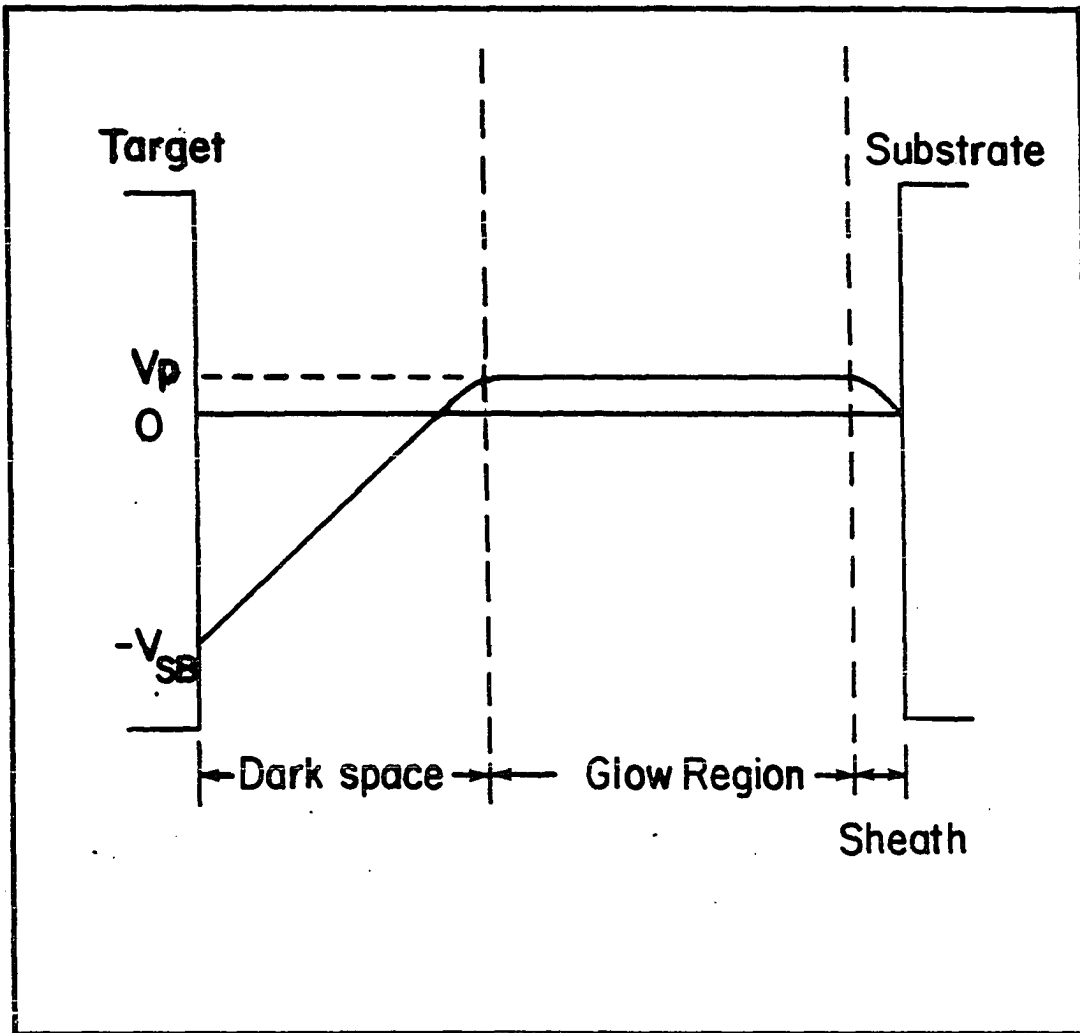


Fig. 17. Schematic description of the voltage distribution in a r.f. sputtering process. V_p is the sheath voltage between the plasma and substrate; and, V_{SB} is the naturally occurring self-bias which is responsible for the sputtering of the target

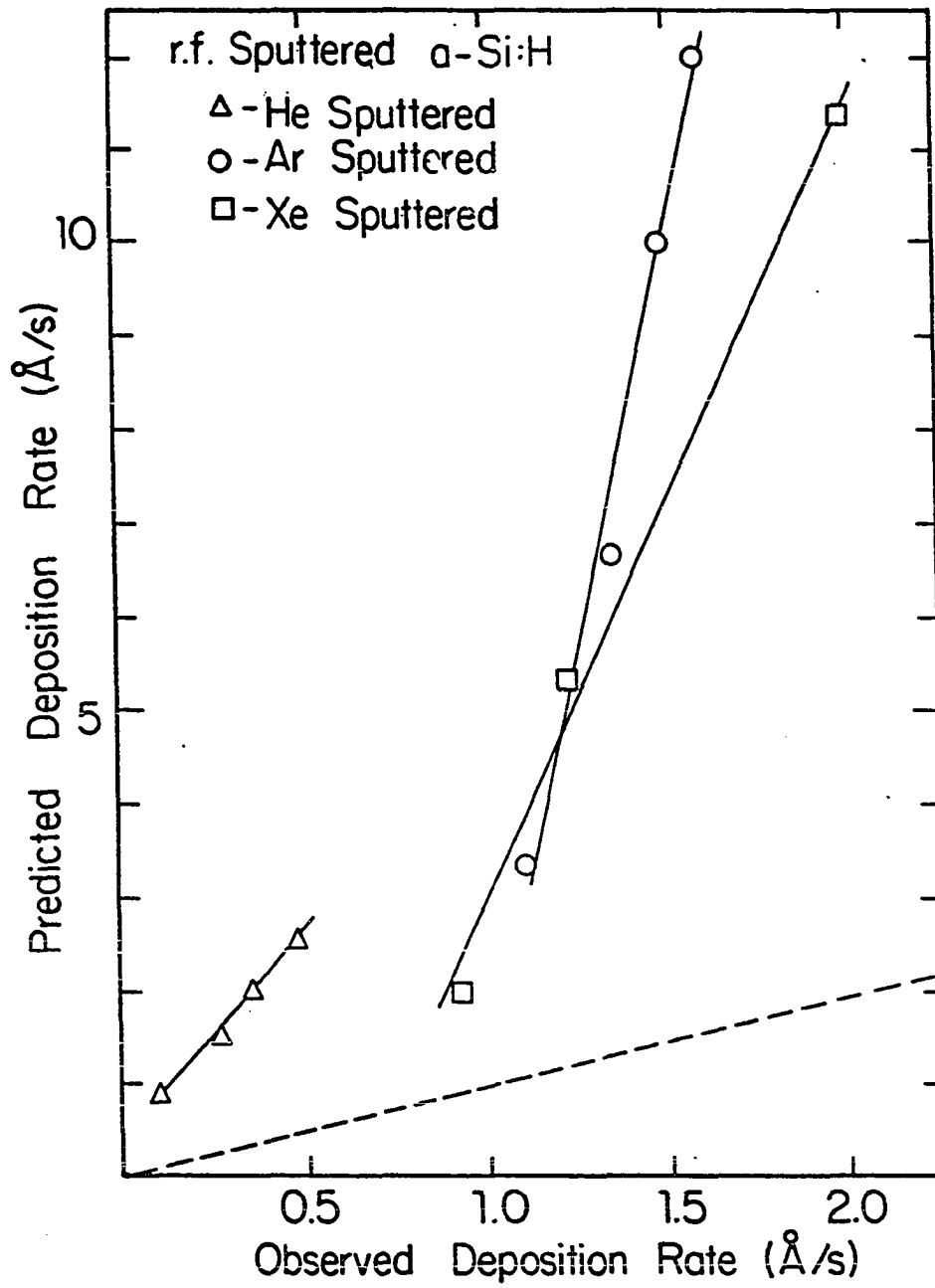


Fig. 18. Predicted vs. observed deposition rates for a-Si:H prepared by r.f. sputtering

which might influence the deposition rate would be plasma-substrate interactions. Some of the positively charged inert gas ions may be accelerated towards the growing film by the sheath voltage, see Fig. 17. These ions may desorb and reorganize silicon atoms bonded on the top of the growing film surface. The desorption of silicon atoms would lower the deposition rate. It would be expected that helium ions, because of their low mass, would be the least effective in removing silicon atoms from the growing film surface. This expectation is confirmed by Fig. 18 which shows that the slope of the predicted deposition rate vs. observed deposition rate for He sputtered films is much lower than that for either Ar or Xe sputtered films. The sputtering yield of Xe^+ is slightly less than that of Ar^+ at low incident ion energies.⁴⁷ Thus, Ar ions are expected to be slightly more efficient than Xe ions at removing silicon atoms from the growing film surface. This also agrees with Fig. 18 in that the Xe sputtered samples give a slightly smaller slope than the Ar sputtered samples.

C. Hydrogen Concentrations

The hydrogen concentration of the samples was determined using infrared spectroscopy as discussed earlier. The total hydrogen concentration and the concentration of silicon atoms bonded to more than one hydrogen atom was found using

$$N = A^* \int \frac{\alpha}{\omega} d\omega \quad (59)$$

The 640 cm^{-1} bond wagging mode was used to determine the total hydrogen concentration, $[\text{H}_T]$. The prefactor for this mode, as discussed earlier, should not depend on the sputtering gas. The $850\text{--}890 \text{ cm}^{-1}$ bond bending

band was used to determine the concentration of silicon atoms bonded to more than one hydrogen atom, to be referred to as $[\text{Si-H}_2]$. The prefactor for this band may be a function of sputtering gas, and may vary by a factor of two. However, with a series of samples all sputtered with the same inert gas, this prefactor should be almost constant. Thus, the absolute values of $[\text{Si-H}_2]$ are in question while the relative values within a series of samples is much more certain. There were two possible sources of error in determining the hydrogen concentration. First, the thickness measurement of the sample was used to find the absorption coefficient, see Eq. (31). This introduced a five percent uncertainty into the determination of the hydrogen concentration. Second, the drawing of the baseline introduced an uncertainty of about five percent in the determination of $[\text{H}_T]$ and of about ten percent in the determination of $[\text{Si-H}_2]$. The larger uncertainty in $[\text{Si-H}_2]$ is due to the small size of the $850\text{--}890\text{ cm}^{-1}$ bond bending peaks. The values of $[\text{H}_T]$ and $[\text{Si-H}_2]$ given in Table 2 have been normalized by dividing by $5.12 \times 10^{22}\text{ cm}^{-3}$, the density of a-Si:H.

The total hydrogen concentration of the films, as is seen in Fig. 19, tends to decrease with increasing deposition rate for all three sets of samples. From Fig. 19 it can be seen that the films deposited in a He/H₂ atmosphere have the greatest range in hydrogen concentration (from 32% to 5.7%) over the shortest range in deposition rates (from 0.09 Å/s to 1.39 Å/s). The samples deposited with Ar/H₂ and Xe/H₂ atmospheres show qualitatively similar hydrogen concentration vs. deposition rate relationships, with the Xe/H₂ sputtered samples having slightly less hydrogen at a given deposition rate than the Ar/H₂ sputtered samples.

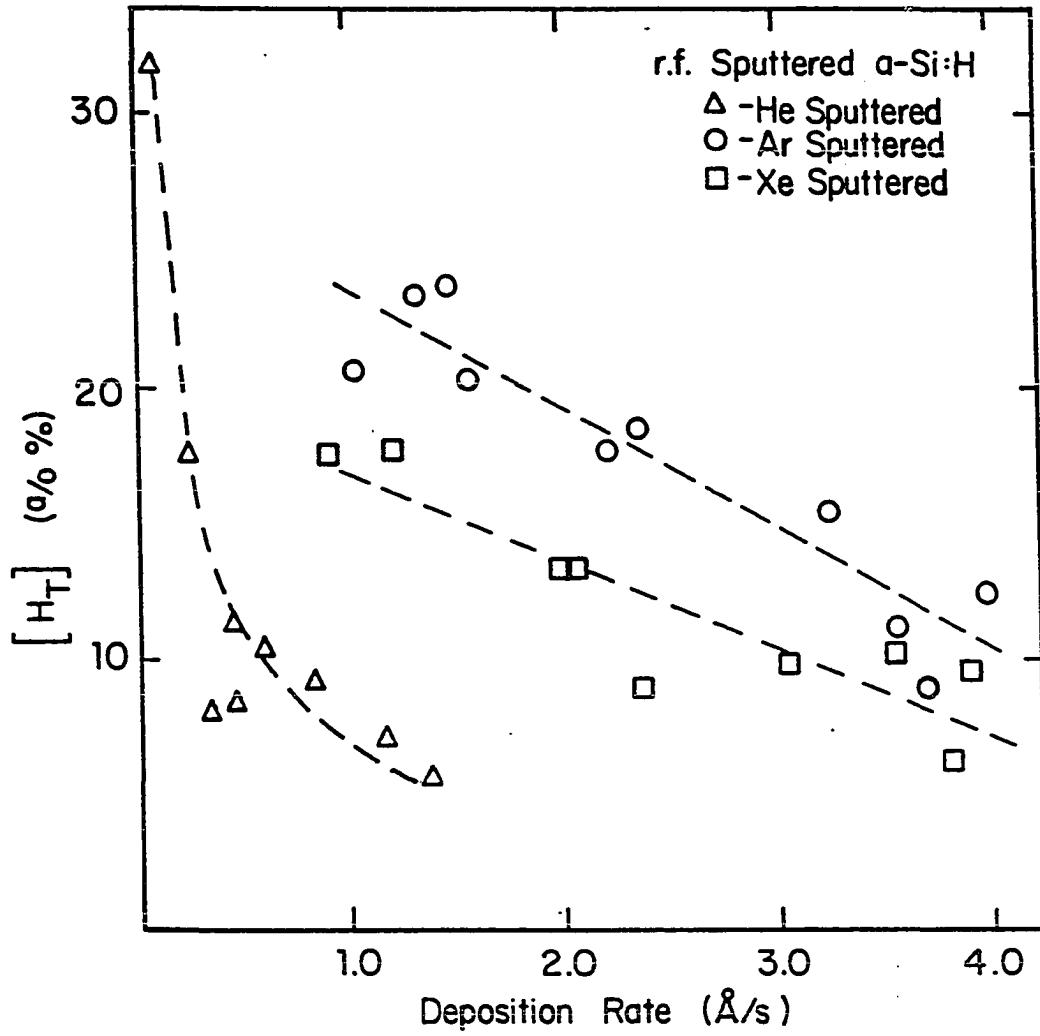


Fig. 19. Total hydrogen concentration vs. deposition rate for the three sets of r.f. sputtered a-Si:H films

A kinematic model for the incorporation of hydrogen into r.f. sputtered a-Si:H films has been proposed by Moustakas, Tiedje, and Lanford.⁴⁸ They show that if it is assumed that 1) there are no gas phase reactions between Si and H, 2) hydrogen incorporation arises from surface reactions only, and 3) there is no significant desorption of bonded H, then the hydrogen concentration in the film is given by this kinematic model as

$$[H_T] = [H_T]_{\max} \left[1 - \exp\left(-\frac{F\theta\sigma}{R}\right) \right] \quad (60)$$

In Eq. (60), $[H_T]_{\max}$ is the maximum possible hydrogen concentration, F is the flux of hydrogen onto the surface, R is the deposition rate, θ is the sticking coefficient, and σ is the capture cross section of the bonding sites for hydrogen. For the present work, $[H_T]_{\max}$ was taken to be the highest hydrogen concentration of each of the three sets of films. Then $-\ln(1 - [H_T]/[H_T]_{\max})$ vs. $1/R$ was plotted for those samples which had a greater deposition rate than the sample which had the highest hydrogen concentration. A least squares fit was used to determine the lines through the data in Figs. 20a-20c. The results of these plots are given in Table 3.

If the deposition rate is measured in units of monolayers per second, the slope of the $-\ln(1 - [H_T]/[H_T]_{\max})$ vs. $1/R$ gives $F\theta\sigma$, see Eq. (60). For this work, R was measured in angstroms per second; therefore, it was necessary to divide the slope of the $-\ln(1 - [H_T]/[H_T]_{\max})$ vs. $1/R$ plot by the average monolayer thickness of a-Si:H to get $F\theta\sigma$. This thickness was assumed to be 2.45 Å, the interatomic

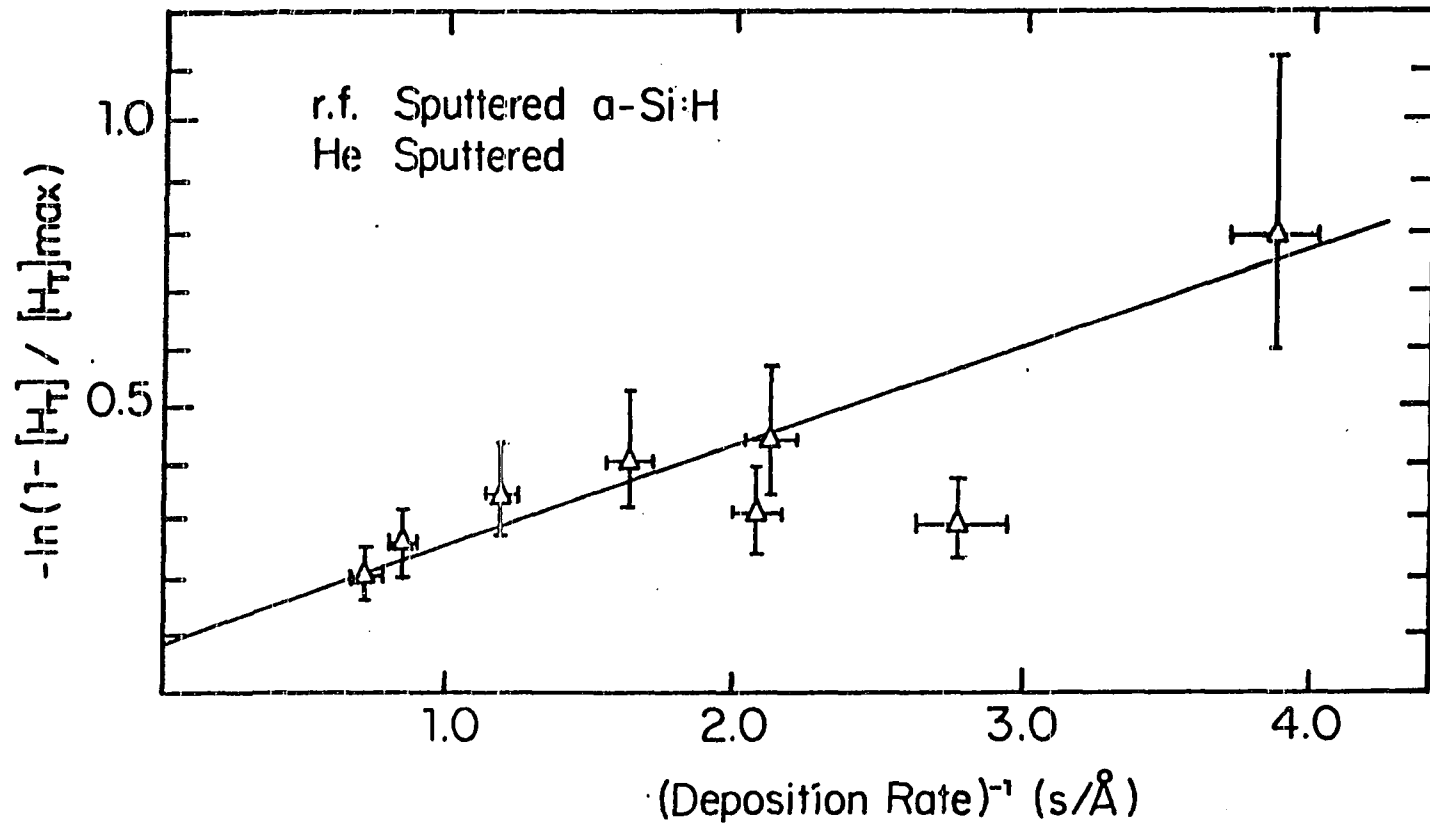


Fig. 20a. $-\ln(1 - [H_T] / [H_R]_{\max})$ vs. $1/R$ for the helium sputtered a-Si:H films, where $[H_T]$ is the total hydrogen concentration and R is the deposition rate

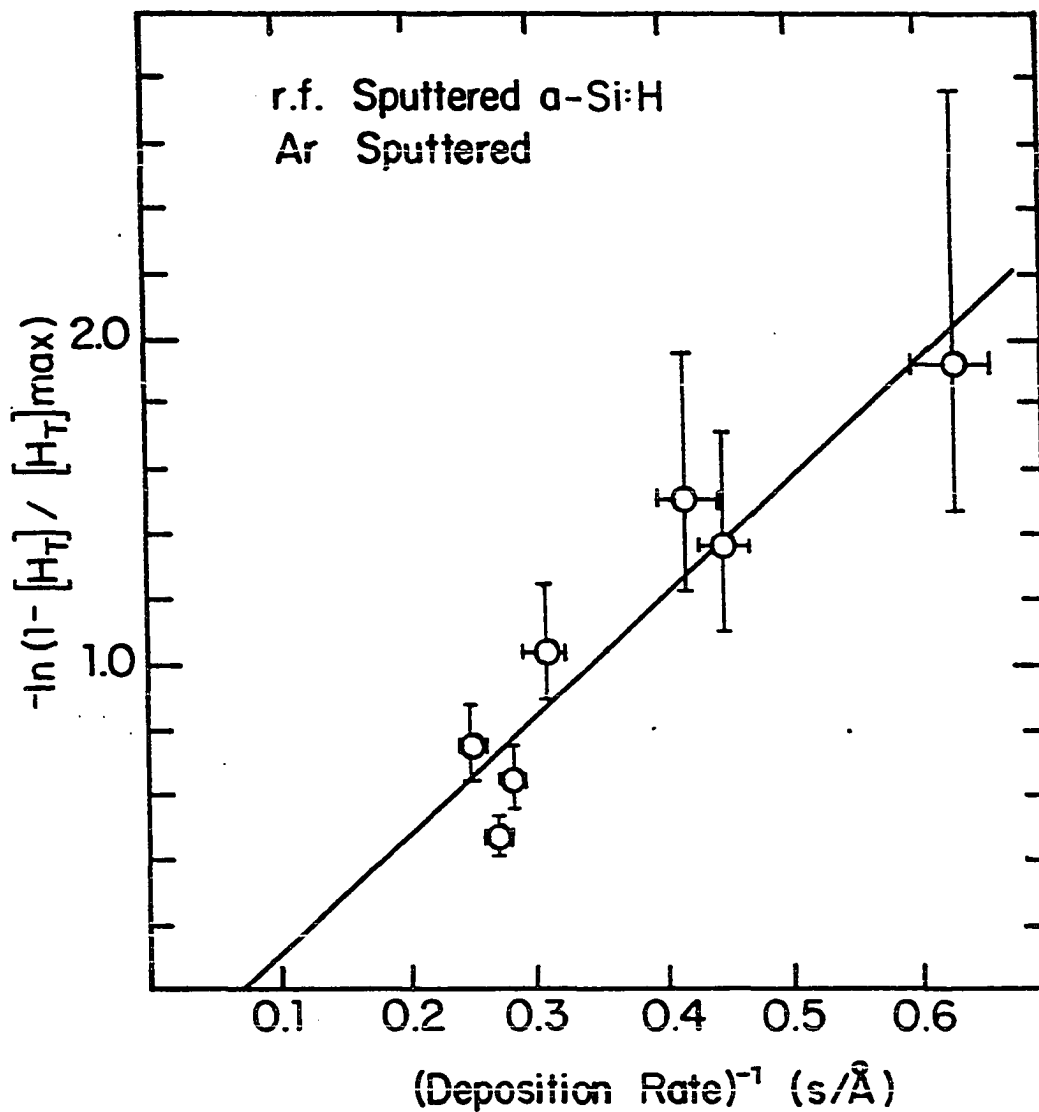


Fig. 20b. $-\ln(1 - [H_T] / [H_T]_{\max})$ vs. $1/R$ for the argon sputtered a-Si:H films, where $[H_T]$ is the total hydrogen concentration and R is the deposition rate

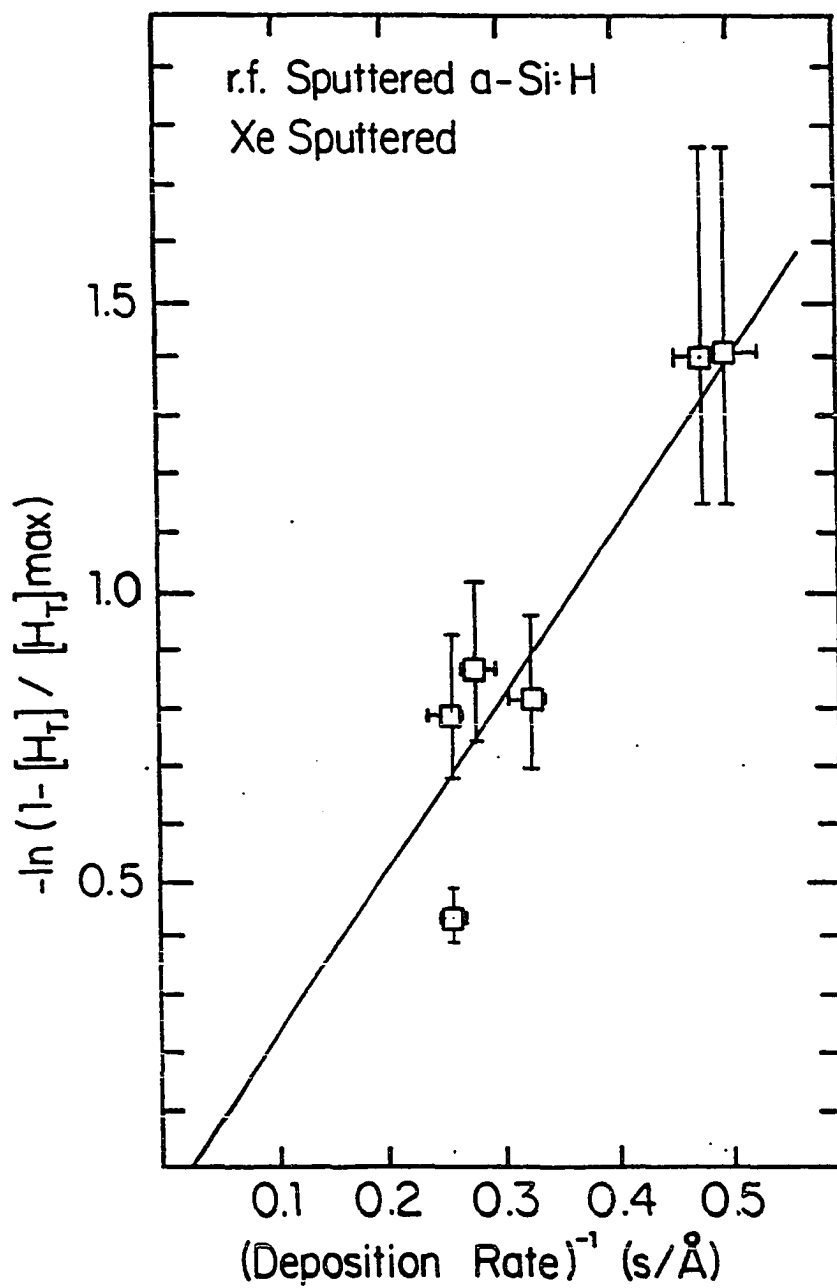


Fig. 20c. $-\ln(1 - [H_T] / [H_T]_{\max})$ vs. $1/R$ for the xenon sputtered a-Si:H films, where $[H_T]$ is the total hydrogen concentration and R is the deposition rate

Table 3. Results of $-\ln(1-[H_T]/[H_T]_{\max})$ vs. $1/R$ plots

Sputtering Gas	Slope of $-\ln(1-[H_T]/[H_T]_{\max})$	$F\theta\sigma(s^{-1})$	Least squares fit correlation coefficient	$\frac{F\theta\sigma}{(F\theta\sigma)_{\text{He}}}$
He	0.17	0.07	0.94	1
Ar	3.60	1.47	0.94	21
Xe	2.91	1.19	0.97	17

spacing of crystal silicon. The correlation coefficient gives a measure of how well the data fits a straight line. A correlation coefficient of ± 1 would correspond to a perfect linear fit. The boxes drawn around the data points in Figs. 20a-20c give the uncertainties in the data.

The data in Table 3 indicate that the product $F\theta\sigma$ is ~ 20 times larger when sputtering in Ar or Xe than when sputtering in He. However, the flux of hydrogen at the film surface, F , should be the same for all three sets of samples since F depends only on the partial pressure of hydrogen used when sputtering; and, this was always set at 0.5 mtorr. Thus, the difference must be in the product $\theta\sigma$. These changes in $\theta\sigma$ with sputtering gas could be the result of differing plasma-substrate interactions. Let us assume that the inert gas ions impinging on the growing film not only remove Si atoms but also break weak (or distorted) Si-Si bonds. The most effective sputtering gas would also be the most effective at breaking weak Si-Si bonds. Then this gas would provide the most available free silicon bond sites for hydrogen incorporation. In this way, σ (and hence $\theta\sigma$) would be the largest for sputtering in this gas. Likewise, $\theta\sigma$ would be the smallest when sputtering the gas which has the smallest sputtering yield. Figures 20a-20c demonstrate that this is the case with Ar sputtering having both the largest sputtering yield and $\theta\sigma$ while He sputtering has the lowest sputtering yield and $\theta\sigma$.

The concentration of silicon atoms bonded to more than one hydrogen atom, $[\text{Si-H}_2]$, was also determined. Figure 21 gives $[\text{Si-H}_2]$ vs. deposition rate for the three series of samples. As can be seen in Fig. 21, the concentration of silicon atoms bonded to more than one hydrogen atom tends to decrease with increasing deposition rate. Possible

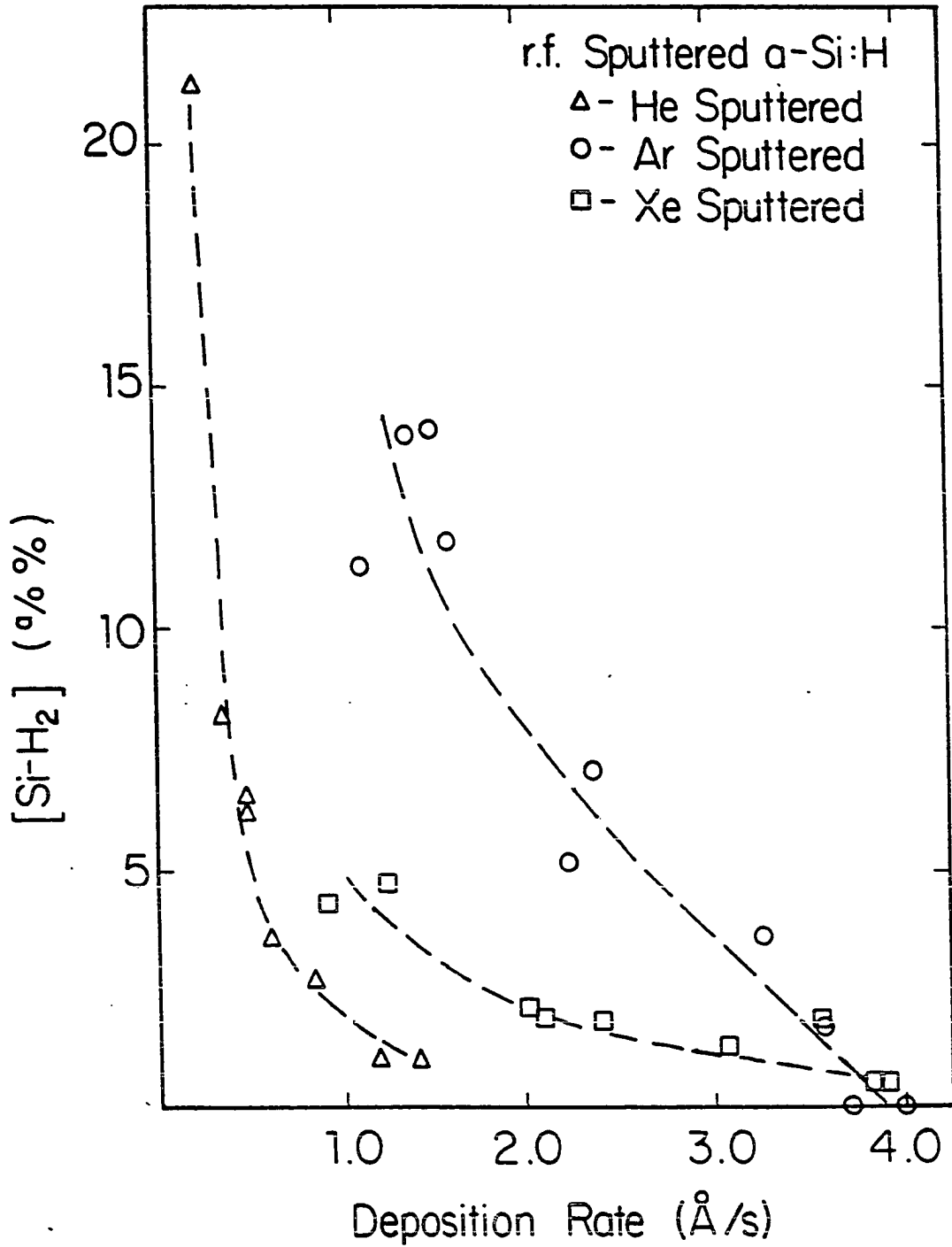


Fig. 21. [Si-H₂] vs. deposition rate for the three sets of r.f. sputtered a-Si:H films

reasons for the observed change in $[\text{Si-H}_2]$ with deposition rate include 1) increased probability of SiH_2 formation with increasing total hydrogen concentration, and 2) an increase in $[\text{Si-H}_2]$ due to an increase of "surface-like" morphology in the film.

Increasing $[\text{Si-H}_2]$ can be expected with increasing total hydrogen concentration from simple statistical considerations. Let us consider N boxes (silicon atoms available for hydrogen bonding) into which will be placed M balls (hydrogen atoms). Let N_1 be the number of boxes with one ball, and N_2 the number with two balls. For fixed values of N , N_1 , and N_2 , the number of ways this can be done is given by

$$W = \frac{N!}{N_1!N_2!(N-N_1-N_2)!} \quad (61)$$

and $M = N_1 + 2N_2$. (62)

By using Eq. (62) to substitute for N_1 in Eq. (61), one finds

$$W = \frac{N!}{N_1!N_2!(N-N_1-N_2)!} \quad (63)$$

If $\ln W$, and hence W , is maximized with the aid of Sterling's approximation for $\ln n!$, the most probable distribution of balls is found to occur when

$$N_2 = 1/6 [N + 3M \pm N \sqrt{1 + \frac{6MN - 3M^2}{N^2}}] \quad (64)$$

If $M = 0$ (no balls) then $N_2 = 0$ (no doubly occupied boxes) is expected. When $M = 0$, Eq. (64) gives

$$N_2 = \begin{cases} 1/3N & \text{for the (+) sign} \\ 0 & \text{for the (-) sign} \end{cases} \quad (65)$$

When $M = 2N$ (all boxes doubly occupied), then $N = N_2$ is expected. For $M = 2N$, Eq. (64) gives

$$N_2 = \begin{cases} 4/3N & \text{for the (+) sign} \\ N & \text{for the (-) sign} \end{cases} \quad (66)$$

Therefore, the (-) sign in Eq. (64) must be chosen. Assuming $(6MN - 3M^2)/2N^2 \ll 1$ and using the approximation $(1 - \epsilon)^{1/2} \approx 1 - \epsilon/2$ for $\epsilon \ll 1$, Eq. (64) becomes

$$N_2 \sim \frac{M^2}{4N} \quad (67)$$

If it is assumed that silicon bond filling by hydrogen is indeed a random, statistical process, that the number of bonding sites N is independent of deposition rate, and that the temperature of the substrates is independent of the sputtering power, then $[\text{Si-H}_2]$ should be given by

$$[\text{Si-H}_2]^{1/2} = \frac{1}{\sqrt{2N}} [H_T] \quad (68)$$

Plots of $[\text{Si-H}_2]^{1/2}$ vs. $[H_T]$ for the three sets of samples are given in Figs. 22a-22c. A least squares fit was used to determine the lines through the data in Figs. 22a-22c. The results of these plots are given in Table 4.

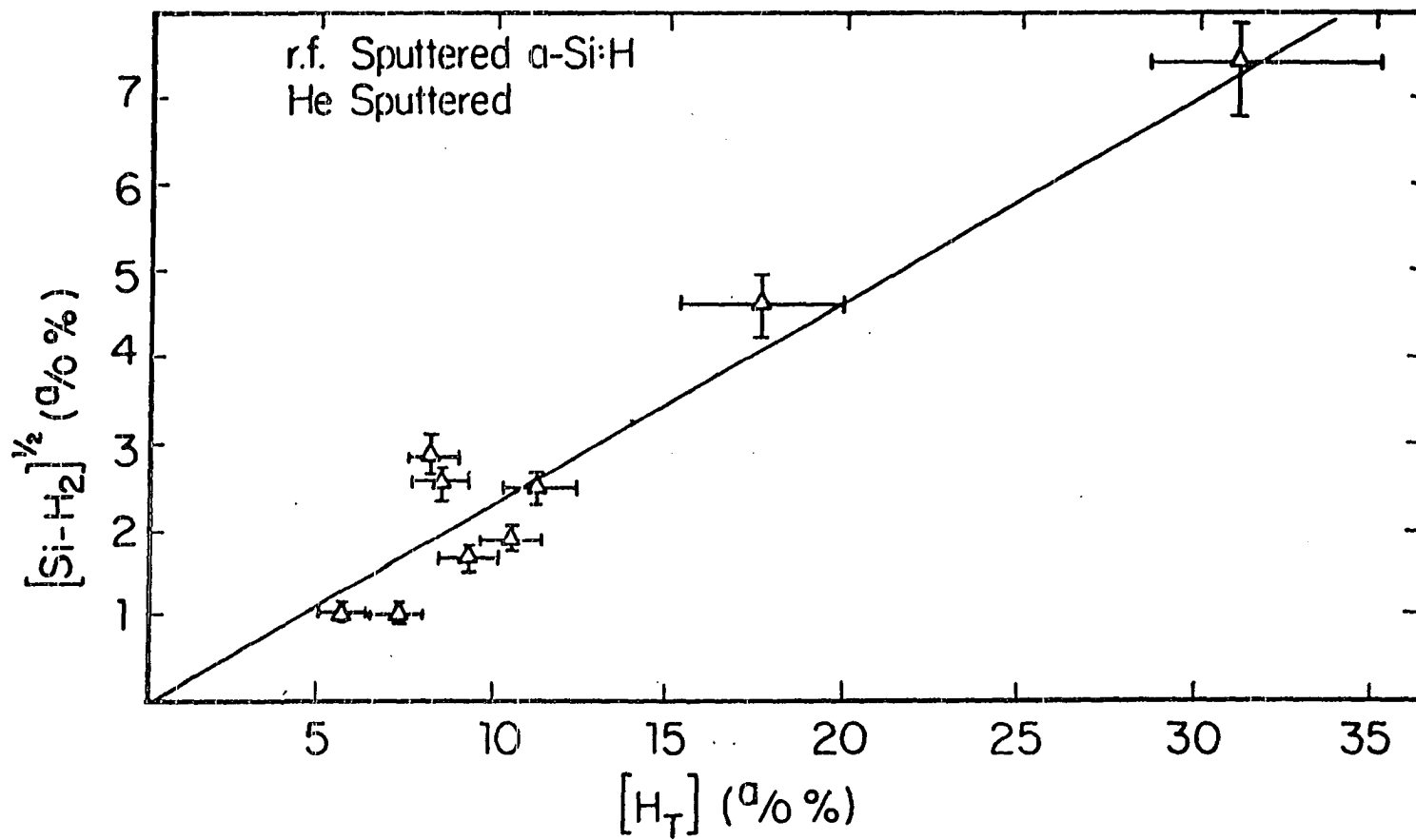


Fig. 22a. $[\text{SiH}_2]^{1/2}$ vs. $[\text{H}_T]$ for the helium sputtered a-Si:H films

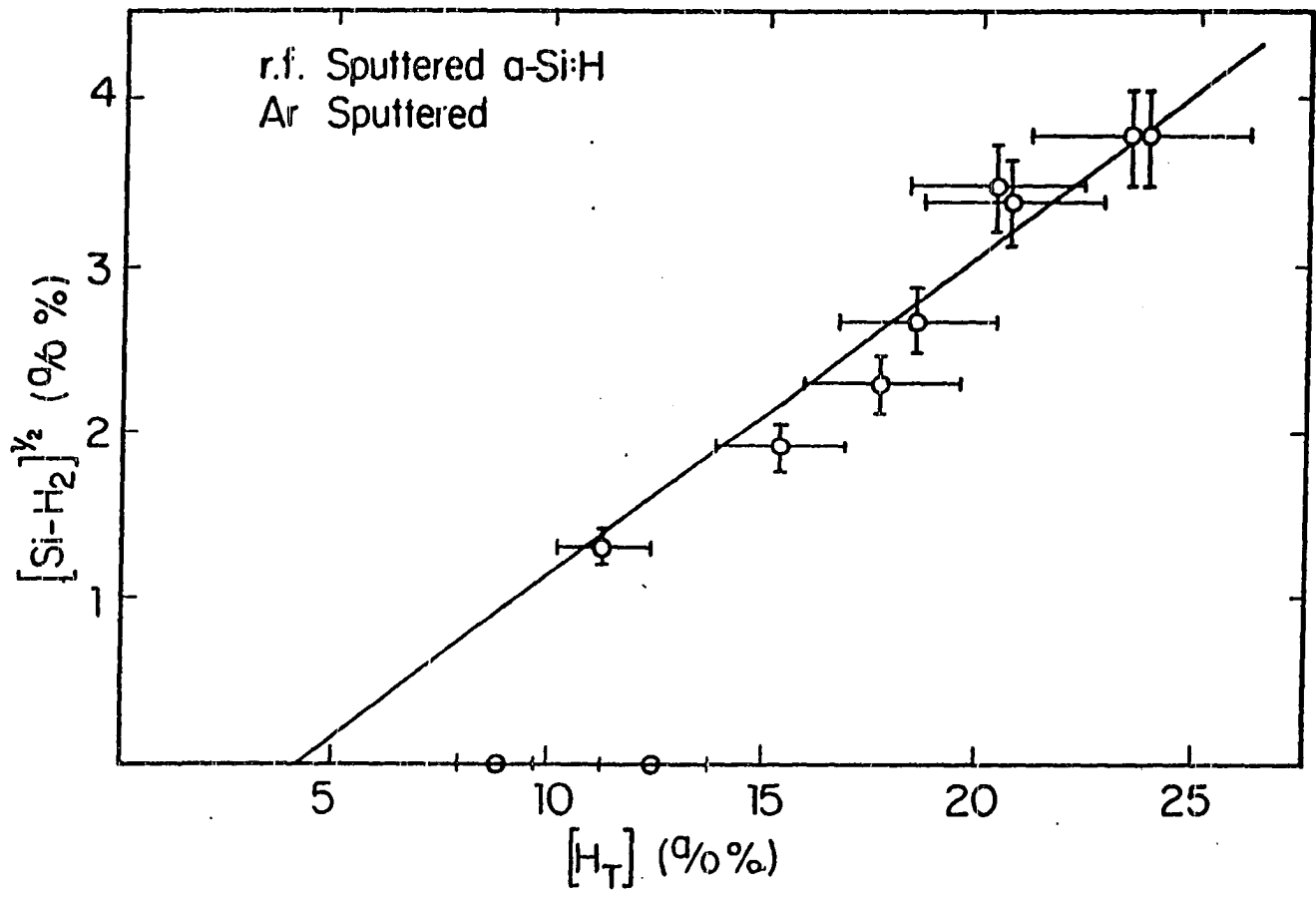


Fig. 22b. $[\text{SiH}_2]^{1/2}$ vs. $[\text{H}_T]$ for the argon sputtered a-Si:H films

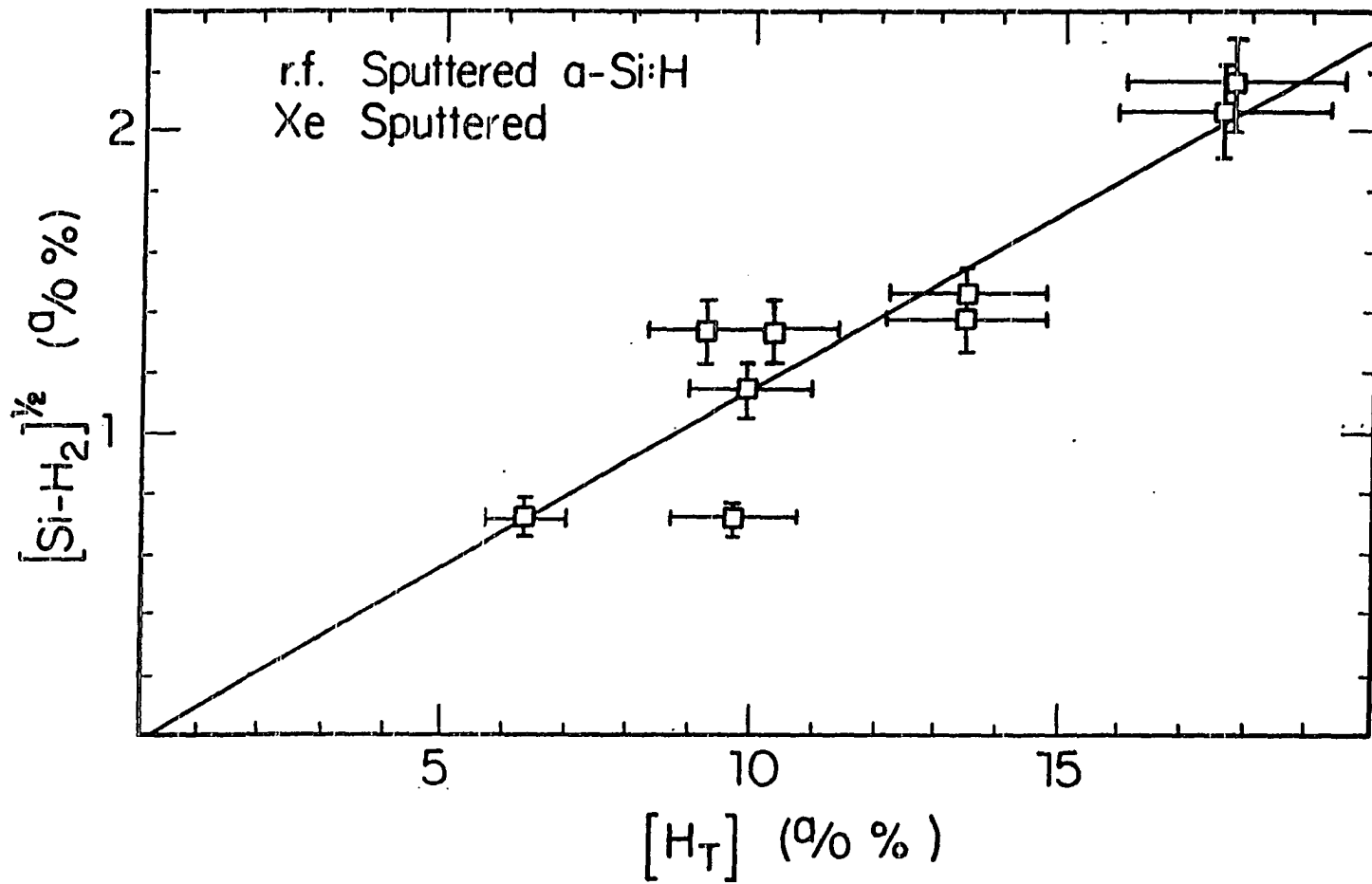


Fig. 22c. $[\text{SiH}_2]^{1/2}$ vs. $[\text{H}_T]$ for the xenon sputtered a-Si:H films

Table 4. Results of a fit to a random incorporation model for [Si-H₂] concentration

Sputtering Gas	Slope of [SiH ₂] ^{1/2} vs. [H _T]	(2[H _T] _{max}) ^{-1/2}	Least squares fit correlation coefficient
He	0.24	0.13	0.97
Ar	0.17	0.15	0.97
Xe	0.12	0.17	0.97

The slope of these plots should be equal to $(2N)^{-1/2}$ where N is the number of silicon atoms which are available to bond to one or more hydrogen atoms. Therefore, the total concentration of hydrogen for the sample having the most hydrogen in each series should be a good estimate of N. This model seems to give a good qualitative description of the situation. This can be seen in the qualitative agreement between the slopes of [Si-H₂]^{1/2} vs. [H_T] plots and $(2[H_T]_{max})^{-1/2}$ as well as in the high correlation coefficients for these plots. However, this random bonding model does not completely explain the observed concentrations of silicon atoms bonded to more than one hydrogen atom. For the Xe sputtered samples (Fig. 22c) there is a very small range of values for [Si-H₂]^{1/2} and a good deal of scatter to the plot. Therefore, these data do not allow a judgment to be made on the accuracy of this model. For the Ar sputtered samples, Fig. 22b indicates that the predicted values of [Si-H₂]^{1/2} are too high for the low [H_T] data points. Indeed, for two of the samples [Si-H₂] was equal to zero. These samples were prepared at the highest sputtering powers used, 500W and 600W. This indicates an abrupt decrease in the number of silicon atoms available to

bond to more than one hydrogen atom when these high r.f. sputtering powers were used. Figure 23 is a plot of $[\text{Si-H}_2]^{1/2}/[\text{H}_T]$ vs. sputtering power for the He sputtered samples. This plot indicates that for the He sputtered samples, the number of sites preferring double hydrogen occupancy generally increases with decreasing sputtering power. Since double hydrogen occupancy is associated with internal surfaces, ¹⁴⁻²⁶ these data suggest two results. First, the concentration of silicon atoms bonded to more than one hydrogen atom is controlled by both the total hydrogen concentration and the concentration of silicon bonding sites available for double hydrogen bonding. Second, it suggests that with decreasing sputtering power the number of bonding sites which will allow SiH_2 formation increases, probably due to increasing internal surface area in the films.

While the treatment above partially explains the behavior of $[\text{Si-H}_2]$ within each of the three sets of samples, it does not explain the differences in $[\text{Si-H}_2]$ between the three sets of samples. Even allowing for a factor of two differences in the prefactors A^* used to determine $[\text{Si-H}_2]$, the He sputtered films have much higher values of $[\text{Si-H}_2]$ than either the Ar or Xe sputtered films. These differences can be explained in terms of the different morphologies of the films; and, these morphologies are apparently determined by plasma-film interactions during the deposition. The He sputtered films show post-depositional oxidation when exposed to air. This indicates the possible existence of columnar morphology in the film with the oxygen diffusing down the sides of the columns. The samples sputtered in Ar and Xe show no signs of post-depositional oxidation and are, therefore, believed to be free of

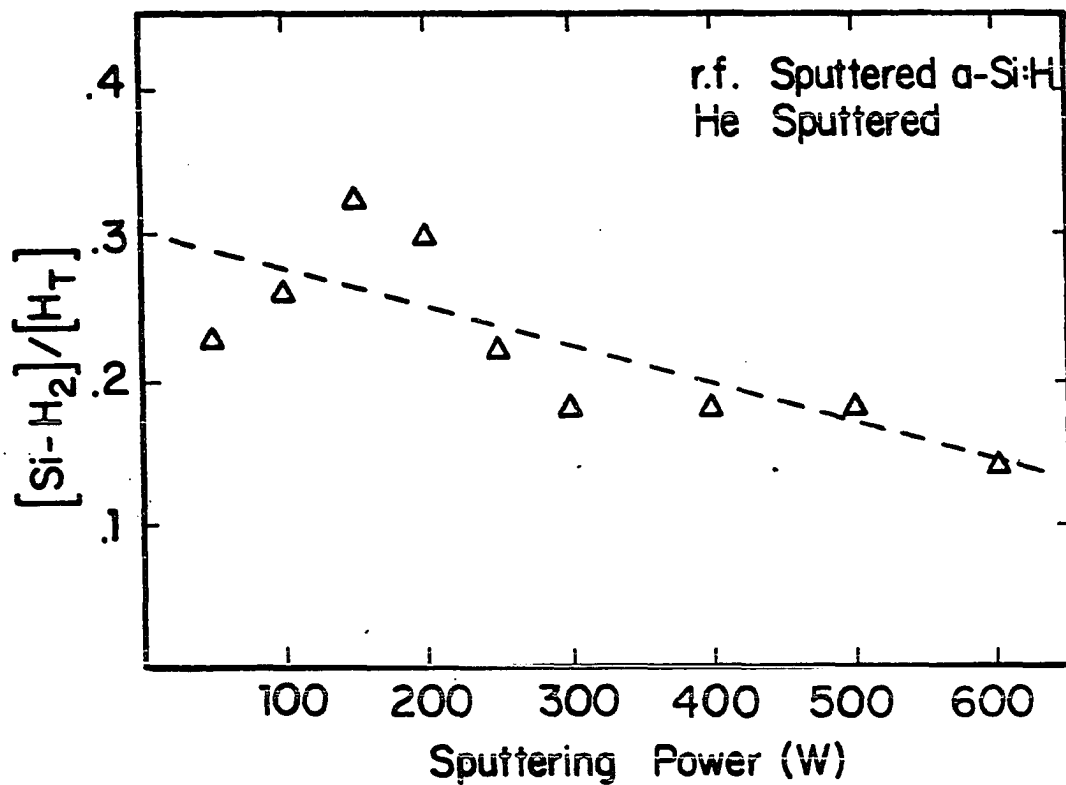


Fig. 23. $[\text{SiH}_2]^{1/2}/[\text{H}_T]$ vs. sputtering power for the helium sputtered a-Si:H films

columnar morphology. Columnar morphology is the result of a growth process in which the film starts to grow at many separate nucleation points. As these islands grow to cover the surface of the substrate, they eventually meet and merge together. When these islands merge, the atoms at their surfaces can either rearrange themselves to form a continuous amorphous network or boundaries between the islands can form. On these boundaries there are silicon atoms bonded to three or less silicon atoms and silicon atoms only weakly bonded to other silicon atoms. The under coordinated Si atoms on these surfaces provided additional bonding sites for the formation of SiH and SiH₂.

Bombardment of the film surface by the plasma gives momentum to the silicon atoms which helps them to rearrange themselves and prevents the columnar growth morphology. In He sputtering, the plasma-film interactions are not strong enough to prevent columnar growth. This lack of film bombardment by the He/H₂ plasma can have two effects on the hydrogen incorporation in the film. The column surfaces can provide more bonding sites for the hydrogen while the inability of the plasma backscattering of the film to break weak Si-Si bonds would reduce the number of these bonding sites. The data would suggest that the non-breaking of weak bonds is the dominant effect when sputtering in He at high r.f. sputtering powers. These samples have very low SiH and SiH₂ concentrations when compared to samples sputtered in Ar or Xe with similar deposition rates. However, the concentration of SiH and SiH₂ grows very large for the He sputtered films prepared at low r.f. sputtering powers. This indicates the presence of columnar morphology in these films is becoming the dominant factor in determining the hydrogen concentrations.

D. Unpaired Dangling Bond Spin Densities

Electron spin resonance (ESR) was used to measure the density of unpaired dangling bonds in the three sets of samples. Brodsky and Kaplan⁴⁹ have shown that only one to ten percent of the dangling bonds in an a-Si sample are detected by ESR. This reduction in ESR signal is caused by dangling bonds pairing across microvoids and cancelling each other's signals. It is unknown to what extent this signal reduction depends on the structure of the films. Therefore, since the films sputtered with different inert gases are believed to have different microstructures (e.g., the columnar morphology believed to be present in the He sputtered films) the dangling bond spin densities as measured by ESR should only be compared within series of films sputtered with the same inert gas. The uncertainty in the values for the unpaired dangling bond spin density was found by measuring this value for sample number 103 on five separate occasions. The standard deviation in these values gave the uncertainty to be thirty percent.

As mentioned earlier, the samples prepared in a He/H₂ atmosphere oxidized when exposed to air unless they were coated with a thin Ar/H₂ sputtered layer. The Ar sputtered coating prevented post depositional oxidation for several days during which time thickness, infrared and optical density measurements were made. The ESR measurements were performed approximately five months after deposition, by which time some of the He sputtered films had begun to oxidize. The unpaired dangling bond spin densities for these samples are given in Table 2 and marked with an asterisk. Note that these samples had much lower unpaired dangling bond spin densities than those sputtered in He which did not

oxidize. This is to be expected since oxygen introduced to the a-Si:H film would probably bond to dangling bonds. Thus, the previously unpaired dangling bond electron would then share a bonding orbital with an electron from the oxygen and the spins of these two electrons would cancel. In the following, only the unpaired dangling bond spin densities for those samples which had not oxidized by the time the ESR measurement was made will be considered.

Figures 24 and 25 give unpaired dangling bond spin densities vs. sputtering power and depositing rate, respectively, for the three sets of samples. The unpaired dangling bond spin density decreases both with increasing sputtering power and increasing deposition rate for all three sets of samples. The dangling bond density seems to reach a minimum of $\sim 1.4 \times 10^{18} \text{ cm}^{-3}$ and $\sim 1 \times 10^{17} \text{ cm}^{-3}$ for the He and Ar sputtered samples, respectively. This minimum occurs at $\sim 200\text{W}$ rf sputtering power for the He sputtered samples at $\sim 300\text{W}$ r.f. sputtering power for the Ar sputtered samples. This behavior is in sharp contrast to that observed in a-Si:H samples produced by glow discharge of silane,^{50,51} where the dangling bond spin density is observed to increase with increasing rf sputtering power and deposition rate. In the glow discharge produced samples the increase in dangling bonds is associated with a decrease in hydrogen content of the film.

Hydrogen added to a-Si is believed to passivate dangling bonds and thereby lower the dangling bond ESR signal. Connell and Pawlik⁵² demonstrated a linear relationship between the dangling bond ESR signal intensity and the amount of hydrogen incorporated into r.f. sputtered a-Ge films. These data showed a decreasing spin density with increasing

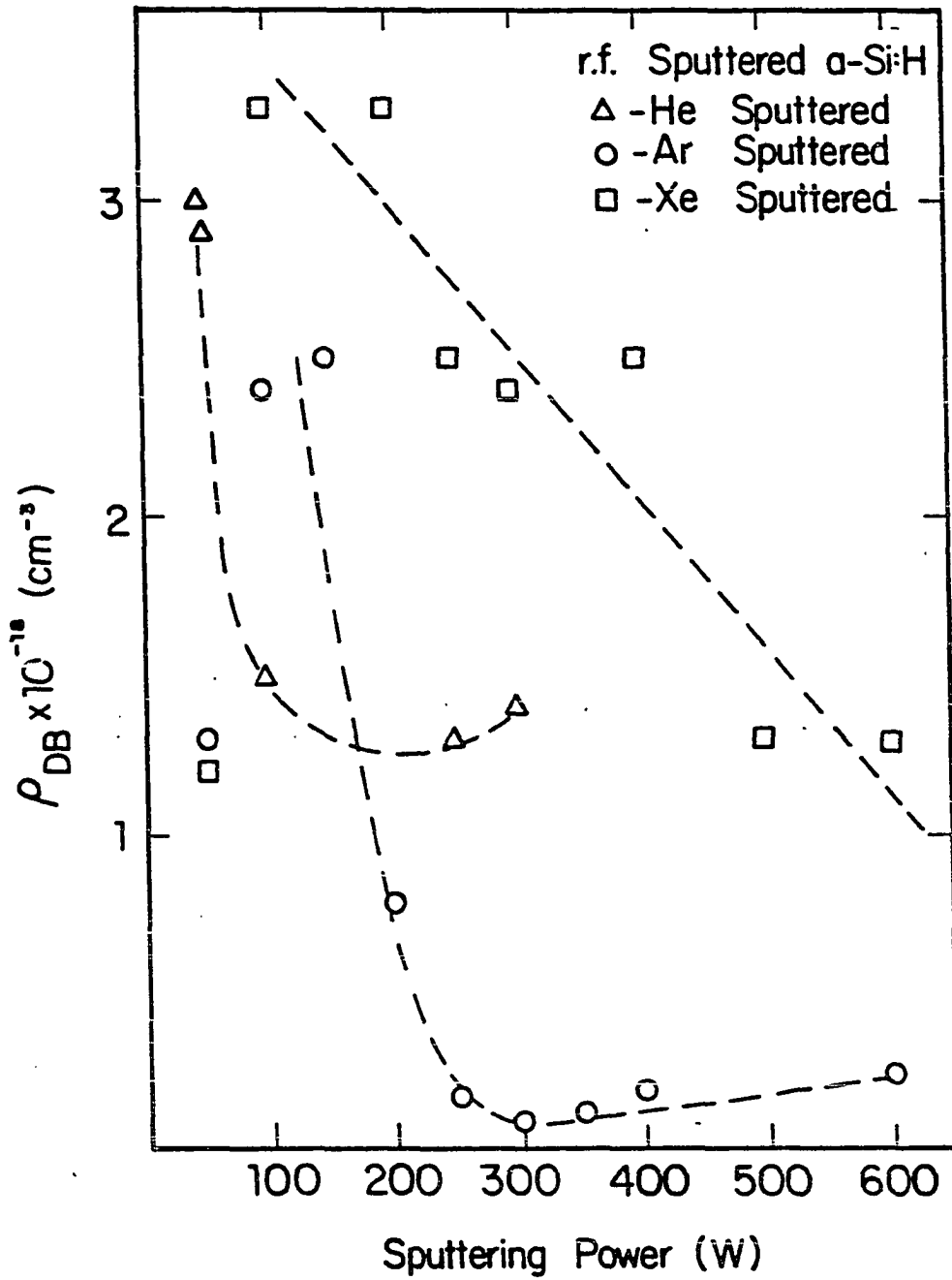


Fig. 24. Unpaired dangling bond spin density vs. sputtering power for the three sets of r.f. sputtered a-Si:H films

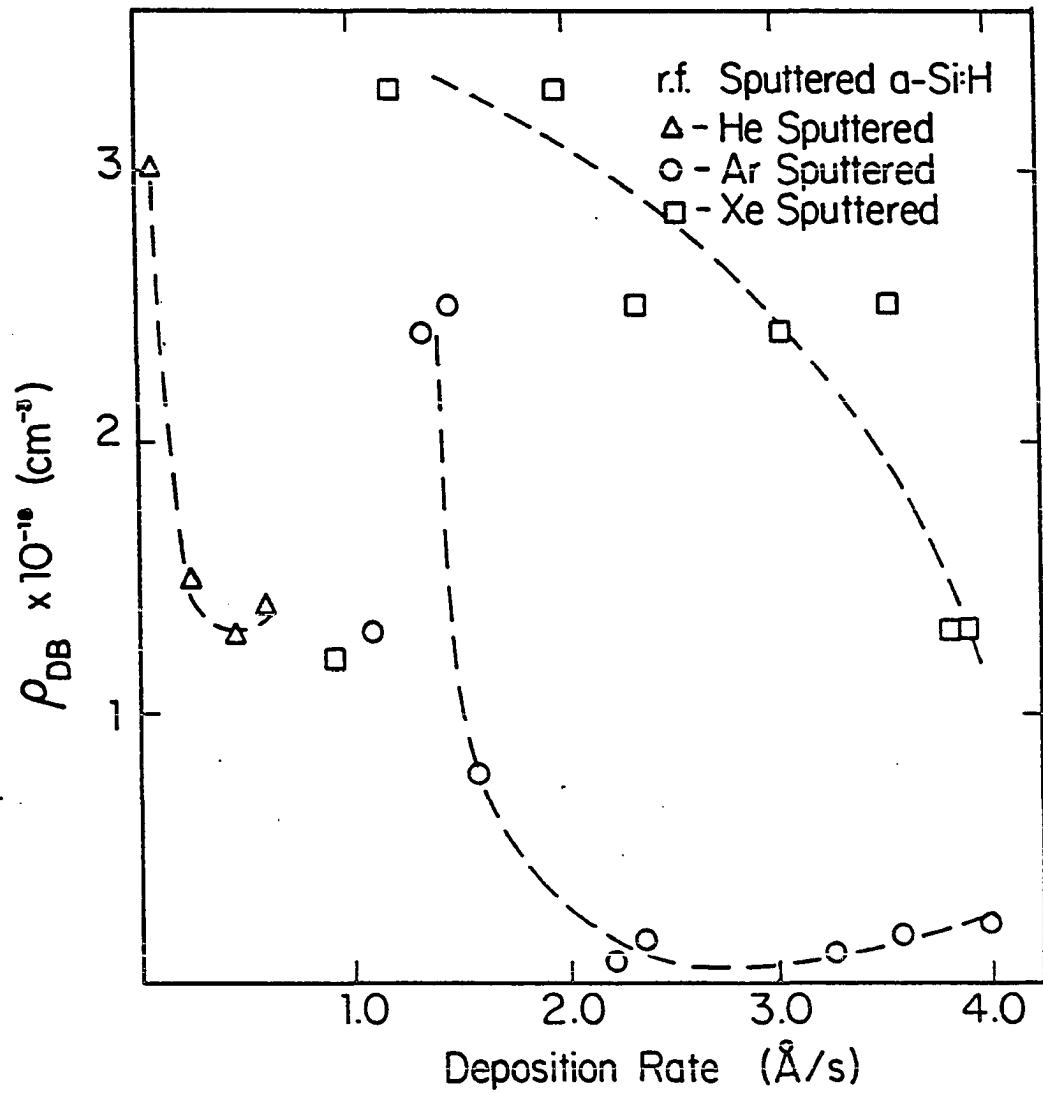


Fig. 25. Unpaired dangling bond spin density vs. deposition rate for the three sets of r.f. sputtered a-Si:H films

hydrogen concentration. The slope of these data indicated that a spin is measured for only about every 100 electrons in dangling bonds. Knights et al.⁵¹ found an increase in spin density with increasing hydrogen concentration. However, in the work of Knights et al., the hydrogen concentration was varied by varying the temperature of the substrates. Higher substrate temperatures gave lower hydrogen concentrations and lower spin densities. This can be explained by assuming that at higher substrate temperatures the growing film is better thermally annealed, thereby reducing the density of dangling bonds. Also, Paul et al.⁵³ have correlated the density of dangling bonds in a-Si to the surface area of microvoids in the materials. Thus, while hydrogen passivates dangling bonds in a-Si:H, it is not the lone parameter in influencing the dangling bond density. The microstructure of the film, which is determined by the film's deposition conditions, also effects the dangling bond density.

Unpaired dangling bond spin density, ρ_{DB} , vs. hydrogen concentration for this work is given in Fig. 26. For the Xe sputtered samples, the dangling bond spin density increases nearly monotonically with increasing hydrogen concentration. For $10\% < [H_T] < 17\%$, the He and Ar sputtered samples show nearly constant dangling bond densities of $\sim 1.4 \times 10^{18} \text{ cm}^{-3}$ and $\sim 1 \times 10^{17} \text{ cm}^{-3}$, respectively. For $[H_T]$ greater than 17%, both the He and Ar sputtered samples show a marked increase in unpaired dangling bond spin densities. In Figs. 27a and 27b, the same qualitative dependence of ρ_{DB} on $[Si-H_2]$ as $[H_T]$ can be seen.

As has been discussed earlier, there are two parameters which control the unpaired dangling bond spin densities in a-Si:H. First,

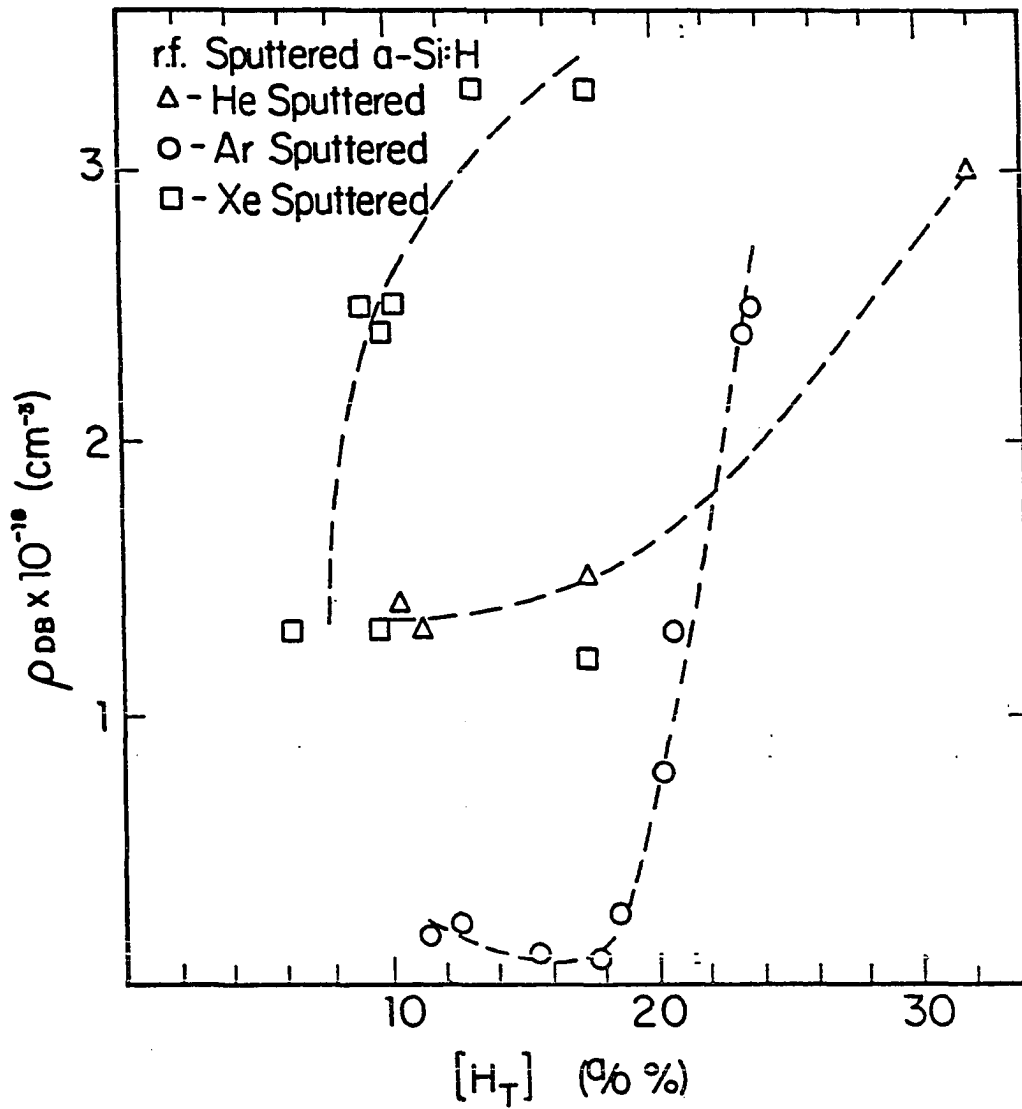


Fig. 26. Unpaired dangling bond spin density vs. $[H_T]$ for the three sets of r.f. sputtered a-Si:H films

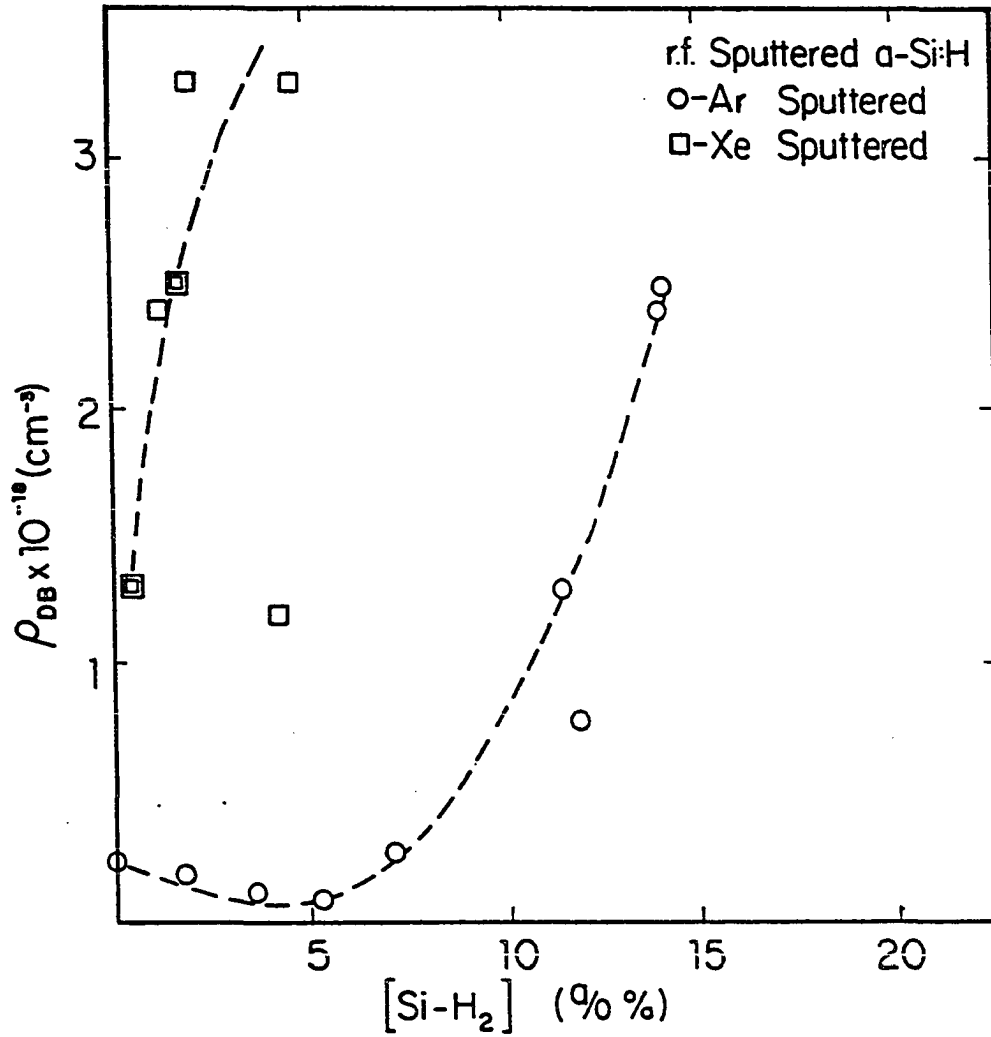


Fig. 27a. Unpaired dangling bond spin density vs. $[\text{Si-H}_2]$ for the Ar and Xe sputtered a-Si:H films

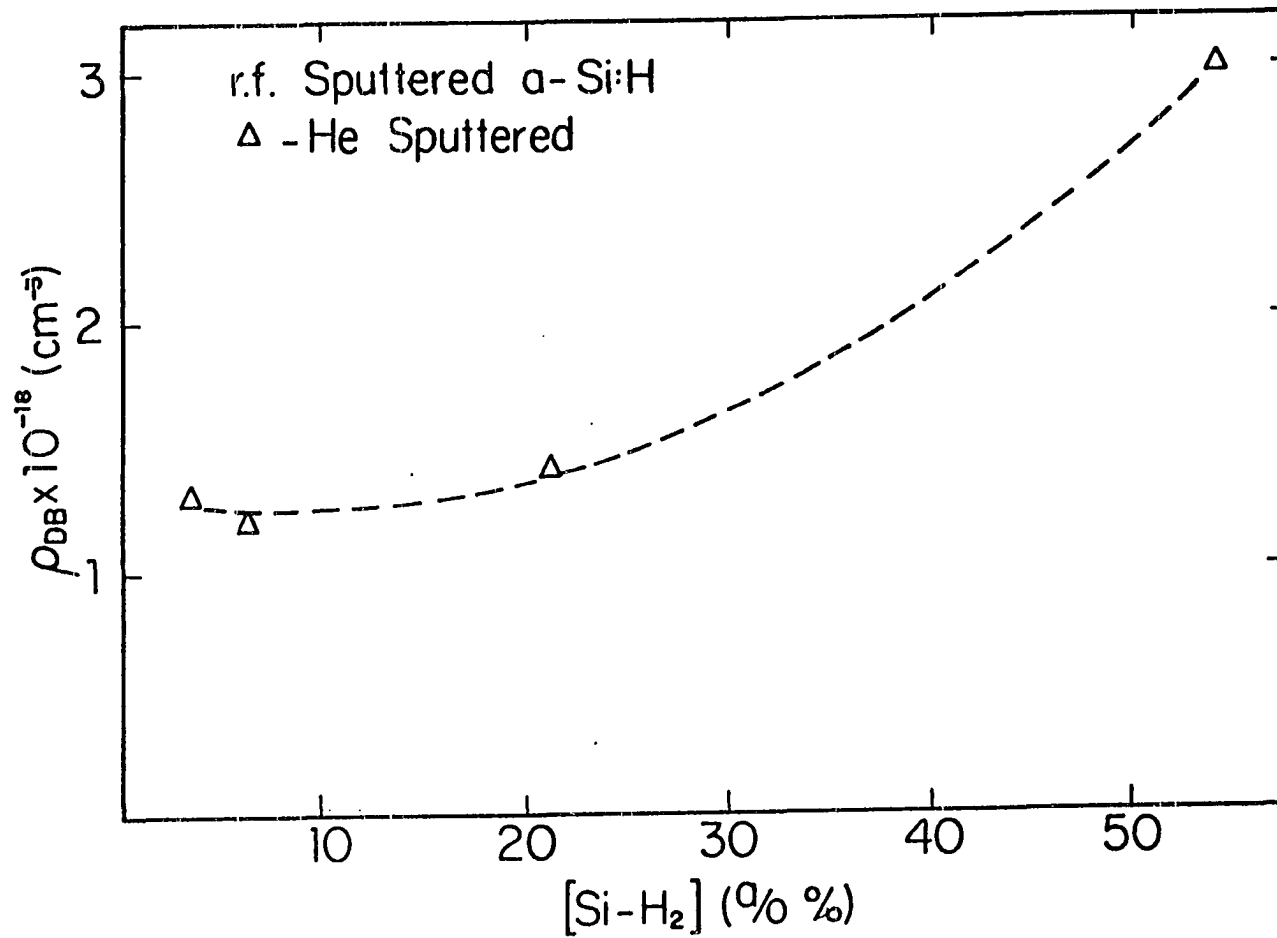


Fig. 27b. Unpaired dangling bond spin density vs. [Si-H₂] for the He sputtered a-Si:H films

increasing hydrogen concentration reduces ρ_{DB} by passivating dangling bonds. Second, increasing internal microvoid or columnar surface areas increase ρ_{DB} . It is obvious that for those samples which have increasing ρ_{DB} with increasing $[H_T]$ the second of these effects is dominant. A great deal of work¹⁶⁻²⁶ has shown $[Si-H_2]$ to be roughly proportional to the surface area of microvoids and columns in a-Si:H. Also, the work of Paul et al.⁵³ has shown ρ_{DB} to be proportional to the surface area of microvoids and columns in a-Si. Therefore, for those samples in which the dominant effect on ρ_{DB} is the internal surface areas, it is reasonable to assume

$$\rho_{DB} \sim A[Si-H_2] \quad (69)$$

If it is assumed that the number of dangling bonds per unit internal surface area is the same for the three sets of samples, then the constant A in Eq. (69) will give a measure of what fraction of the dangling bonds do not pair and cancel their ESR signals for each set of samples.

Listed in Table 5 are the results of a least squares fit of ρ_{DB} vs. $[Si-H_2]$, the plots of these data are in Fig. 28.

Table 5. Results of ρ_{DB} vs. $[Si-H_2]$

Sputtering Gas	A(arb units)	A_{Xe}/A	Correlation Coefficient
He	4.3×10^{-16}	25.6	--
Ar	3.3×10^{17}	3.33	0.99
Xe	1.1×10^{18}	1	0.96

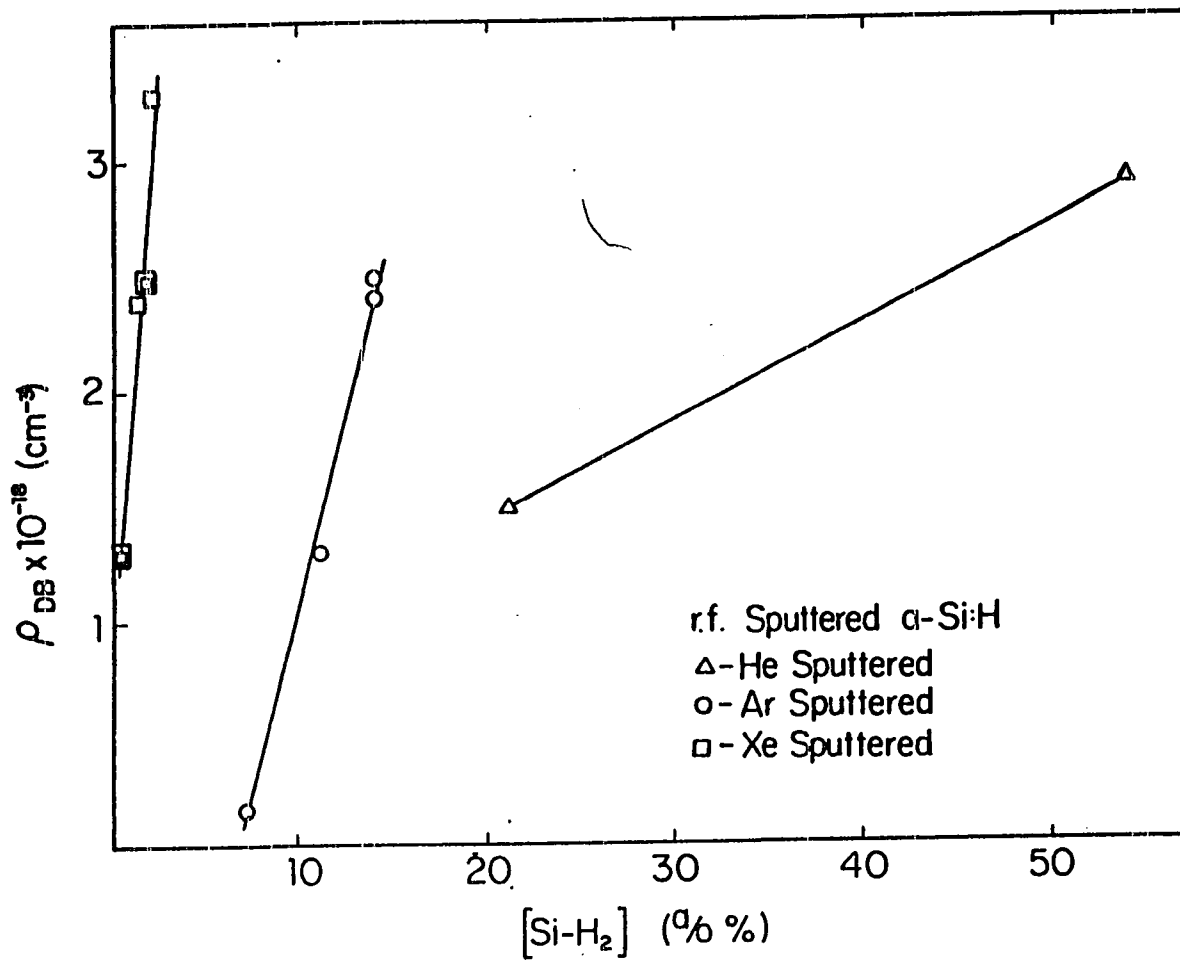


Fig. 28. Unpaired dangling bond spin density vs. [Si-H₂] which show increasing ρ_{DB} with increasing [H_T]

It should not be forgotten that $[\text{Si-H}_2]$ was determined using the infrared $850\text{--}890\text{ cm}^{-1}$ bond bending mode for which the oscillator strength may vary for samples deposited in different atmospheres. However, the results above do suggest that there are differences in the degree to which the observed spin densities are lowered by spin pairing in the different series of samples. The He sputtered samples had the smallest proportionality constant between ρ_{DB} and $[\text{Si-H}_2]$. This indicates that they are much more effective at pairing up spins and effectively "hiding" their dangling bonds from detection by ESR. The Ar and Xe sputtered samples have much larger proportionality constants and their dangling bonds are therefore "more exposed." These differences in spin pairing abilities may be due to differences in the morphologies of the films.

The pairing of dangling bonds yields weak Si-Si bonds. An estimate of the relative concentrations of these weak Si-Si bonds can be made using

$$[\text{WB}] = \frac{A_{\text{Xe}}}{A_{\text{x}}} \frac{\rho_{\text{DB}}}{\rho_{\text{DB, Xe}}^{\text{min}}} \quad (70)$$

In Eq. (70), $[\text{WB}]$ is the density of weak Si-Si bonds normalized to the density of weak Si-Si bonds in the Xe sputtered sample with the fewest unpaired dangling bonds. The ratio $A_{\text{Xe}}/A_{\text{x}}$ ($x=\text{He, Ar or Xe}$) accounts for the differences in spin pairing abilities. Figure 29 gives $[\text{WB}]$ vs. sputtering power for the three sets of samples. In Fig. 29, a familiar theme is observed. The samples sputtered in a He/H_2 atmosphere were exposed to less plasma film interactions during the deposition than

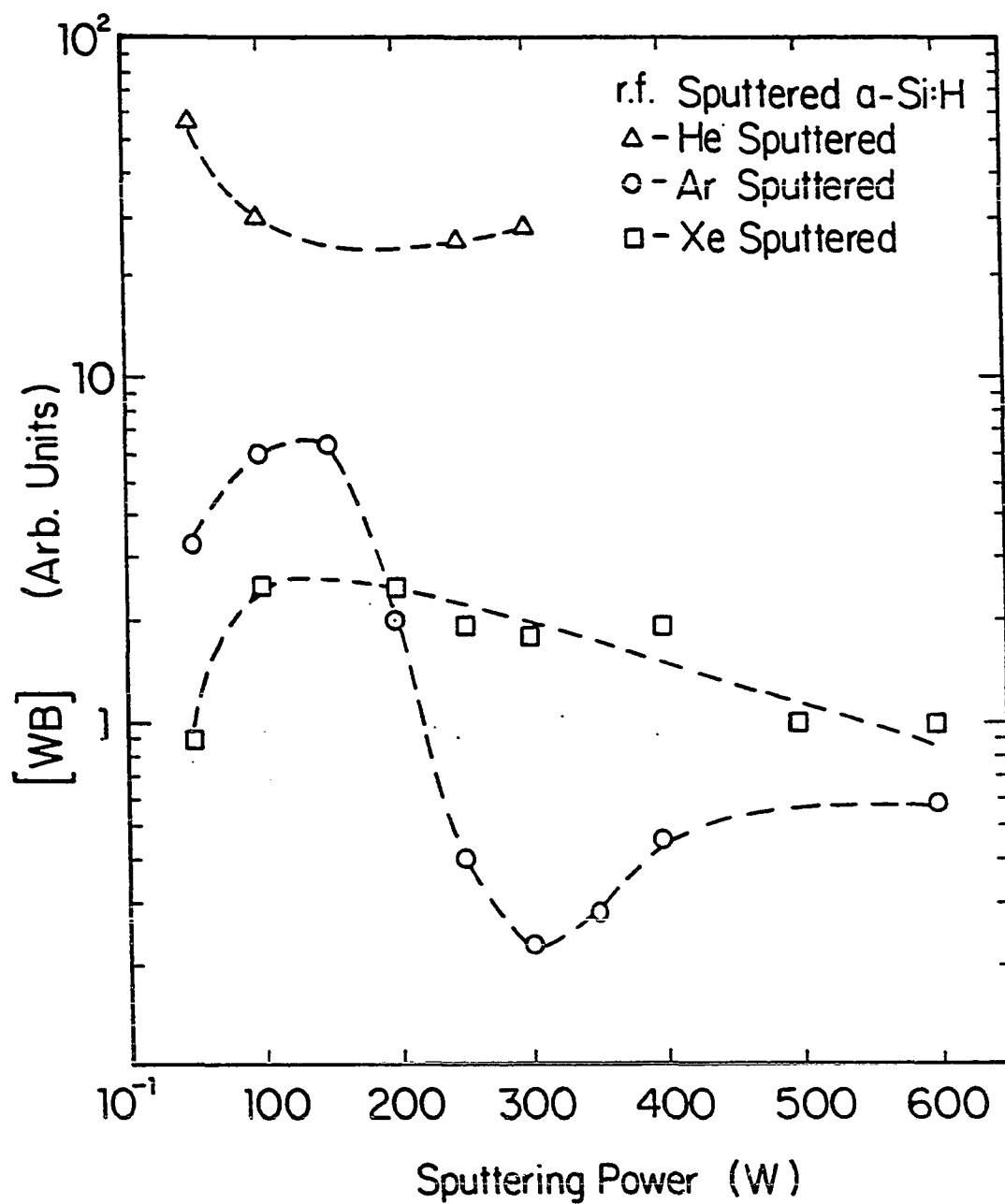


Fig. 29. Relative density of weak Si-Si bonds ([WB]) vs. sputtering power for the three sets of r.f. sputtered a-Si:H films

those sputtered in an Ar/H₂ or an Xe/H₂ atmosphere. This lack of plasma-film interactions caused a smaller number of weak Si-Si bonds to be broken. These weak Si-Si bonds may be the result of dangling bonds on internal surfaces which have "bent" to pair orbitals. With increasing sputtering power (and an associated increase in plasma-film interactions), there is an increase in the breaking of these weak bonds. Sputtering in Ar and Xe give very similar results, with Ar being slightly more efficient at breaking weak bonds. This can be related to Ar being slightly more effective at sputtering silicon than Xe.

B. Optical Measurements

Optical transmission measurements were used to determine the absorption coefficient, α , as a function of energy for the samples. In Fig. 30 are some typical $\sqrt{E\alpha n}$ vs. E plots used to determine the optical band gap as discussed earlier. Both the slopes and the $\sqrt{E\alpha n} = 0$ intercepts of these plots are of interest. The energy at which $\sqrt{E\alpha n}$ extrapolates to zero is interpreted as the optical energy gap; and, the slope is a measure of the "order" in the system. A larger slope implies a higher density material and/or a larger overlap of valence and conduction band wave functions (i.e., less localization due to disorder).

Figure 31 gives $E_{\text{gap}}^{\text{optical}}$ vs. $[H_T]$ for the three sets of samples. For all three sets of films, $E_{\text{gap}}^{\text{optical}}$ tends to increase with increasing hydrogen incorporation. But only for Ar sputtered samples is this increase nearly linear. Other workers⁵⁴⁻⁵⁶ have also seen a linear relationship between $E_{\text{gap}}^{\text{optical}}$ and $[H_T]$ for Ar sputtered films. The

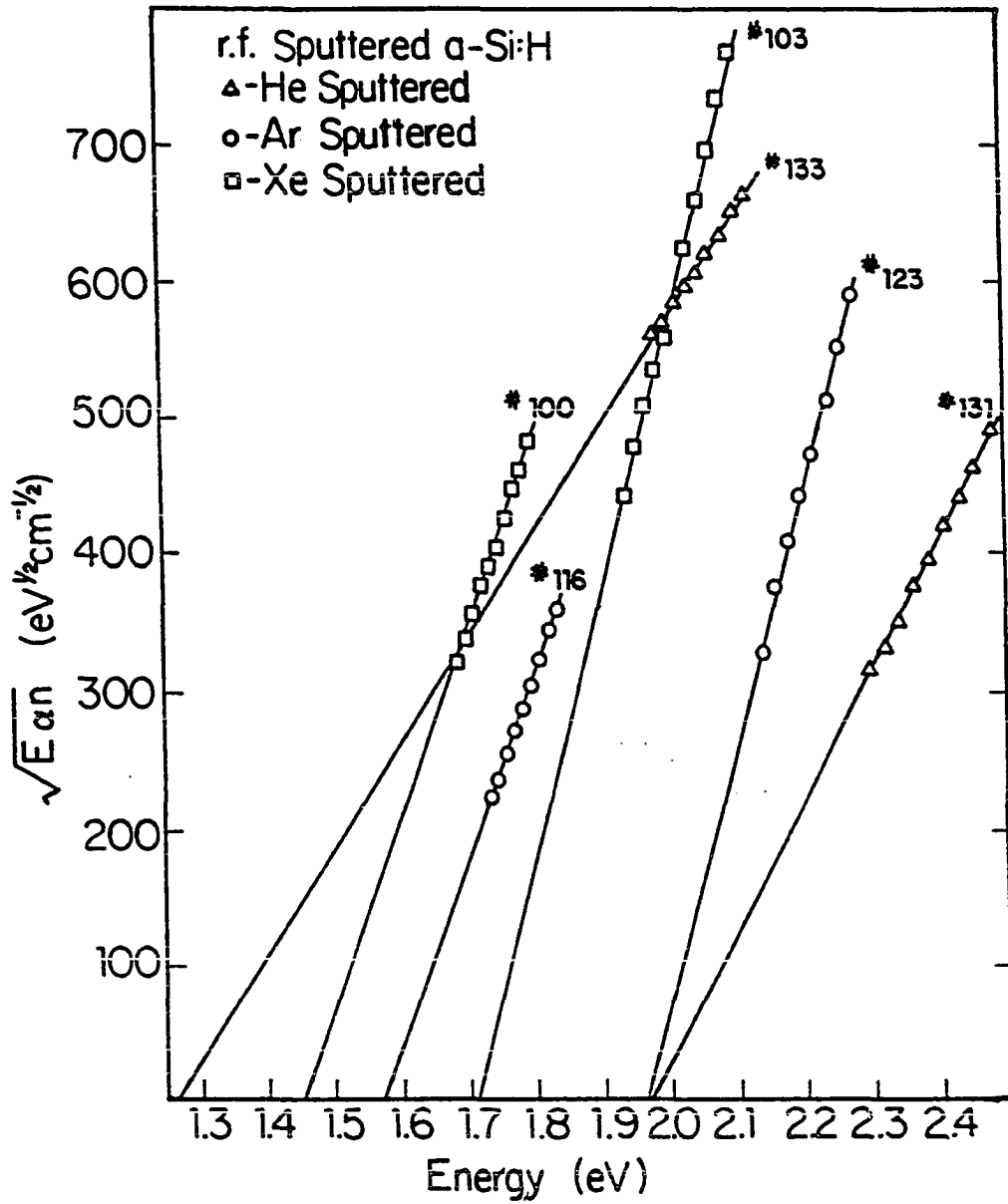


Fig. 30. $\sqrt{E\alpha_n}$ vs. E plots for the He, Ar, and Xe r.f. sputtered α -Si:H films

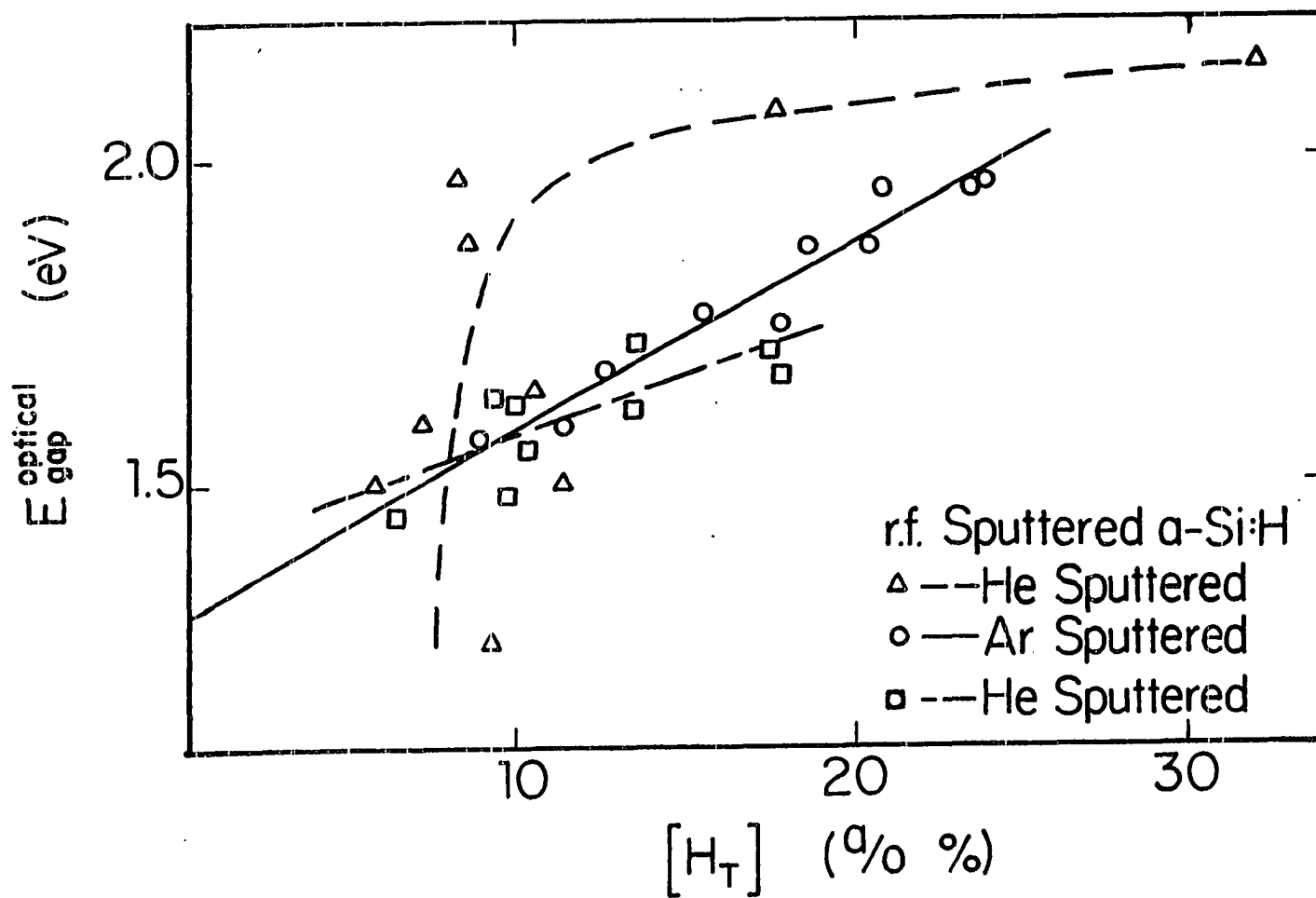


Fig. 31. $E_{\text{gap}}^{\text{optical}}$ vs. $[H_T]$ for the three sets of r.f. sputtered a-Si:H films

scatter in the Xe sputtered films data is large. However, it can be seen that Xe sputtered films give optical energy gaps similar to those of Ar sputtered films with the same hydrogen concentration. It should also be noted that the He sputtered films give the greatest range in $E_{\text{gap}}^{\text{optical}}$; and, that the optical energy gap for these films depend on the hydrogen concentration in a decidedly non-linear manner. These results would suggest that the influence of hydrogen on $E_{\text{gap}}^{\text{optical}}$ is similar for Ar and Xe sputtered a-Si:H, but very different for He sputtered a-Si:H.

The slopes of the $\sqrt{E\alpha}$ vs. E plots are given in Table 2. For the He, Ar and Xe sputtered samples, these slopes were $840 \pm 180 \text{ eV}^{-1/2} \text{ cm}^{-1/2}$, $1700 \pm 300 \text{ eV}^{-1/2} \text{ cm}^{-1/2}$, and $1400 \pm 300 \text{ eV}^{-1/2} \text{ cm}^{-1/2}$, respectively. The uncertainty was taken as one standard deviation in the data. This indicates that the Ar sputtered samples are the most ordered, followed by the Xe sputtered samples and then the He sputtered samples. This correlates well with Ar being the most effective sputtering medium and He the least effective. Again, this indicates that stronger plasma-film interactions give higher quality films.

The Urbach edge coefficient can be determined from the absorption region for which $\ln\alpha$ vs. E is linear. For this exponential region, the absorption coefficient is seen to vary as

$$\alpha = \alpha_0 \exp[(E-E_e)/E_0] \quad (71)$$

where E_e is approximately equal to the energy gap and E_0 is the Urbach edge coefficient. To find α_0 and E_0 , E_e was estimated to be equal to the energy gap of these samples which was found by plotting $\sqrt{E\alpha}$ vs. E , as described earlier. Then a plot of $\ln\alpha$ vs. E was made and a line was fit to these plots using a least squares linear regression. From the

slope, m , and the "y-intercept," y_0 , of this line, α_0 and E_0 were found using

$$\alpha_0 = mE_{\text{gap}}^{\text{optical}} + y_0 \quad (72)$$

and
$$E_0 = m^{-1} \quad (73)$$

In Fig. 32 are plots of $\ln\alpha$ vs. E for six samples. In order to have optical densities large enough to make reliable measurements in the exponential region, it was necessary to make the samples very thick ($> 4\mu\text{m}$). This sample thickness gave optical densities near the largest optical densities that could be measured in the energy region where $\sqrt{E\alpha n}$ vs. E is linear. Thus, accurate determinations of $E_{\text{gap}}^{\text{optical}}$ were impossible for these samples. This introduces an uncertainty in the determination of α_0 , but does not affect the value of E_0 . Listed in Table 6 are the values of α_0 and E_0 , as well as the sputtering conditions, for the samples which were thick enough to allow the determination of the Urbach edge coefficient.

Table 6. The Urbach edge coefficient, E_0 , and prefactor, α_0 , for the r.f. sputtered a-Si:H films

Sample Number	Sputtering Gas	Sputtering Power (ω)	$\alpha_0(\text{cm}^{-1})$	$E_0(\text{eV})$
154	He	300	1390	0.49
153	He	600	700	0.19
163	Ar	100	470	0.08
144	Ar	600	380	0.09
150	Xe	300	380	0.10
149	Xe	600	260	0.08

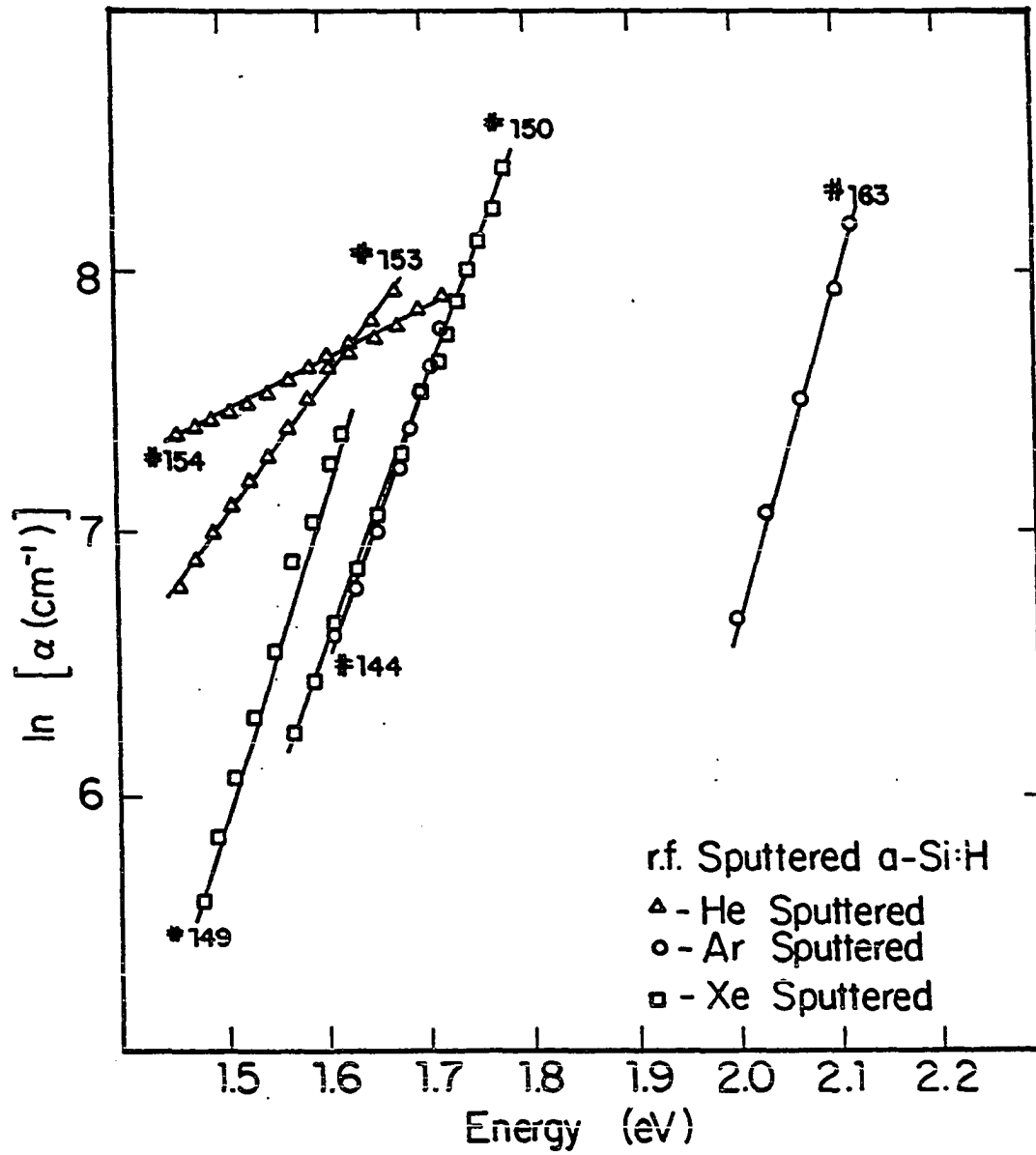


Fig. 32. $\ln \alpha$ vs. E for determination of the Urbach edge coefficient

These data indicate that the samples sputtered in He have the largest Urbach edge coefficient and that this coefficient grows with decreasing sputtering power. This implies that the He sputtered samples have larger and broader band tails than the Ar or Xe sputtered samples. The He sputtered samples also had the largest concentration of weak Si-Si bonds; and, this concentration grew with decreasing sputtering power. Therefore, it seems plausible that the band tail states are caused by weak Si-Si bonds formed by reconstructed dangling bonds.

F. Summary of Results and Conclusions

There are two major conclusions which can be drawn from this comparative study of r.f. sputtering of a-Si:H with He/H₂, Ar/H₂, and Xe/H₂ mixtures. First, that increased plasma-film interactions improves the quality of the deposited film by breaking weak Si-Si bonds. Second, the band tail states in a-Si:H are caused in large extent by weak Si-Si bonds on the surfaces of internal microvoids and/or columns.

Two factors determined the extent of plasma-film interactions during the a-Si:H deposition. These factors were the inert gas used for sputtering, and the r.f. power used for sputtering. Sputtering in Ar gave the largest plasma-film interactions and the highest quality films because Ar is the most effective at sputtering silicon. Helium sputtering gave the least plasma-film interactions and the lowest quality films because of its small sputtering ability. Evidence of this can be seen in five of the results. First, the slope of expected deposition rate vs. measured deposition rate is largest for the Ar sputtered samples and the smallest for the He sputtered samples. This

indicates that the rate at which silicon atoms were removed from the growing film surface was largest when sputtering with Ar and the smallest when sputtering in He. Second, the hydrogen capture cross section was the largest for the Ar sputtered samples and the smallest for the He sputtered samples. This indicates that the helium plasma bombardment of the surface was not able to break weak Si-Si bonds on the growing film surface. Third, unpaired dangling bond densities vs. the concentration of silicon atoms bonded to more than one hydrogen atom indicate the existence of many more weak Si-Si bonds in the He sputtered samples than in the Ar or Xe sputtered samples. Fourth, the slope of the $\sqrt{E_{\text{cut}}}$ vs. E plots for the Ar sputtered samples is larger than that for the He sputtered samples. This indicates that the Ar sputtered films have a higher degree of ordering than the He sputtered films. And fifth, the Urbach edge coefficient is smaller for the Ar sputtered films than the He sputtered films. Thus, the Ar sputtered films have less band tail states than the He sputtered films. This also indicates that the Ar sputtered films have a higher degree of ordering.

The r.f. sputtering power also effected the plasma-film interactions and the quality of the films. The density of silicon atoms bonded to more than one hydrogen atom and the unpaired dangling bond spin density both decreased with increasing r.f. sputtering power. Thus, higher sputtering powers gave higher quality films. This increase in film quality correlates well with the increase in plasma-film interactions expected at higher r.f. sputtering powers. However, it should be noted that the r.f. sputtering power was much less influential than the choice of sputtering gas in determining the quality of the films produced.

These results agree with the results of Ross and Messier^{57,58} which showed decreasing microstructure with increasing plasma-film interactions.

The second conclusion drawn from this work is that band tail states in a-Si:H are caused to large extent by weak Si-Si bonds formed by the pairing of dangling bonds on the surfaces of internal microvoids and/or columns. This can be seen in the large values of the Urbach edge coefficient, which indicates a large density of tail states, for the He sputtered samples. These samples also have the largest density of weak Si-Si bonds. And, for the He sputtered films, both the Urbach edge coefficient and the density of weak Si-Si bonds grow with decreasing r.f. sputtering power. For the He sputtered films deposited at high r.f. powers the density of unpaired dangling bonds and the concentration of silicon atoms bonded to more than one hydrogen atom were both very similar to those obtained when the sputtering was done by Ar or Xe. Therefore, it seems apparent that the density of weak Si-Si bonds, and not $[\text{Si-H}_2]$ or ρ_{DB} , determines the Urbach edge coefficient. This can be understood in terms of the frozen phonon picture of Tauc.⁵⁹ In this model, the Urbach coefficient is proportional to a thermal average of the square of the displacement, U , of the atoms from the crystalline equilibrium positions. Thus, weak Si-Si bonds, with their distorted bond lengths and angles, would contribute states to the band tails.

Cody et al.¹¹ believe that the incorporation of hydrogen reduces the number of band tail states by allowing the a-Si:H to "relax" to a structure more like that of crystalline silicon. This model would not allow the Urbach edge coefficient to increase with increasing hydrogen

concentration as was seen in this work. However, this does not imply a contradiction between the present work and that of Cody et al. In their work, Cody et al. varied the concentration of hydrogen by changing the partial pressure of hydrogen used during the deposition. They used only Ar as the sputtering gas and held the r.f. sputtering power constant. Thus, Cody et al. would not have seen the variation in film morphology observed in this work. So, the density of band tail states in the work of Cody et al. was determined by the total hydrogen concentration; and, the density of band tail states in the present work was determined by the area of microvoids and/or columns within the film.

V. MULTILAYERED FILMS OF $a\text{-Si}_{1-x}\text{H}_x/a\text{-Si}_{1-y}\text{H}_y$

A. Introductory Comments

The possibility of observing quantum well confinement effects in semiconductor superlattices was first proposed by Esaki and Tsu in 1969.^{60,61} They proposed that by alternating thin layers of high and low band gap materials one could confine electrons or holes in a periodic potential very similar to that of the Kronig-Penney band model, but on a much larger scale than is usually considered when using the Kronig-Penney model. It was believed that this structure would allow the study of a quasi one-dimensional system. Figure 33 gives a schematic presentation of the ideas of Esaki and Tsu. In Fig. 33, the periodic "square wells" labelled CB and VB are the conduction and valence band edges of the two semiconductor materials used to form the superlattice, the hatched regions are the new allowed bands formed by the periodic quantum well structure, and l is the period of the superlattice.

Since 1969, much work has been done on crystalline superlattices. Esaki, Chang, Howard, and Rideout⁶² used an MBE system to grow a GaAs-GaAlAs superlattice which exhibited a negative resistance in its transport properties, which was interpreted on the basis of the predicted quantum effect. Resonant tunneling of electrons incident with energies corresponding to the "new bands" in the superlattices was also predicted. This resonant tunneling effect was first observed by Chang, Esaki, and Tsu in 1974.⁶³ Dingle et al. observed pronounced structure in the optical absorption spectrum of superlattice structures,

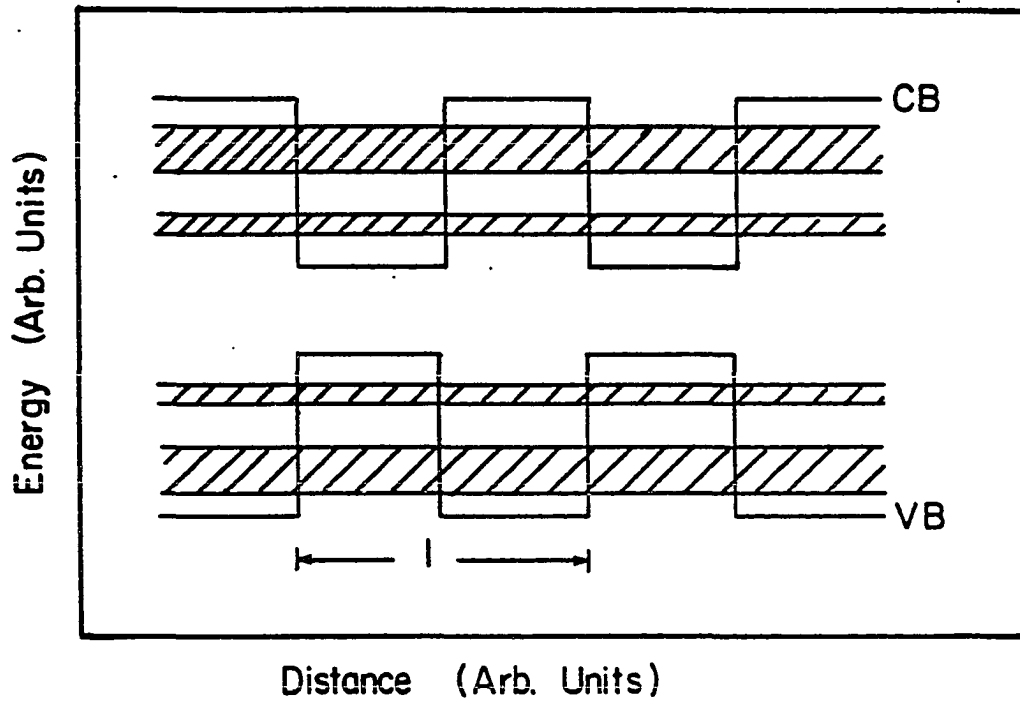


Fig. 33. Schematic representation of quantum well confinement in semiconductor superlattices as proposed by Esaki and Tsu. CB and VB are the conduction and valence band edges, respectively, the hatched regions are the new allowed bands formed by the periodic quantum well structure, and l is the period of the superlattice

representing bound states in isolated⁶⁴ and coupled⁶⁵ quantum wells. It is usually the case that free carriers, electrons or holes in semiconductors are created by doping impurities. Thus, carriers inevitably suffer from impurity scattering. In superlattice structures, it is possible to spatially separate carriers and their parent impurity atoms by doping the high band gap materials and then having the carriers reside in the low gap regions. In 1978, Dingle et al.⁶⁶ successfully implemented such a concept in modulation-doped GaAs-GaAlAs superlattices achieving electron mobilities which exceeded the Brooks-Herring predictions. Also in 1978, Dupius and Dapkus⁶⁷ and Holonyak et al.⁶⁸ succeeded in lasing a quantum-well $\text{Ga}_{1-x}\text{Al}_x\text{As-GaAs}$ laser diode at room temperature. In 1980, Mimura et al.⁶⁹ fabricated a new high speed FET (called the HEMT) using modulation-doped GaAs-GaAlAs superlattices. Although much more work has been done on crystalline superlattices, it is beyond the scope of this paper to cite all of this work.

The work done on crystalline superlattices sparked interest in investigating amorphous multilayers. Amorphous multilayers should not be referred to as superlattices since the constituent layers do not have well-defined lattices. In 1983, Abeles and Tiedje⁷⁰ demonstrated that amorphous multilayers of $\text{a-Si:H/a-SiN}_x\text{:H}$ could be formed. They confirmed the existence of the multilayers using x-ray diffraction and the fact that the electrical conductivity of their films was orders of magnitude larger in the plane of the film than it was normal to the film. They also noticed a shift in the optical energy gap of the multilayers to higher energies with decreasing layer thicknesses. They attributed this effect to a quantum well like formation of discrete

allowed energy levels in their samples. Tiedje and Abeles⁷¹ also observed charge transfer doping in their amorphous multilayers analogous to that observed by Dingle et al.⁶⁶ in crystalline superlattices. Ibaraki and Fritzsche⁷² also observed an increase in the optical energy gap with decreasing layer thickness in a-Si:H/a-SiN_x:H multilayers, which they interpreted as being due to quantum well effects.

It has been proposed that amorphous multilayers could be used in the fabricating of solar cells,⁷³ thin film transistors,⁷⁴ and image sensors.⁷⁵ Thus, for reasons of basic research and technological applications, the study of hydrogenated amorphous silicon multilayers must be considered very important. To this end, hydrogenated amorphous silicon multilayers of alternating high and low hydrogen concentration layers were prepared and studied, and are described below.

B. Sample Preparation

Multilayer films of hydrogenated amorphous silicon with alternating layers of high and low hydrogen concentration were prepared. These samples were fabricated by the r.f. sputtering of a polycrystalline silicon target in an Ar/H₂ atmosphere. As has been noted earlier in this paper, increasing the r.f. sputtering power used for depositing the film had two effects, 1) it increased the rate at which the film was deposited, and 2) it lowered the hydrogen concentration in the film. Taking advantage of the second of these two effects, the hydrogen concentration of the individual layers in the multilayer samples was controlled by alternately sputtering with high and low r.f. sputtering powers. The two sputtering powers used were 600W (3.3 W/cm²) and 50W

powers. The two sputtering powers used were 600W (3.3 W/cm^2) and 50W (0.27 W/cm^2). Individual layer thicknesses were determined by the time of sputtering at each power. From earlier work, it was found that the a-Si:H deposited at a rate of $\sim 1.1 \text{ \AA/sec}$ when sputtering at 50W and at a rate of $\sim 4.0 \text{ \AA/sec}$ when sputtering at 600W. These sputtering rates were used to determine the sputtering time required at each power level to give a predetermined individual layer thickness. In the multilayered samples described below, an attempt was made to make all of the individual layer thicknesses equal. Table 7 gives a summary of the multilayer samples prepared and some preliminary film characteristics. The variation in hydrogen concentration between these films is believed to be the result of three factors. First, setting the hydrogen partial pressure in the sputtering chamber at exactly the same value for each deposition was impossible, but this should only account for fluctuations of a few percent. Second, while fabricating the multilayer samples, it was difficult to set the r.f. sputtering power at exactly 50W or 600W. When the sputtering power was rapidly changed, it was necessary to retune the r.f. matching system. The transmitted r.f. sputtering power would oscillate slightly ($\pm 10\text{W}$) during the time in which the r.f. sputtering system was untuned. Third, when sputtering at 600W the substrate temperature may be higher. This temperature may grow with time when sputtering with 600W for an extended period. It is impossible to say how large this effect may have been because the substrate temperature was neither measured nor controlled during deposition.

Table 7. Summary of multilayer samples used in this work

Sample No.	Number of Periods	Predicted Period (Å)	Observed Period (Å)	[H _T] atomic %	E _{optical gap} (eV)
147	150	102	93.3	24.9	1.94
157	150	102	100	--	1.94
76	19.5	400	328	28.8	1.64
97	19.5	500	385	19.0	1.68
139	15	1025	813	20.1	1.89
119	16	510	940	11.2	1.78
146	14	1025	1021	16.9	1.85
155	4	3075	3375	12.6	1.90
187	1.5	4000	4000	12.0	1.92

C. Multilayer Structure Measurements

Three measurements indicated the existence of a layered structure within the films. In brief, x-ray diffraction results showed samples numbers 147 and 157 to be multilayers. Interference fringing in the optical transmission of samples numbers 119, 139, and 146 confirmed these samples as being multilayers. Reflected electron energy loss spectroscopy (REELS) was used to find the hydrogen concentration as a function of depth for samples numbers 76 and 187. These samples were thereby also confirmed to be multilayers. These measurements will now be discussed in detail.

1. X-ray diffraction

Four criteria must be met for an x-ray diffraction experiment to indicate the existence of layers in a multilayered film. First, the alternating layers must have different total electron densities. The total electron density determines the index of refraction of a material in the x-ray wavelength region. The difference between the index of refraction of the layers determines the reflection coefficient for x-rays impinging on the boundary between the layers. In a-Si:H the total electron density is increased by the addition of hydrogen, but this is probably a small effect since hydrogen has only one electron and silicon has fourteen. Rather, the total electron density of a-Si:H is probably changed most by changing the atomic density of the film. As has been shown earlier in this paper, a-Si:H films sputtered at higher r.f. sputtering powers are more ordered than those sputtered at low r.f. sputtering powers. Therefore, the layers deposited with 600W r.f. power

are probably more dense than those deposited with 50W r.f. power. Note that the effects of hydrogen and bulk density on total electron density are opposed and therefore would tend to cancel each other, since higher hydrogen concentrations are found when sputtering at lower powers. Thus one does not expect large x-ray diffraction peaks from a-Si_{1-x}H_x/a-Si_{1-y}H_y multilayers. A second criterion for a successful x-ray diffraction experiment on a multilayered film is that there be a large number of such layers. Simply put, more layers give more reflections and correspondingly stronger x-ray diffraction peaks. Third, there must be uniformity in layer thicknesses throughout the sample. This allows the Bragg condition,

$$2L \sin\theta = m\lambda \quad , \quad (74)$$

to be met by all of the reflections which then add together to give a diffraction peak. In Eq. (74), L is the period of the multilayer, m is the diffraction order, λ is the x-ray wavelength, and θ is the angle of diffraction. The fourth requirement for a successful x-ray diffraction experiment is that the period, L, be small enough to allow θ to be large enough for the diffraction peak to be observed. In x-ray diffraction experiments, there is always a large signal due to unreflected x-rays for incident angles less than $\sim 0.5^\circ$ which obscure diffraction peaks at lower angles. Therefore, with $\lambda \approx 1.5\text{\AA}$, it is required that the multilayers period be at most

$$L \leq \frac{1.5 \text{ \AA}}{2 \sin(0.5^\circ)} = 85\text{\AA}. \quad (75)$$

This last requirement explains why x-ray diffraction peaks were observed only for samples numbers 147 and 157 (see Table 7). The x-ray diffraction data plots for samples numbers 147 and 157 are given in Figs. 34, and 35, respectively.

Using Eq. (74) rewritten as

$$L = \frac{m}{2\sin\theta} \quad (76)$$

the periods of multilayered samples numbers 147 and 157 were calculated. Taking $m=1$, these periods were found to be 124 ± 3 and 103 ± 3 Å for sample number 147 and number 157, respectively. These periods compare reasonably well with those determined by measuring the total thickness of the film and dividing by the number of periods in the film. The periods measured in this way were 93 and 100 Å for samples numbers 147 and 157, respectively.

2. Optical transmission

Optical transmission measurements on single layer samples characteristically showed interference patterns. The wavelengths at which maxima in these interference patterns occurred were given by

$$\lambda_{\max} = \frac{2nd}{m}, \quad (77)$$

where n is the index of refraction of the film for light with a wavelength of λ_{\max} , d is the thickness of the film, and m is an integer. The optical transmission spectra of multilayer films could have interference patterns corresponding to the total thickness of the film

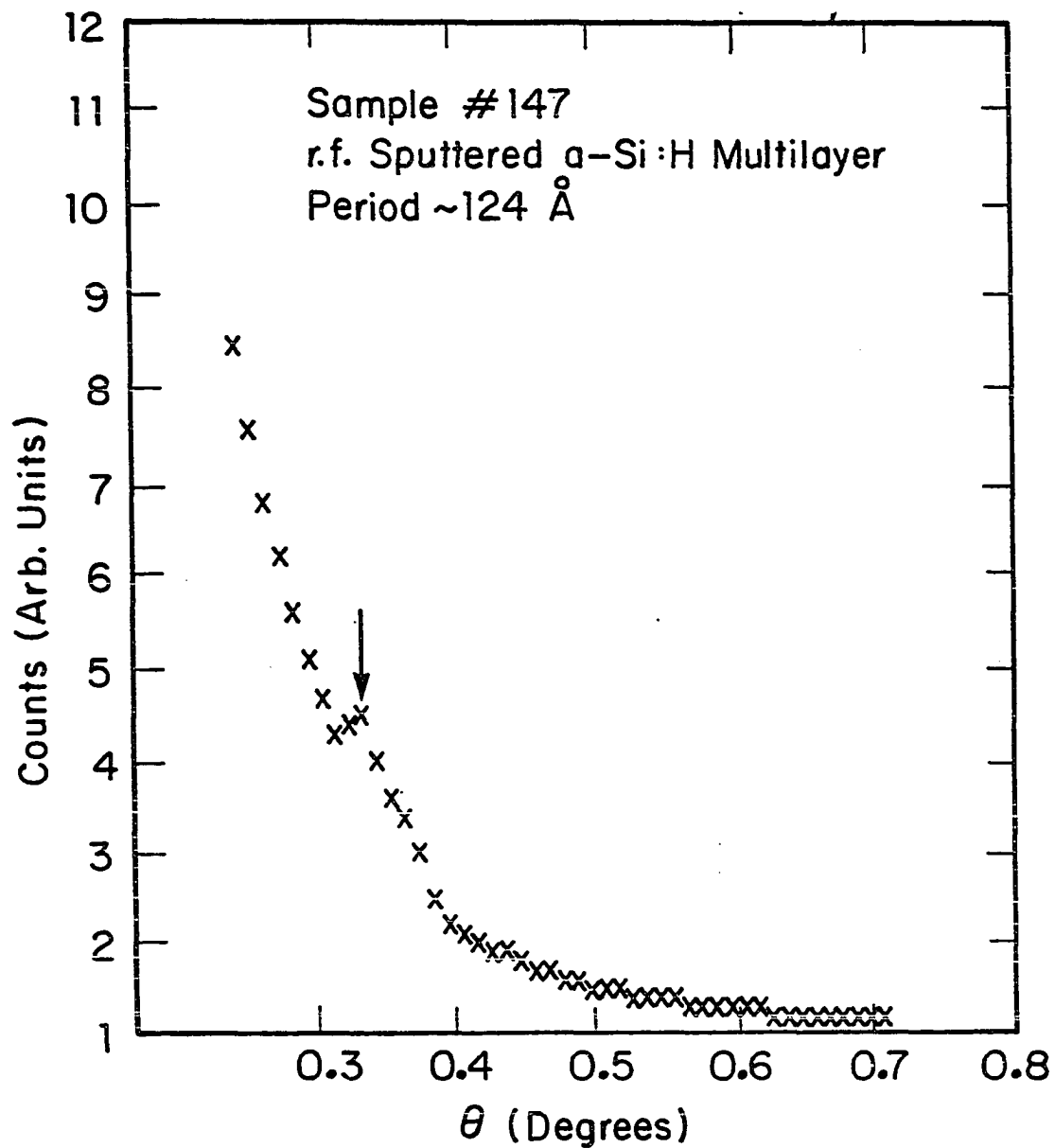


Fig. 34. X-ray diffraction data for a-Si_{1-x}H_x/a-Si_{1-y}H_y multilayer number 147

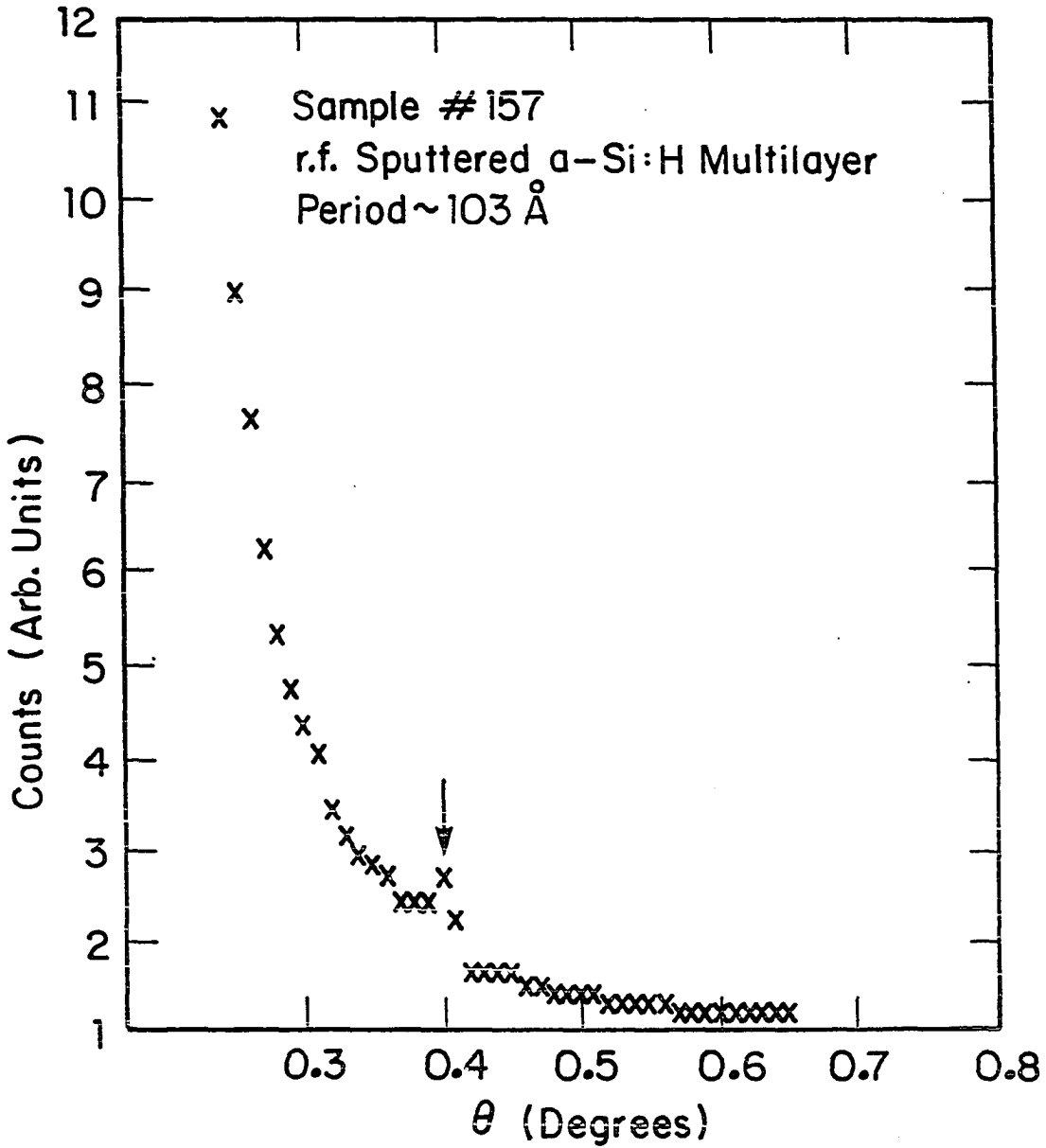


Fig. 35. X-ray diffraction data for $a\text{-Si}_{1-x}\text{H}_x/a\text{-Si}_{1-y}\text{H}_y$ multilayer number 157

and/or to the period of the layers within the film. As with x-ray diffraction, observation of optical transmission interference fringes corresponding to the multilayer period implies the following. First, there must be a difference between the index of refraction of the two layers. The simple classical treatment of Patterson⁷⁶ gives the index of refraction of a semiconductor to be

$$n^2 = 1 + \frac{Ne^2}{m^* \epsilon_0} \frac{\omega_0^2 - \omega^2}{(\omega_0^2 - \omega^2)^2 - \omega^2/\tau^2}, \quad (78)$$

where N is the density of valence band electrons, e is the charge of an electron, m^* is the effective mass of the electron, ϵ_0 is the dielectric constant in vacuum, ω is the angular frequency of the light, and ω_0 is given by

$$\omega_0 = \frac{E_{\text{gap}}}{h}. \quad (79)$$

It should be noted that in Eq. (78) the imaginary part of the index of refraction has been implicitly chosen to be zero. Thus, it is seen that a change in either the density of the material or its optical band gap will produce a change in the index of refraction. Since the energy gaps of materials sputtered at 50W and 600W are different, a substantial difference in their indices of refraction is expected. A second criterion for optical transmission interference fringes corresponding to the period of the multilayers is that there be many layers giving many reflections. The third requirement is uniformity in layer thicknesses so that all of the layers contribute to the fringe at the same

wavelength. Fourth, it is necessary for the multilayer period, L , to be such that λ_{\max} falls in the wavelength region measured. For these experiments, the wavelength region measured was typically 6000 to 10,000Å. Therefore, L must be in the range

$$\frac{m\lambda_{\text{low}}}{2n} < L < \frac{m\lambda_{\text{high}}}{2n}, \quad (80)$$

where m is a small integer (1 or 2), λ_{low} is 600 Å, λ_{high} is 10,000 Å, and n is the index of refraction which was typical ~ 3.5 . Equation (80) gives the allowed range of L to be

$$859 \leq L \leq 2800 \text{ Å} . \quad (81)$$

This criterion, together with the criterion of many layers, explains why only samples numbers 119, 139, and 146 showed signs of optical transmission interference fringes due to the period of the multilayers. Optical density vs. wavelength spectra for samples numbers 119, 139, and 146 are given in Figs. 36, 37, and 38, respectively.

Figure 36 shows a local minimum in the optical density for sample number 199 at ~ 5920 Å. Note that this local minimum occurs where the optical density of the film is ~ 1.75 . The absorption coefficient at this wavelength, as discussed earlier, can be determined using

$$\alpha \approx -\frac{1}{d} \ln \left\{ \frac{\text{O.D.}^{-10}}{T_s(1 - R_1)(1 - R_2)} \right\} \quad (82)$$

where d is the thickness of the film ($\sim 1.5 \mu\text{m}$), O.D. is the optical density (~ 1.75), T_s is the transmission of the substrate (0.97), and R_1 and R_2 are the reflection coefficients of the film-air and film

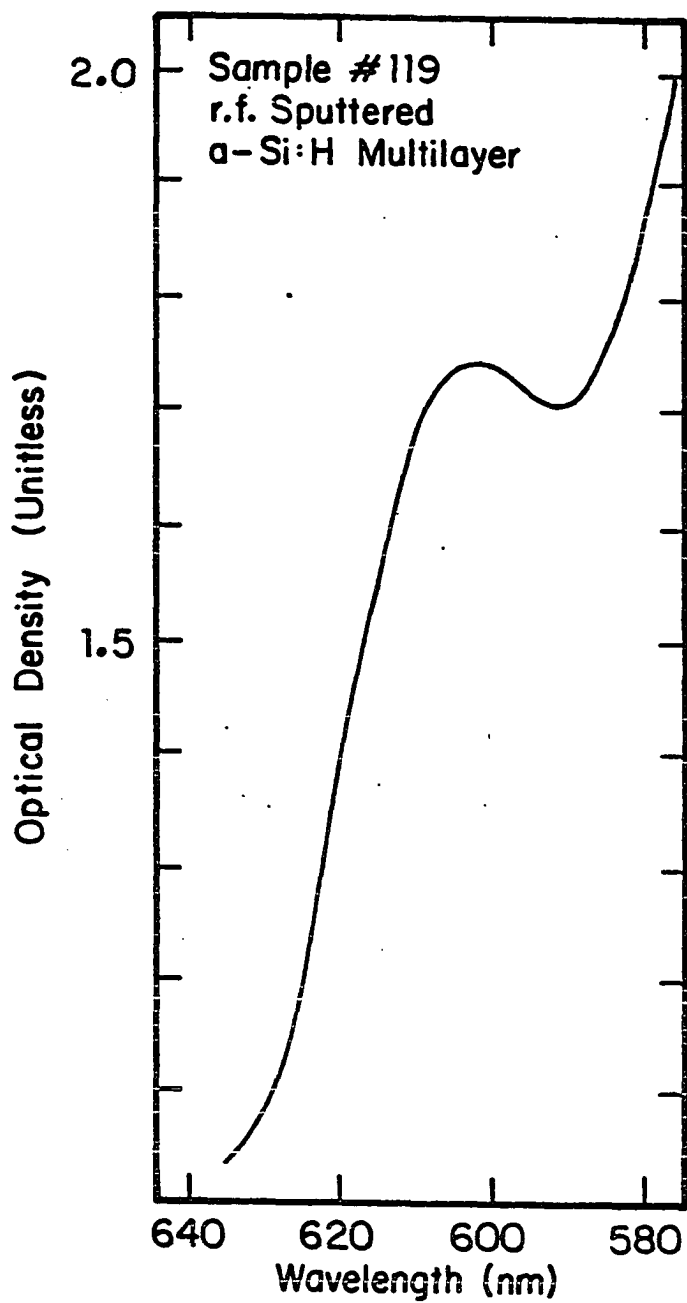


Fig. 36. Optical density vs. wavelength spectrum for multilayer sample number 119. Note the interference fringe at high optical densities

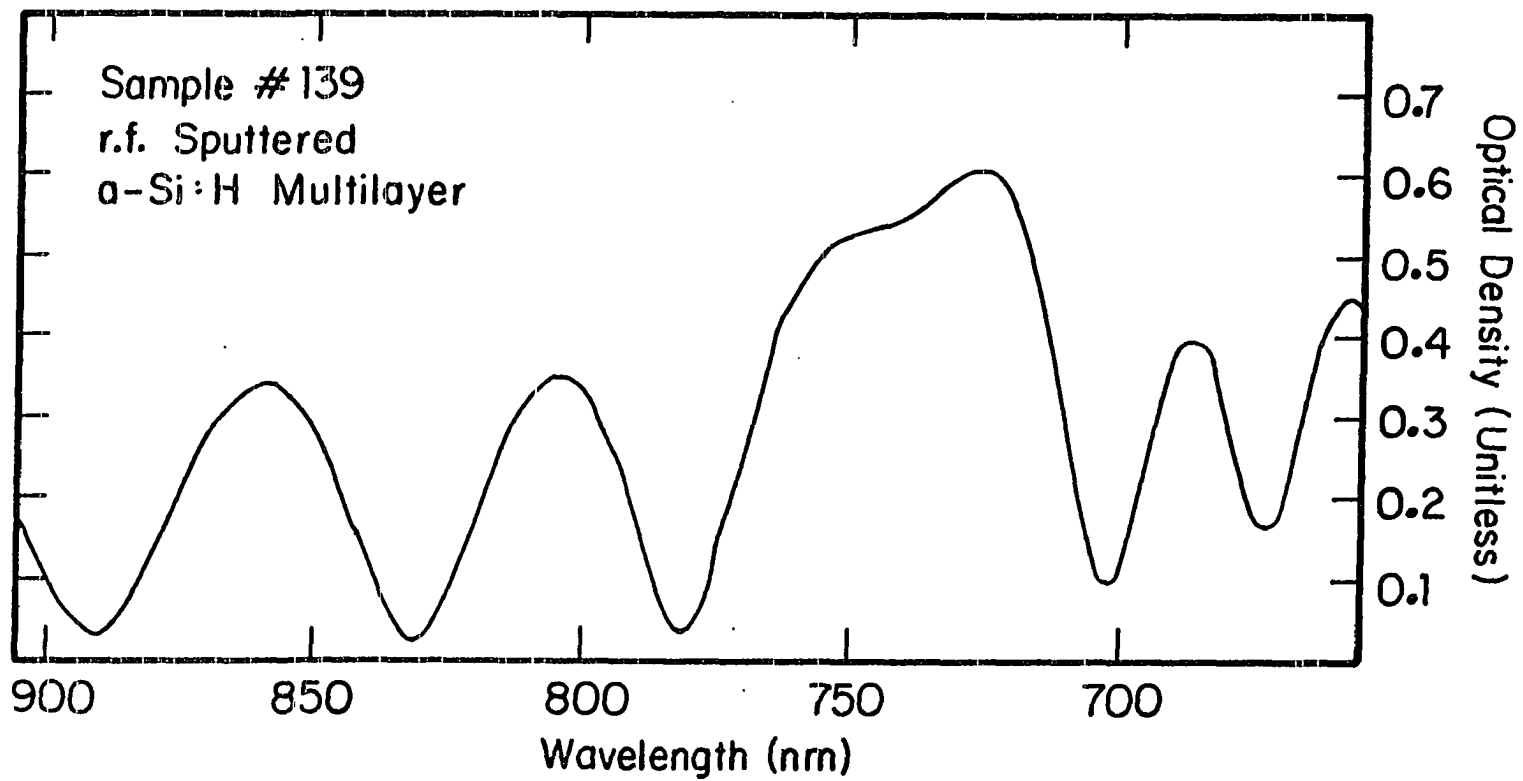


Fig. 37. Optical density vs. wavelength spectrum for multilayer sample number 139. Note the "strange" interference fringe from 780 to 700 nm

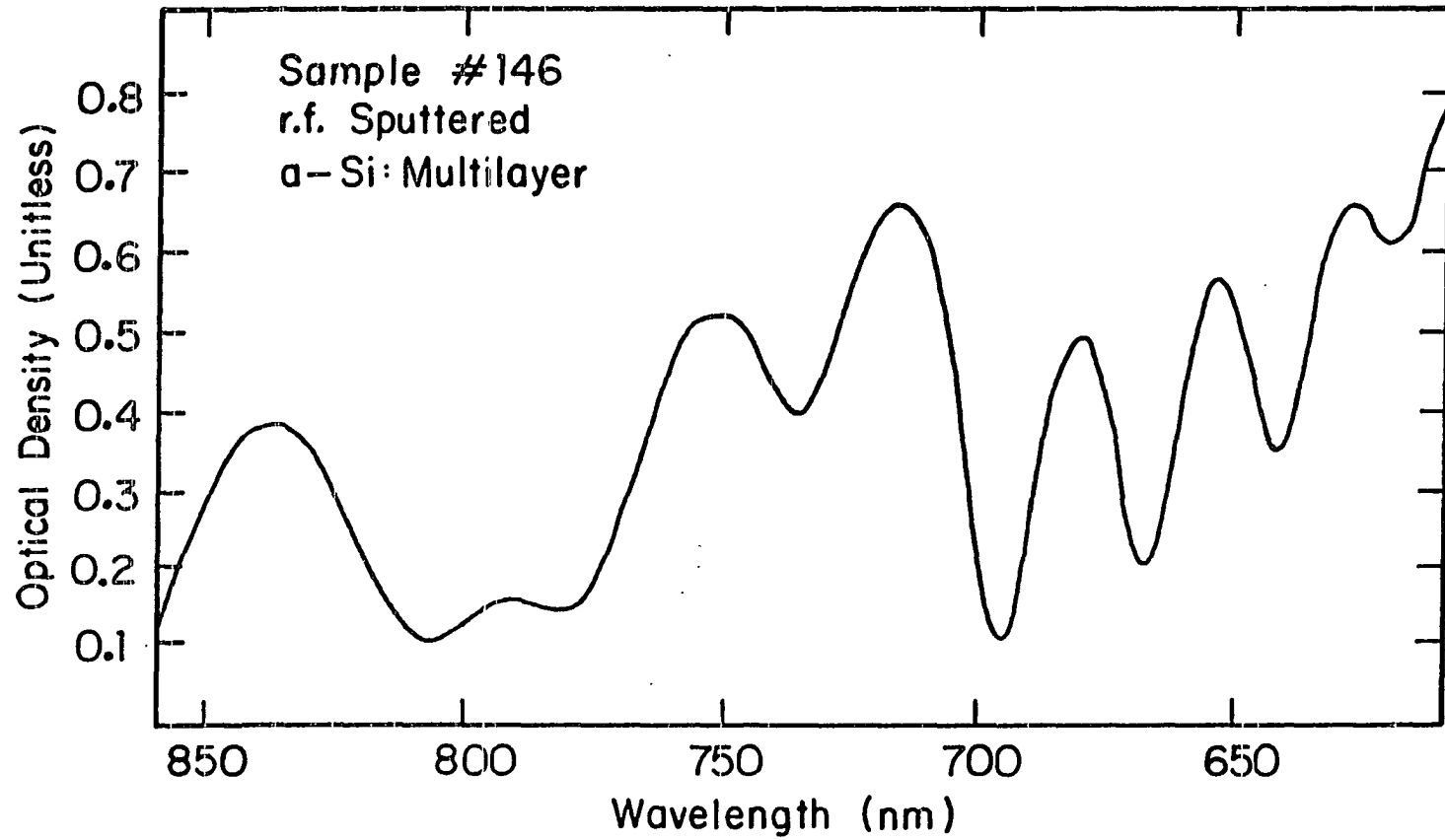


Fig. 38. Optical density vs. wavelength spectrum for multilayer sample number 146. Note the "strange" interference fringe from 810 to 700 nm

substrate interfaces, respectively. Assuming an average index of refraction for the film, as determined by the position of the interference fringes at low optical densities, of 3.2, Eq. (82) gives α to be

$$\alpha = 2.3 \times 10^4 \text{ cm}^{-1} . \quad (83)$$

Interference maxima in transmission arise from the constructive addition of two light waves. The first of these waves is the one which passes unreflected through the film and has an intensity I_1 upon leaving the film given by

$$I_1 \approx I_0 e^{-\alpha d} . \quad (84)$$

In Eq. (84), I_0 is the intensity of light incident on the film. The second wave is the one which is reflected twice and must, therefore, travel the thickness of the film three times. The intensity of this wave is given by

$$I_2 \approx I_0 R_1 R_2 e^{-3\alpha d} . \quad (85)$$

By dividing Eq. (85) by Eq. (84), the relative intensities of these two waves is found to be

$$\frac{I_2}{I_1} = R_1 R_2 e^{-2\alpha d} . \quad (86)$$

Using Eqs. (86) and (83) and assuming the interference fringe at $\lambda \approx 5920 \text{ \AA}$ for sample number 119 corresponds to the total film thickness, the ratio I_2/I_1 is found to be

$$\frac{I_2}{I_1} = 5.0 \times 10^{-5} . \quad (87)$$

This ratio is much too small to account for the large interference fringe observed in the optical density measurement of sample number 199. However, if the interference fringe is assumed to correspond to the period of the multilayers in sample number 119, then the ratio of I_2 to I_1 is found to be

$$\frac{I_2}{I_1} = 3.0 \times 10^{-2} \quad . \quad (88)$$

When considering there are eleven such periods in sample number 119, this is large enough to give the observed interference fringe. The wavelength at which an interference maximum due to the multilayer period is expected can be found from Eq. (77). Here it will be assumed that the index of refraction is 3.2, that this is the first order diffraction maximum ($m=1$), and that d is the multilayer period (940Å). With these assumptions, Eq. (77) gives the wavelength of local maximum transmission to be

$$\lambda_{\max} = 6020 \text{ \AA} \quad , \quad (89)$$

which is fairly close to the observed wavelength of 5920 Å.

Figure 37 shows the optical density vs. wavelength spectrum for sample number 139. It is obvious that the interference pattern observed for $7000 \text{ \AA} < \lambda < 7800 \text{ \AA}$ does not "fit" with the rest of the interference pattern. This strange fringing is interpreted as being due to interference within the multilayer structure. Figure 38 shows a similarly odd interference pattern for $7000 \text{ \AA} < \lambda < 8200 \text{ \AA}$ in the optical density vs. wavelength spectrum of sample number 146.

3. REELS measurements

In the reflected electron energy loss spectroscopy (REELS) technique, a monoenergetic beam of electrons strikes the surface of the sample to be studied. These electrons interact with the sample by exciting plasmons or by causing interband transitions of the electrons within the sample. Some of the electrons incident upon the sample are reflected from the sample. The reflected electrons have energies less than the incident electrons by an amount equal to the energy required to either excite the plasmon or cause the interband transition. The number of electrons reflected with an energy E less than the incident electron energy vs. E constitutes a REELS spectrum.

There are two types of plasmons observed by REELS, the bulk and the surface plasmons. The loss energy of the bulk plasmon is given by⁷⁷

$$E_{BP} = h \sqrt{\frac{4\pi N e^2}{m}}, \quad (90)$$

where h is Plank's constant, N is the density of valence band electrons, e is the charge of an electron, and m is the mass of an electron. The loss energy of the surface plasmon is given by⁷⁸

$$E_{SP} = \frac{E_{BP}}{\sqrt{2}}. \quad (91)$$

The loss energies of interband transitions are determined by

$$E_{IT} = E_f - E_i, \quad (92)$$

where E_f and E_i are the final and initial energy levels, respectively, of the electron involved in the transition. These levels are determined

by the electronic density of states of the sample. The initial state is usually a valence band state, while the final state is usually a conduction band state.

The REELS spectrum of a sample will be unique because the loss energies observed are determined by the electronic structure of the material. Thus, it is to be expected that a-Si:H films with different hydrogen concentrations should give different REELS spectra. This is expected because the addition of hydrogen should change the loss energies of the bulk and surface plasmons; and, the addition of hydrogen should introduce new allowed electron energy levels in the valence and conduction bands of a-Si:H. It is also known that if interband transitions are present at loss energies close to the loss energy of a plasmon, the loss energy and intensity of both the plasmon and the interband transition can be changed.⁷⁹

Reflected electron energy loss spectroscopy combined with ion milling was used to depth profile the hydrogen concentrations of samples numbers 76 and 187. The results of this measurement on sample number 76 will be discussed here, while the results for sample number 187 will be discussed in the section on hydrogen motion. The REELS measurements reported upon here were carried out by Dr. A. J. Bevolo of Ames Laboratory.⁸⁰ For these measurements a PHI TFA fixed spot spectrometer was operated as a REELS spectrometer. The TFA, whose output is the first derivative of the $EN(E)$ spectra, could be operated with a primary electron beam energy E_p as low as 45 eV. The electron beam was incident at 60° to the sample normal to reduce the effects of charging when a 2 keV primary beam was used to acquire Auger spectra. This angle of

incidence also decreased the bulk plasmon signal in the REELS spectra. In addition, the spectrometer was equipped with an ion gun that generated a 1 keV xenon ion beam to clean the sample surface and depth profile through the multilayer specimens. The ion beam struck the sample at an angle of 20° to the surface normal. The electron beam was operated at 100 eV with a current of 0.40 μA and a spot size of 150 μm .

A series of a-Si:H films homogenous with depth but with different hydrogen concentrations were prepared and used to calibrate the REELS spectra to the bulk hydrogen concentration as determined by infrared measurements. Figure 39 shows the first derivative REELS spectra taken with the TFA spectrometer for two reference a-Si:H films, one containing 27% hydrogen, the other 0% hydrogen. The films had been cleaned by ion bombardment to remove the native oxide until only silicon Auger peaks were present above the 0.5% level. The elastic peak width was 0.75 eV and the modulation amplitude was 1 eV. The principal difference between the two spectra occur in the energy loss region from 7 to 13 eV. In addition, the two strong peaks at 5.0 and 1.5 eV are unshifted in energy but reduced in intensity by the addition of hydrogen. A weak should at 15.0 eV nearly disappears after hydrogen incorporation. Sputtering with an argon ion beam yielded the same spectra as those shown in Fig. 39 which were taken during xenon ion bombardment. The spectra shown in Fig. 39 are very similar to those reported for the absorption of hydrogen onto a (100) surface crystalline silicon.⁸¹ Previous attempts to observe the effects of bulk hydrogen on the REELS spectra of argon sputtered glow discharge a-Si:H films were unsuccessful^{82,83} apparently due to the excessive preferential sputtering of hydrogen from the surface of the film.

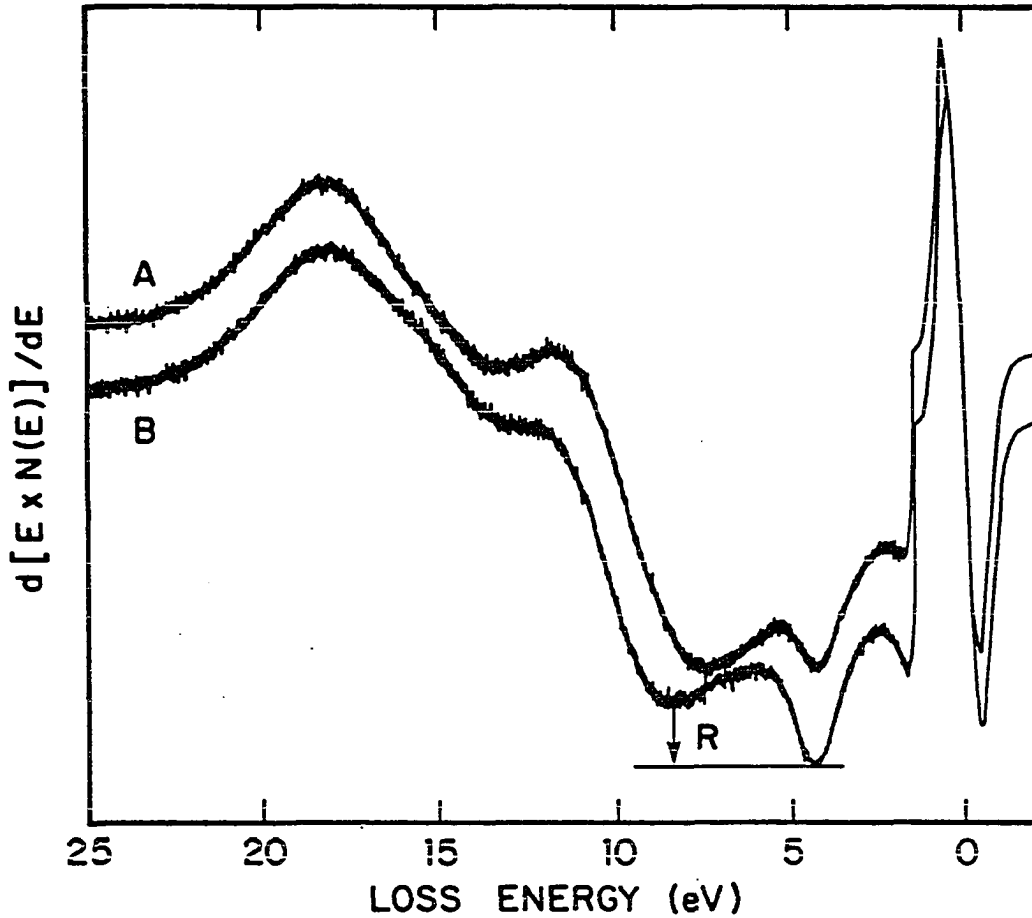


Fig. 39. First derivative REELS spectra taken at $E_p = 100$ eV from an a-Si:H film containing 27 at.% hydrogen (a) and from another a-Si:H film containing 0 at.% hydrogen (b). Small but reproducible changes between the spectra are observed over a loss energy range from 1.5 to 18 eV. The parameter R, used to determine the bulk hydrogen concentration is also shown

A parameter R can be defined as the difference in intensity between the two major negative derivative portions of the spectra near 5 and 8 eV loss energy. It is noted that the negative derivative peak at 5 eV loss does not change in loss energy with hydrogen while the negative peak near 8 eV does shift to lower loss energy with increasing hydrogen content. The parameter R exhibits the largest change with hydrogen between the two samples and serves as a convenient measure of the bulk hydrogen content of the films. Figure 40 shows the linear variation of the parameter R, normalized to the elastic peak intensity, with the bulk hydrogen concentration of the films. Because of the possible effects of preferential ion beam sputtering of the hydrogen, the actual hydrogen concentration, within the 2-3 Å probing depth expected for 100 eV REELS, cannot be determined. Nonetheless, the linear variation of R shown in Fig. 40 permits the bulk hydrogen concentration to be determined as a function of depth with a precision of about one atomic percent. It is emphasized that the results shown in Figs. 39 and 40 were all obtained with the ion beam on during data acquisition and that the spectra remained unchanged with depth for the homogeneous reference samples over depths of hundreds of angstroms beyond the surface oxide, even though the ion beam current densities varied from 1 to 50 $\mu\text{A}/\text{cm}^2$.

After the REELS spectra had been calibrated to the bulk hydrogen concentration of the films, a hydrogen depth profile of sample number 76 was made. The experimental conditions used to acquire data on sample number 76 were the same as for the homogenous films. Figure 41a shows a depth profile of sample number 76 which consisted of 19 periods, each consisting of two layers of different hydrogen content, i.e., 24 and 8%

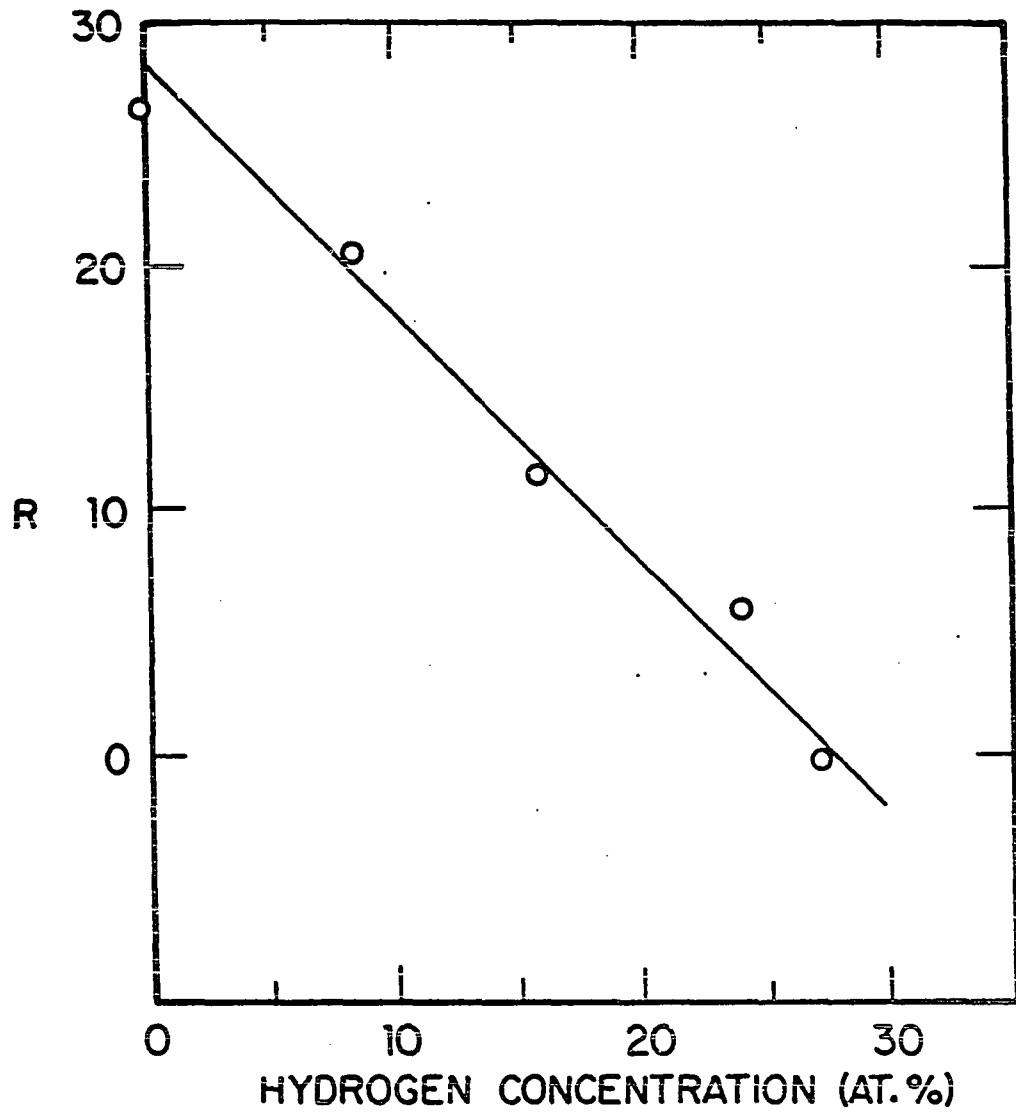


Fig. 40. The linear dependence of R on bulk hydrogen concentration is demonstrated

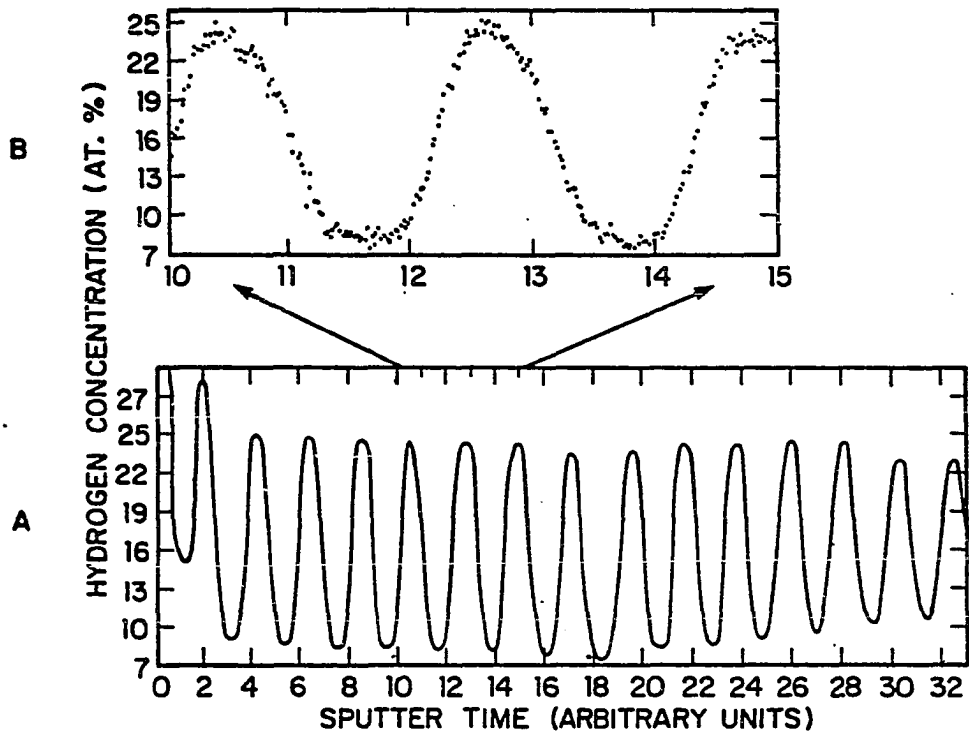


Fig. 41a. A REELS depth profile of a multilayer specimen consisting of alternating hydrogen concentration layers of a-Si:H. One period consists of a high hydrogen concentration layer containing 24 at.% hydrogen and a low hydrogen layer contains 8 at.% H

An expanded view of a portion of the depth profile shown in (a) illustrating the scatter in the data and the interfacial broadening

hydrogen. The thickness of one period was 340 Å. A 1 keV-900nA xenon ion beam with a spot size of 1 mm was rastered over an area of 5x5 mm². Except for the first layer, which contained the surface oxide, regular oscillations of R were observed all the way to the silicon substrate, about 5000Å below the surface of the film. Figure 41b shows an expanded view of a portion of the depth profile. About 100 values of R were determined for each period so that accurate measurements of the interface widths could be obtained. Using the 16% to 84% measure of the interface width, the interface width was seen to increase from 50±5 Å to 80±5 Å as the depth increased toward the silicon substrate. the main contribution to the interface width is believed to be due to ion mixing during depth profiling.

Thus, it was established that sample number 76 did consist of alternating layers of high and low hydrogen concentration a-Si:H. The hydrogen concentration vs. depth of sample number 187 was also profiled using the REELS technique. This sample was also shown to consist of alternating layers of high and low hydrogen concentration a-Si:H. furthermore, thermal annealing studies in conjunction with REELS depth profiling were used to study the motion of hydrogen within sample number 187. These studies are the subject of the next section.

D. Hydrogen Motion in a-Si:H

The motion of hydrogen in hydrogenated amorphous silicon, a-Si:H, has been extensively studied by hydrogen evolution experiments.⁸⁴ However, only a few direct measurements of hydrogen diffusion within the bulk of a-Si:H have been reported. Carlson and Magee⁸⁵ determined the diffusion coefficient as a function of temperature by SIMS depth profiling of deuterated sandwich structures of undoped glow discharge a-Si:H/a-Si:D. Later Beyer and Wagner⁸⁶ used hydrogen evolution measurements to study hydrogen diffusion in undoped, P and B doped glow discharge a-Si:H. For the undoped and P doped a-Si:H they obtained a diffusion coefficient very similar to that of Carlson and Magee, but for B doped a-Si:H their results indicated that diffusion did not occur but rather hydrogen effusion occurred during low temperature annealing. In this work, annealing studies combined with REELS hydrogen depth profiles of an a-Si_{1-x}:H_x/a-Si_{1-y}:H_y multilayered sample (sample number 187) are used to investigate the motion of hydrogen in r.f. sputtered a-Si:H.

The REELS measurements of sample number 187 were carried out using a PHI600 scanning Auger spectrometer (SAM) as a REELS spectrometer. The SAM spectrometer provided imaging capabilities lacking in the PHI TFA. The SAM could only operate for primary electron energies, E_p , greater than 200 eV but had the advantage of SEM capability to avoid defects in the film. The electron beam was incident at 60° to the sample normal to reduce the effects of charging when a 2 keV primary beam was used to obtain Auger spectra. This angle of incidence also decreased the bulk plasmon signal in the REELS spectra. In addition, the SAM was equipped with an ion gun that generated a 1 keV xenon ion beam to clean the

sample surface and depth profile through the multilayer specimen. The ion beam struck the sample at an angle of 20° to the surface normal. Because the electron optics of the SAM were optimized for higher E_p than those of the TFA, it was found that the optimum E_p for REELS in the SAM was 196 eV rather than the 100 eV found for the TFA. At 100 eV the electron beam current in the SAM was too small, while much above 200 eV the energy resolution was too poor. The elastic peak width at 196 eV was 1.1 eV. The electron beam current was 4 nA with a spot size of approximately two microns. During data acquisition the electron beam was rastered over an area of $80 \times 40 \mu\text{m}^2$ to minimize electron stimulated desorption of hydrogen, although no such effects were evident in the unrastered mode.

For sample number 187, three a-Si:H layers, each 2000 Å thick, were deposited. The first layer next to the silicon substrate contained 14% H as did the third layer. Both were deposited with an r.f. power of 50 watts. The second layer, containing 7% H, was deposited at 600 watts r.f. power. This sample was cut into small pieces, typically 3 mm on a side, that were annealed at various temperatures for a period of 1 hr. Several unannealed portions of sample number 187 were depth profiled in the SAM to establish that 1) the specimen was identical over its whole area, 2) the two different Auger spectrometers could be used in the REELS mode, and 3) surface defects could be avoided by the use of the SEM mode of the SAM.

Figure 42 shows the second derivative REELS spectra of the 0 and 27% H reference films taken in the SAM after removal of the surface oxide layer. Because of the poorer energy resolution of the SAM, the

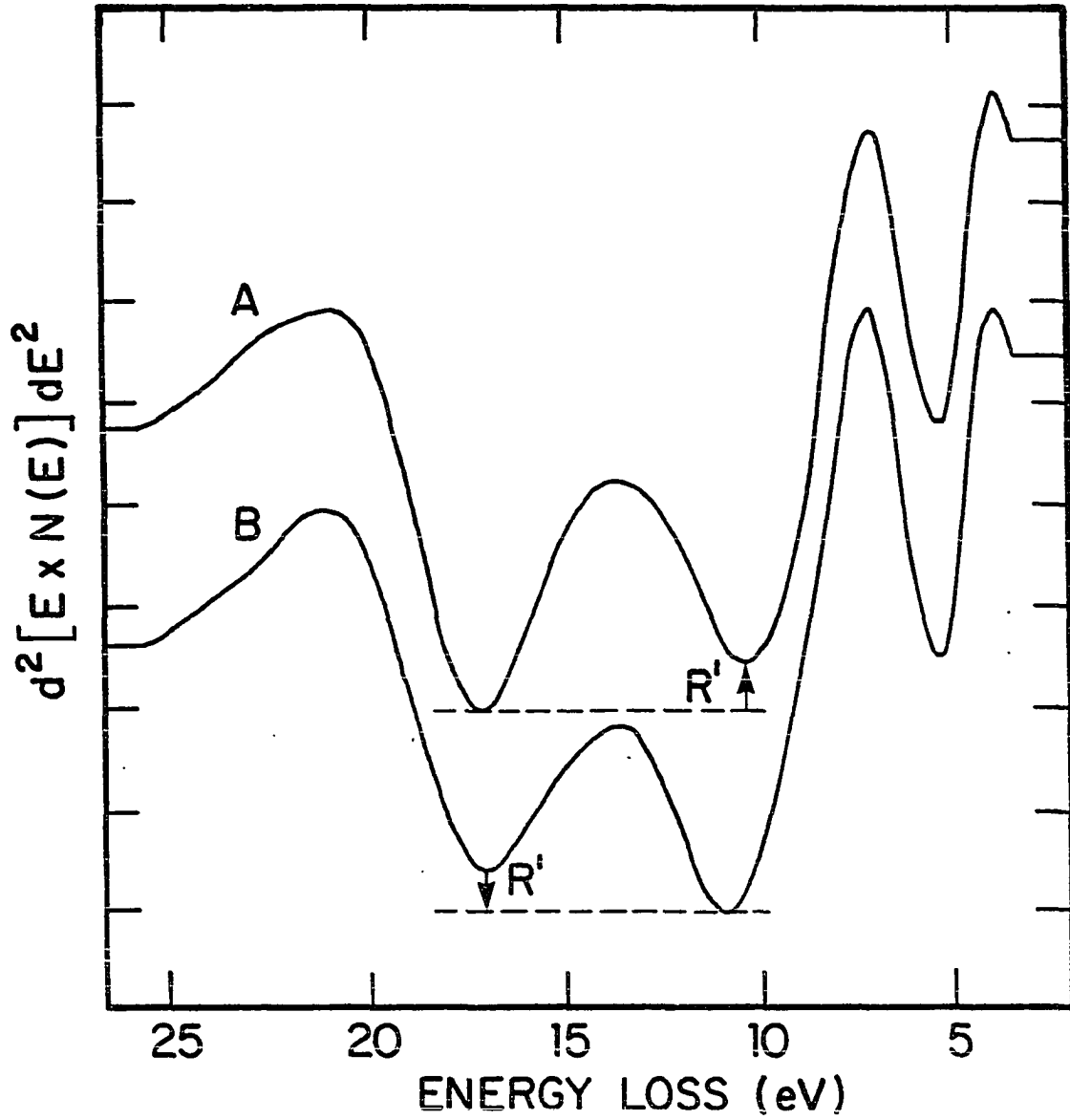


Fig. 42. Second derivative REELS spectra taken at $E_p = 196$ eV from an a-Si:H film containing 27 at.% H (a) and from another a-Si:H film containing no hydrogen (b). The parameter R' is also shown

parameter R used in the TFA generated-spectra could not be used. Instead, a new parameter R', equal to the intensity difference between the maximum negative portions of the second derivative as measured at loss energies of 17.5 and 10.5 eV, was found to correlate well with bulk hydrogen concentrations. As indicated in Fig. 42, R' is positive for 27% H and negative for 0% H. The energy shift of the 10.5 eV peak with hydrogen concentration shown in Fig. 42 reproduces that observed in Fig. 39. Although the REELS data were acquired in the EN(E) mode in the SAM, changes with hydrogen concentration were most evident in the second derivative mode obtained by digital differentiation of the EN(E) raw data.

Figure 43 shows a depth profile of an unannealed three layer film where the vertical axis is given in percent hydrogen as derived from R'. The horizontal axis is given in sputter time rather than units of distance because it is not known how the sputter yield of a-Si:H depends on hydrogen content. The 1 keV - 100 nA xenon ion beam was rastered over a $3 \times 2 \text{ mm}^2$ area to minimize crater edge degradation of depth resolution. The three hydrogen levels as well as the various interfaces are evident in Fig. 43. The increase in H content at the surface of the film is due to the remanant of the surface oxide that produces enhanced R' values. The interface between the top and middle layers has a width of $200 \pm 30 \text{ \AA}$, while the interface between the middle and bottom layer is $500 \pm 50 \text{ \AA}$ wide. In contrast, the interface between the bottom a-Si:H layer and the silicon substrate is only $100 \pm 25 \text{ \AA}$, a value consistent with a $35 \pm 5 \text{ \AA}$ width obtained from a 1000 \AA SiO₂ layer on silicon profiled under the same conditions, considering the 6000 \AA depth of the $100 \pm 25 \text{ \AA}$

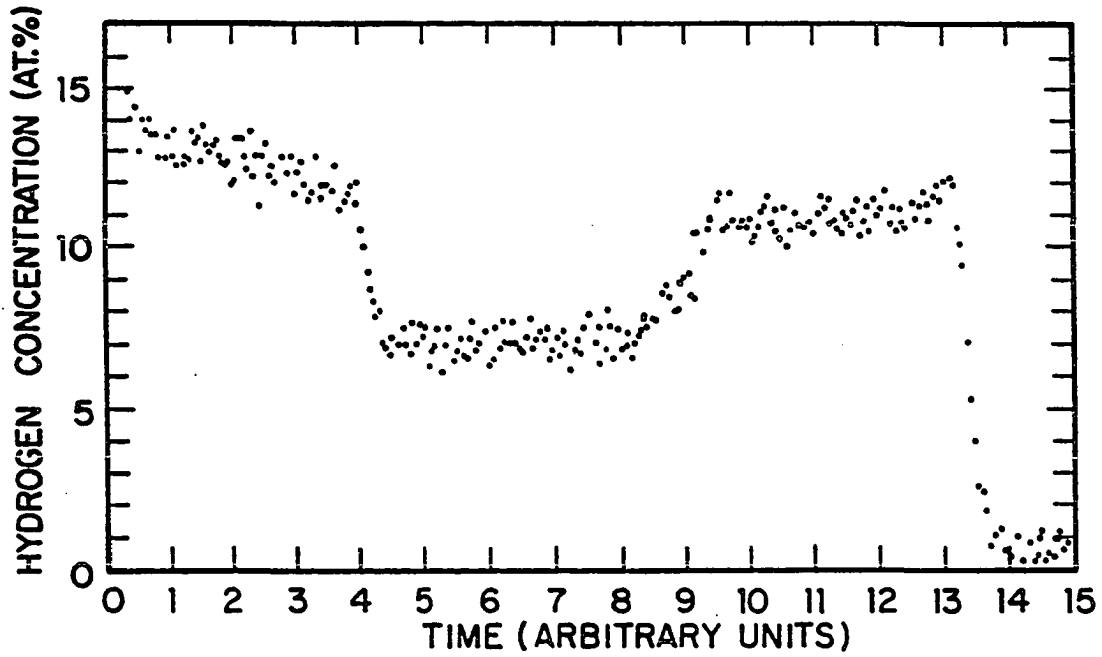


Fig. 43. REELS depth profile of a three layer a-Si:H sample on a silicon substrate. The two high hydrogen layers are readily distinguishable from the middle low hydrogen layer and from the silicon substrate. The three interfaces between the four regions of different hydrogen concentration are apparent in this unannealed sample

interface. Thus, the two interfaces between the three a-Si:H layers are intrinsic and not caused by ion beam mixing from the xenon ion beam used to erode through the multilayer. Rather, the broadening of these two interfaces probably arises from the argon ion mixing and/or thermal effects present during film deposition. The broad 500 Å interface, in contrast to the narrower 200 Å interface, was the only one present during the 600 watt deposition of the middle a-Si:H layer. The slightly lower level of hydrogen in the bottom layer, as compared to its nominally equal value expected from the top layer, is probably due to hydrogen loss during the deposition of the middle and top layer. Identical depth profiles, including interfacial widths and hydrogen levels, were obtained from three widely spaced regions of the original sample thus insuring multilayer uniformity across the whole specimen.

Figure 44 shows, in a schematic manner, the depth profiles of samples that had been heated to 175, 225, 350, 400, and 500°C each for 1 hr as well as the unannealed specimen. The interface widths are ignored in this figure and only the relative to the unannealed sample throughout the total thickness of the multilayer. A slight loss of hydrogen has occurred on the bottom layer of the 225°C sample but not in the other two layers. After heating at 350° for 1 hr, hydrogen was lost in the two high hydrogen layers but not from the middle low hydrogen concentration layer. Only after 400°C does hydrogen leave the middle layer. Overall, about half of the hydrogen remained in the multilayer stack after the 400°C anneal, while after the 500°C 1 hr anneal about 75% of the hydrogen was lost. These values correlate well with the total hydrogen measured in the samples by infrared after annealing but

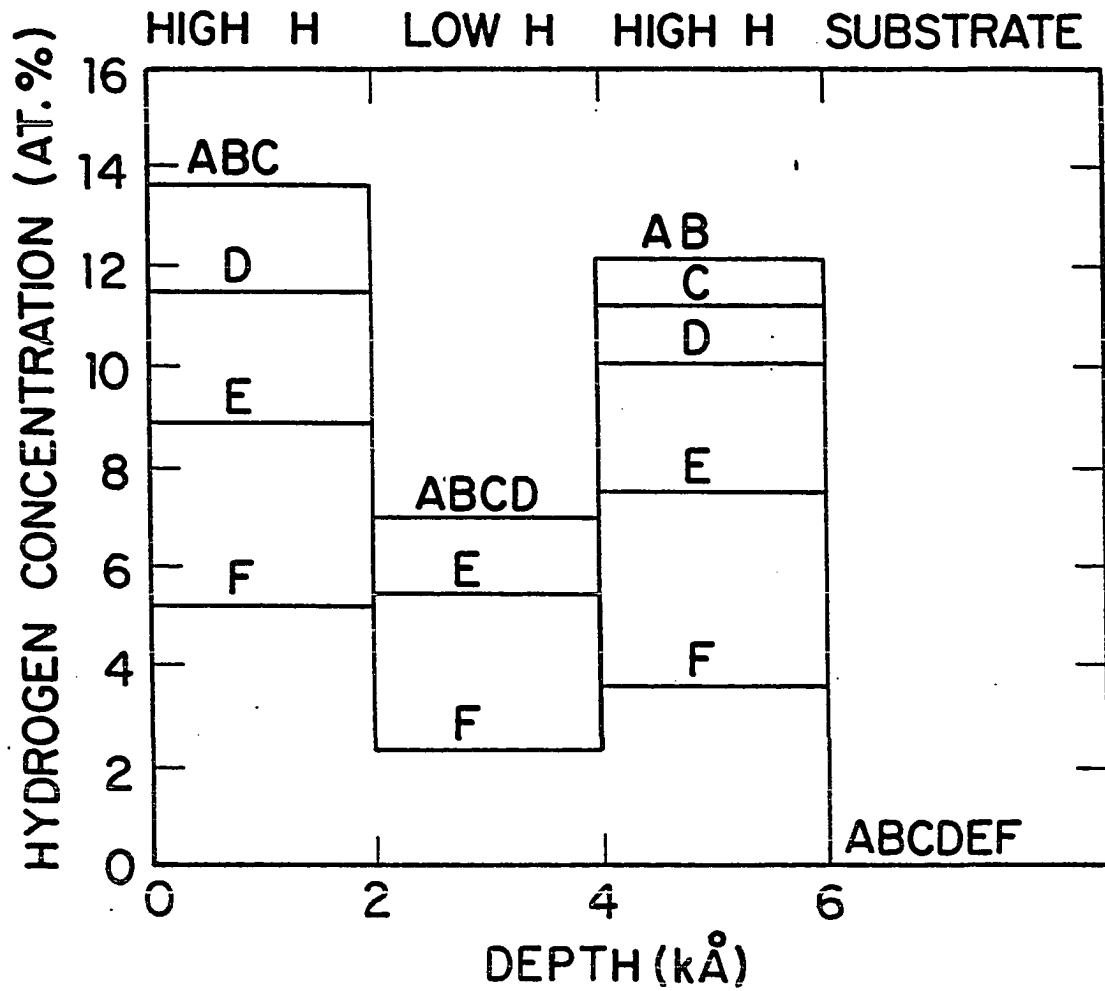


Fig. 44. A schematic representation of the depth profiles obtained from various three layer a-Si:H samples that had been annealed for one hr at 175°C (b), 225°C (c), 350°C (d), 400°C (e), and 500°C (f) as well as an unannealed sample (a). Each hydrogen layer was 2000 Å thick. The interfacial widths, not shown here, are given in Table 8

before depth profiling. In all cases, the bottom layer has lost more hydrogen than the top layer indicating that the surface oxide layer, formed during transport of the specimens from the r.f. sputter unit to the SAM, is more effective as a barrier to hydrogen evolution than the film/substrate interface. Bubbles in the film of the type previously reported⁸⁷ occurred only during the 400°C anneal on a small portion of the sample. The depth profile of this sample was performed well away from this isolated cluster of bubbles.

Table 8 lists the interface widths for each of the five annealed samples and the unannealed sample, where ΔX_1 is the interface width between the top and middle layer while ΔX_2 is the interface between the middle and bottom layers.

E. Conclusions

It has been shown that a-Si_{1-x}:H_x/a-Si_{1-y}:H_y multilayer films (i.e., films consisting of alternating layers of high and low hydrogen concentration amorphous silicon) can be produced by simply alternating the r.f. sputtering power used for film deposition between a high (600W) and a low (50W) value. The existence of the layering has been confirmed by x-ray diffraction, optical transmission, and REELS depth profiling experiments. Furthermore, it has been shown that the REELS depth profiling technique can give an accurate measure of the hydrogen concentration vs. depth into the film.

Perhaps the most interesting aspect of these results is how they compare to the results of similar measurements performed on glow discharge produced a-Si:H. When others^{82,83} had attempted to observe

Table 8. Interface widths observed between top and middle layer, ΔX_1 , and between middle and bottom layer, ΔX_2 , as a function of annealing temperature $T(^{\circ}\text{C})$ and an annealing time of 1 hr. Sample A is an as-prepared sample. ΔX_{CM} is the interface broadening expected if the diffusion coefficient of glow discharge a-Si:H, as reported by Carlson and Magee⁸⁵, were the same for the r.f. sputter deposited a-Si:H used in this study. All interface widths are in units of \AA

Specimen	T	ΔX_1	ΔX_2	ΔX_{CM}
A	-	200	500	-
B	175	200	500	5
C	225	200	500	34
D	350	200	500	1230
E	400	200	500	3540
F	500	200	500	19400

the effect of hydrogen incorporation on the REELS spectra of a-Si, it was discovered that the ion beam bombardment used to clean the surface of the sample preferentially removed the hydrogen from the surface. The hydrogen was removed from the surface to the extent that no hydrogen effects on the REELS spectrum could be observed during or after ion bombardment. In any depth profiling experiment, it is necessary to acquire data while simultaneously ion milling through the sample. Thus, it would be impossible to depth profile the hydrogen concentration of glow discharge deposited a-Si:H using REELS. For r.f. sputtered a-Si:H it was found that while some preferential sputtering of hydrogen from the surface by the ion beam may occur, enough hydrogen was left on the surface to allow hydrogen incorporating effects to be seen in the REELS spectra. This allowed the hydrogen depth profiling of r.f. sputtered a-Si:H using REELS. This also indicates that the silicon-hydrogen bonds on the surface of r.f. sputtered on Si:H are stronger, or at least more nearly equal in strength to the silicon-silicon bonds, than the silicon-hydrogen bonds on the surface of glow discharge produced a-Si:H.

Another difference in hydrogen bonding between r.f. sputtered and glow discharge produced a-Si:H is evident in Table 8. Namely, despite the loss of hydrogen at elevated temperatures, no observable broadening of the interfaces in the r.f. sputtered multilayer sample occurred. For comparison, the interface width, ΔX , predicted by the diffusion coefficient given by Carlson and Magee⁸⁵ for undoped glow discharge produced a-Si:H is also listed in Table 8. Even assuming the maximum interface broadening allowed by our data of 200 Å for the 500°C/1 hr anneal yields a hydrogen diffusion coefficient of only 1.3×10^{-16}

cm^2/sec . This is four orders of magnitude lower than the diffusion coefficient of hydrogen in glow discharge produced a-Si:H at 500°C found by Carlson and Magee ($1.2 \times 10^{-12} \text{ cm}^2/\text{sec}$). This observation also indicates the existence of a fundamental difference in the silicon-hydrogen bonding of r.f. sputtered and glow discharge produced a-Si:H.

VI. REFERENCES

1. D. E. Carlson and C. R. Wronski, *Appl. Phys. Lett.* 28, 671 (1976).
2. G. C. Chittick, J. H. Alexander, and H. F. Sterling, *J. Electrochem. Soc.* 116, 77 (1969).
3. A. J. Lewis, G. A. N. Connell, W. Paul, J. R. Pawlik, and R. J. Temkin in Tetrahedrally Bonded Amorphous Semiconductors, M. H. Brodsky, S. Kirkpatrick, and D. Weaire, editors, *AIP Conference Proceedings*, 20, 27 (1974).
4. W. Paul, A. J. Lewis, G. A. N. Connell, T. D. Moustakas, *Solid State Commun.* 20, 969 (1976).
5. A. Triska, D. Dennison, H. Fritzsche, *Bull. Am. Phys. Soc.* 20, 392 (1975).
6. W. E. Spear and P. G. LeComber, *Solid State Commun.* 17, 1193 (1975).
7. M. H. Brodsky, Amorphous Semiconductors, edited by M. H. Brodsky (Springer-Verlag Publishers, Berlin, 1985), vol. 36, p. 2.
8. P. W. Anderson, *Phys. Rev.* 109, 1492 (1958).
9. A. Matsuda, M. Matsumura, K. Nakiagaqwa, T. Imura, H. Yamamoto, S. Yamusaki, H. Okushi, S. Iizima, and K. Tananaka, in Tetrahedrally Bonded Amorphous Semiconductors, edited by R. A. Street, D. K. Biegelsen, and J. C. Knights (American Inst. Phys., New York, 1981), p. 192.
10. S. Zhao and S. Hunklinger, *Solar Energy Mater.*, 6, 233, (1982).
11. G. D. Cody, T. Tiedje, B. Abeles, T. D. Moustakas, B. Brooks, and Y. Goldstein, *J. De Physique* 42(C4), 301 (1981).
12. J. Tauc in Amorphous and Liquid Semiconductors (Plenum, London, 1976) Ch. 6.
13. M. V. Kuirik, *Phys. Status Solidi (a)* 8, 9 (1971).
14. R. C. Ross and R. Messier, *J. Appl. Phys.* 52, 8 (1981).
15. R. Messier and R. C. Ross, *J. Appl. Phys.* 53, 9 (1982).
16. J. C. Knights and R. A. Lujan, *Appl. Phys. Lett.* 35, 244 (1979).
17. J. C. Knights, R. A. Street, and G. Lucovsky, *J. Non-Cryst. Solids* 35-36, 279 (1980).

18. J. C. Knights, G. Lucovsky, and R. J. Nemanich, *J. Non-Cryst. Solids* 32, 393 (1979).
19. J. C. Knights, *J. Non Cryst. Solids* 36-36, 159 (1980).
20. A. J. Leadbetter, A. A. M. Rashid, R. M. Richardson, A. F. Wright, and J. C. Knights, *Solid State Commun.* 33, 973 (1980).
21. G. Lucovsky, R. J. Nwemanich, and J. C. Knights, *Phys. Rev. B* 19, 2064 (1979).
22. J. C. Knights, T. M. Hayes, and J. C. Mikkelsen, *Phys. Rev. Lett.* 39 712 (1977).
23. R. A. Street, J. C. Knights, and D. K. Biegelsen, *Phys. Rev., B* 18, 1880 (1978).
24. D. K. Biegelsen, J. C. Knights, R. A. Street, C. C. Tsang, and R. M. White, *Phil. Mag. B* 37, 477 (1978).
25. D. K. Biegelsen, R. A. Street, C. C. Tsai, and J. C. Knights, *Phys. Rev. B* 20, 4839 (1979).
26. J. A. Reimer, R. W. Vaughn and J. C. Knights, *Phys. Rev. Lett.* 44, 193 (1980).
27. J. Tauc, R. Grigorovici, A. Vancu, *Phys. Status Solidi* 15, 627 (1966).
28. M. Lax, *Phys. Rev.* 109, 1921 (1958).
29. M. H. Brodsky, M. Cardona, and J. J. Cuomo, *Phys. Rev. B* 16, 3556 (1977).
30. H. R. Shanks, F. R. Jeffrey and M. E. Lowry, *J. De Physique* 42, C4-773 (1981).
31. G. Lucovsky, R. J. Nemanick, and J. C. Knights, *Phys. Rev. B* 19, 2064 (1979).
32. H. Shanks, C. J. Fang, L. Ley, M. Cardona, F. J. Desmond, and S. Kalbitzer, *Phys. Status Solidi (b)* 100, 43 (1980).
33. H. Wieder, M. Cardona, and C. R. Guarnieri, *Phys. Status Solidi (b)* 92, 99 (1979).
34. B. Schmitz, M. Jakubith, and G. Lehmann, *Z. Naturforsch* 34a, 906 (1979).
35. F. Bloch, *Phys. Rev.* 70, 460 (1946).

36. G. E. Pake, Paramagnetic Resonance (W. A. Benjamin, Inc., New York, 1962), Ch. 2.
37. C. P. Poole, Jr., Electron Spin Resonance (John Wiley & Sons, New York, 1983), p. 409.
38. J. C. Knights, R. Lujan, Appl. Phys. Lett **35**, 244 (1979).
39. M. H. Brodsky, R. S. Title, Phys. Rev. Lett. **23**, 581 (1969).
40. R. A. Street and D. K. Biegelsen, in the Physics of Hydrogenated Amorphous Silicon II, edited by J. D. Joannopoulos and G. Lucovsky (Springer-Verlag, Berlin, 1984), vol. 56, p. 199.
41. S. Hasegawa, S. T. Yazaki, Thin Solid Films **55**, 15 (1978).
42. R. A. Street, D. K. Biegelsen, J. C. Zesch, Phys. Rev. B **25**, 4334 (1982).
43. P. J. Caplan, E. H. Poindexter, B. E. Deal, R. R. Razouk, J. Appl. Phys. **50**, 5847 (1979).
44. J. C. Knights, G. Lucovsky and R. J. Nemanich, J. of Non-Cryst. Solids **32**, 393 (1979).
45. G. A. N. Connell and J. R. Pawlik, Phys. Rev. B **13**, 787 (1976).
46. R. A. Street, J. C. Knights, and D. K. Biegelsen, Phys. Rev. B **18**, 1880 (1978).
47. H. H. Anderson and H. L. Bay, Sputtering by Particle Bombardment, edited by R. Behrisch (Springer-Verlag, New York, 1981), Ch. 4.
48. T. D. Moustakas, T. Tiedje, and W. A. Lanford, Tetrahedrally Bonded Amorphous Semiconductors, edited by R. A. Street, D. K. Biegelsen, and J. C. Knights (AIP Conference Proceedings, 1981), no. 73, p. 20.
49. M. H. Brodsky and D. Kaplan, J. Non-Cryst. Solids **32**, 431 (1979).
50. R. A. Street, J. C. Knights, and D. K. Biegelsen, Phys. Rev. B., **18**, 1880 (1978).
51. J. C. Knights, G. Lucovsky, and R. J. Nemanich, J. Non-Cryst. Solids **32**, 393 (1979).
52. G. A. N. Connell and J. R. Pawlik, Phys. Rev. B **13**, 787 (1976).
53. W. Paul, G. A. N. Connell and R. J. Temkin, Advan. Phys. **22**, 529 (1973).

54. A. Matsuda, M. Matsumura, K. Nakagawa, T. Imura, H. Yamamoto, S. Yamasuki, H. Okushi, S. Iizima, and K. Tanaka, Tetrahedrally Bonded Amorphous Semiconductors, edited by P. G. Lecomber and J. Mort, (Academic Press, New York, 1973), p. 425.
55. S. Zhao and S. Hunklinger, Solar Energy Mater. 6, 233 (1982).
56. E. Yahya, Density of Gap States in Hydrogenated Amorphous Silicon, Ph.D. dissertation, Iowa State University, Ames, Iowa, 1984.
57. R. C. Ross and R. Messier, J. Appl. Phys. 52, 5329 (1981).
58. R. C. Ross and R. Messier, J. Appl. Phys. 54, 5744 (1983).
59. J. Tauc, Mat. Res. Bull. 5, 721 (1970).
60. L. Esaki and R. Tsu, IBM Research Note RC-2418 (1969).
61. L. Esaki and R. Tsu, IBM J. Res. Develop. 14, 61 (1970).
62. L. Esaki, L. L. Chang, W. E. Howard, and V. L. Rideout, Proceedings of the 11th Inter. Conf. on the Physics of Semiconductors, Warsaw, Poland, 1972, edited by the Polish Academy of Sciences (PWN-Polish Scientific Publishers, Warsaw, Poland, 1972), p. 431.
63. L. L. Chang, L. Esaki, and R. Tsu, Appl. Phys. Lett. 24, 593 (1974).
64. R. Dingle, W. Wiegmann, and C. H. Henry, Phys. Rev. Lett. 33, 827 (1974).
65. R. Dingle, A. C. Gossard, and Wiegmann, Phys. Rev. Lett. 34, 1327 (1975).
66. R. Dingle, H. L. Stormer, A. C. Gossard and W. Wiegmann, Appl. Phys. Lett. 33, 665 (1978).
67. R. D. Dupius and P. D. Dapkus, Appl. Phys. Lett. 32, 295 (1978).
68. N. Holonyak, Jr., R. M. Kolbas, E. A. Rezek, and R. Chin, J. Appl. Phys., 49, 5392 (1978).
69. T. Mimura, S. Hiyamizu, T. Fujii, and K. Nanbu, Jpn. J. Appl. Phys. 19, L225 (1980).
70. B. Abeles and T. Tiedje, Phys. Rev. Lett. 51, 2003 (1983).
71. T. Tiedje and B. Abeles, Appl. Phys. Lett. 45, 179 (1984).

72. N. Ibaraki and H. Fritzsche, Phys. Rev. B, 30, 5791 (1984).
73. D. E. Carlson, Solar Energy Mater. 3, 503 (1980).
74. P. G. LeComber, A. J. Snell, K. D. Maackenzie, and W. E. Spear, J. Phys. (Paris) 42 C4, 423 (1981).
75. M. Matsumura, H. Hayama, Y. Nara and K. Ishibashi, Proc. 12th Conf. Solid State Devices, Tokyo 1980, Jpn. J. Appl. Phys. 20 Suppl. 20-1 (1981), p. 311.
76. J. D. Patterson, Introduction to the Theory of Solid State Physics (Addison-Wesley Publishing Co., Cambridge, Mass., 1971), p. 308.
77. R. H. Ritchie, Phys. Rev. 106, 874 (1957).
78. E. A. Stern and R. A. Ferrell, Phys. Rev. 120, 130 (1960).
79. H. Froitzheim, Electron Spectroscopy for Surface Analysis, edited by H. Ibach (Springer-Verlag, Berlin, 1977), p. 237.
80. A. J. Bevolo, M. L. Albers, H. R. Shanks, and J. Shinar, J. of Appl. Phys., (submitted).
81. H. H. Madden, Surf. Sci. 105, 129 (1981).
82. H. J. Clemens, Solid State Commun. 51, 483 (1984).
83. J. Derrien, B. Goldstein, A. Cross and F. Salvan, Appl. Phys. Lett. 33, 881 (1978).
84. The Physics of Hydrogenated Amorphous Silicon, Vols. I and II, eds. J. P. Joannopoulos and G. Lucovsky, Springer Verlag, New York (1984).
85. D. E. Carlson and C. W. Magee, J. Appl. Phys. 33, 812 (1978).
86. W. Beyer and H. Wagner, J. Appl. Phys. 53, 8745 (1983).
87. H. R. Shanks and L. Ley, J. Appl. Phys. 52, 811 (1981).